Institut für Zuckerrübenforschung

Establishment of phenotyping routines for assessing tolerance levels to syndrome „Basses Richesses“ of different *Beta vulgaris* varieties

Dissertation

zur Erlangung des Grades

Doktor der Agrarwissenschaften (Dr. agr.)

der Agrar-, Ernährungs- und Ingenieurwissenschaftlichen Fakultät

der Rheinischen Friedrich-Wilhelms-Universität Bonn

von

Justus Detring

aus

Bielefeld, Deutschland

Bonn 2026

Referentin: Prof. Dr. Anne-Katrin Mahlein
Korreferent: Prof. Dr. Gabriel Schaaf

Tag der mündlichen Prüfung: 22.05.2026

Angefertigt mit Genehmigung der Agrar-, Ernährungs- und
Ingenieurwissenschaftlichen Fakultät der Universität Bonn

Für Eva,

ohne Deine unermüdliche Unterstützung wäre diese Arbeit nicht möglich gewesen.

Zusammenfassung

Das Syndrom „Basses Richesses“ (SBR) ist eine schwerwiegende, sich stark ausbreitende Zuckerrübenkrankheit. Syndrom „Basses Richesses“ wird vorwiegend durch das y-3 Proteobakterium *Candidatus* Arsenophonus phytopathogenicus (ARSEPH) ausgelöst. Dieser Erreger wird hauptsächlich durch die Zikadenspezies *Pentastiridius leporinus* (Schilf-Glasflügelzikade) übertragen. Ein SBR-Befall reduziert den Zuckergehalt und die Frischmasse der Rüben erheblich, wodurch der Anbau von Zuckerrüben unprofitabel wird. Durch fehlende effektive Kontrollmaßnahmen ist SBR somit eine Bedrohung für die gesamte Zuckerrübenwertschöpfungskette in Europa. Erste Sorten mit geringerem Ertragsverlust wurden bereits entdeckt, jedoch fehlen robuste Methoden zur Selektion auf dieses Merkmal. Ziel dieser Dissertation ist es, Phänotypisierungsroutinen zu etablieren, um das SBR-Toleranzniveau verschiedener Zuckerrübensorten zu bewerten. Zu diesem Zweck wurde krankes Pflanzenmaterial durch die Inokulation von Zuckerrüben mit infektiösen *P. leporinus* Adulten unter kontrollierten Bedingungen generiert. Das kranke Pflanzenmaterial wurde mit digitalen nicht-invasiven, invasiven, Zeitreihen- und Endpunktphänotypisierungsmethoden untersucht. Es wurde eine ausführliche Datenqualitätsevaluierung von bildgebenden hyperspektralen Messungen entwickelt. Diese bildet die Basis für eine bildgebende hyperspektrale Zeitreihenanalyse der SBR-Pathogenese. Die relevantesten Wellenlängen wurden identifiziert und Teile des Blattapparats mit hoher Bedeutung zur Klassifizierung von SBR mittels maschinellen Lernens bestimmt. Die morphologischen Veränderungen des Blattapparats und der Rübe konnten mittels zwei- und drei-dimensionaler Messung parametrisiert werden. Um die Veränderung des Blattapparats und der Rübe in den Kontext der Wirt-Pathogen-Beziehung einzuordnen, erfolgte eine Untersuchung ausgewählter physiologischer Parameter unter ARSEPH-Infektion. Die Analyse von Alkoholunlöslichen Reststoffen und des Markgehalts zeigt eine SBR-induzierte Erhöhung von strukturellen Inhaltsstoffen bei toleranten Sorten, was durch eine erhöhte Bruchfestigkeit unterstützt wird. Diese Dissertation demonstriert die Anwendbarkeit von digitalen Phänotypisierungsmethoden zur umfassenden Parametrisierung und Charakterisierung der Pathogenese von systemischen Pflanzenkrankheiten wie SBR. Die Ergebnisse dieser Dissertation legen einen wichtigen Grundstein für die Etablierung einer „high-throughput“ Selektion zur Beurteilung des SBR-Toleranzniveaus von verschiedenen Zuckerrüben Sorten unter kontrollierten Bedingungen.

Abstract

Syndrome “Basses Richesses” (SBR) is a severe, fast spreading bacterial disease in sugar beet. The predominant causal agent of SBR is *Candidatus* Arsenophonus phytopathogenicus (ARSEPH), a y-3 proteobacterium. This agent is mainly transmitted to sugar beet plants via the plant hopper species *Pentastiridius leporinus* (reed glass-winged cicada). An outbreak of SBR reduces the sugar content and fresh mass of the taproot profoundly, causing sugar beet cultivation to be non-profitable for growers. The absence of effective control measures against SBR poses a significant threat to the entire sugar beet value chain in Europe. Sugar beet varieties which present a mitigation to the substantial yield loss have been discovered but robust screening methods for such varieties are needed. This thesis presents a set of phenotyping routines that facilitate the assessment of different sugar beet varieties' levels of tolerance to SBR. The creation of diseased plant material was achieved by subjecting sugar beets to inoculation with infective *P. leporinus* adults under controlled conditions. The ARSEPH-infected sugar beets were subjected to investigation through the application of non-invasive, invasive, time series and endpoint digital phenotyping methods. A comprehensive hyperspectral imaging (HSI) data quality assurance pipeline has been developed. This pipeline served as the basis for a HSI time series investigation of the SBR pathogenesis to identify the most important wavelengths and canopy parts for disease classification via machine learning (ML). The morphological alterations of the canopy and taproot were parametrized using two- and three-dimensional measurements. To provide a contextual framework of the SBR-induced canopy and taproot alterations for the host-pathogen interaction, an analysis of selected physiological parameters was conducted on ARSEPH-infected taproots. The analysis of alcohol insoluble residues and marc content indicates an increase of structural components in tolerant varieties induced by SBR, a finding corroborated by increased tissue strength. This thesis demonstrates the applicability of digital phenotyping methods to comprehensively parameterize and characterize the pathogenesis of systemic plant diseases, such as SBR. The findings of this thesis lay the basis for the establishment of a high-throughput screening method for the assessing of SBR-tolerance levels of different sugar beet varieties under controlled conditions.

Publications

Publication I:

Justus Detring, Abel Barreto, Anne-Katrin Mahlein, Stefan Paulus 2024. Quality assurance of hyperspectral imaging systems for neural network supported plant phenotyping. Plant Methods 20:189, https://doi.org/10.1186/s13007-024-01315-y.

Publication II:

Justus Detring, Jonas Bömer, Ayan Gupta, Omid Eini, Anne-Katrin Mahlein 2025. Phenotyping of syndrome “Basses Richesses” in sugar beet by morphological and spectral traits. Phytopathology, https://doi.org/10.1094/PHYTO-07-25-0239-R.

Publication III:

Justus Detring, Jonas Bömer, Christa Hoffmann, Anne-Katrin Mahlein 2026. Morphological and physiological alterations caused by *Candidatus* Arsenophonus phytopathogenicus on different sugar beet varieties. Sugar Industry 151:60-68, https://doi.org/10.36961/si34198.

Abbreviations

2D	Two-dimensional
3D	Three-dimensional
AIR	Alcohol insoluble residues
ARSEPH	*Candidatus* Arsenophonus phytopathogenicus
BRDF	Bidirectional Reflectance Distribution Function
CNN	Convolutional neural network
DNA	Deoxyribonucleic acid
HR	Hypersensitive response
HSI	Hyperspectral imaging
ML	Machine learning
NIR	Near infrared
PHYPSO	*Candidatus* Phytoplasma solani
qPCR	Quantitative polymerase chain reaction
ROS	Reactive oxygen species
RTM	Radiative transfer modeling
SBR	Syndrome „Basses Richesses“
SHAP	Shapley additive explanations
SNR	Signal to noise ratio
SWIR	Short wave infrared
UV	Ultraviolet
VIS	Visible

Table of contents

CHAPTER 1: Introduction

1.1 The pathosystem syndrome „Basses Richesses“

Anthropogenic caused global warming has an enormous impact on agriculture all around the world. The multifaceted ramifications of global warming in the agricultural sector manifest in a decline of crop yields (Hu et al. 2024) causing less availability of food in a growing world population (Vollset et al. 2020). The yield reduction following global warming can be caused directly due to abiotic factors such as extremes of weather (Vogel et al. 2019) or indirectly by favoring conditions for biotic factors such as phytopathogens and insect pests. Insect pests can inhabit new areas when the climate is shifting (Skendžić et al. 2021). In central Europe the winter temperatures rose on average about 2.5 °C since the mid-20th century (Sippel et al. 2024) which increases the overwintering survivability of insects (Marshall et al. 2020). Additionally, mean temperatures in spring increased by 2.1 °C, in summer 1.9 °C and autumn 1.5 °C between 1985 and 2020 (Twardosz et al. 2021) causing longer vegetation periods which enables more pest generations per year (Altermatt 2010; Stoeckli et al. 2012). In the past decades, Europe experienced a northward and altitudinal expansion of mediterranean pests moving into central and northern Europe (Haris et al. 2025). Insect pest damage can be categorized as direct damage caused by feeding on the plant resulting in a loss of plant material and indirect damage occurring due to diseases caused by phytopathogens transmitted by insects (Srisakrapikoop et al. 2020; Wielkopolan et al. 2021). In this instance, the insects are acting as a vector. Through expansion into new habitats, insect vectors introduce non-native phytopathogens to new areas and non-insect vectors are introduced to new microorganisms and phytopathogens, respectively. In recent decades, several cases of insect pest expansion in central Europe have been documented. These include the horse chestnut leafminer, the western corn rootworm and the emerald ash worm (Bažok et al. 2021; Grabenweger 2004; Orlova-Bienkowskaja et al. 2019). Moreover, certain species have shifted their host plant from wild plants to crops. After the introduction of maize to Europe 500 years ago, *Ostrinia nubilalis* shifted from dicotyl plants to maize and became a major pest as the European corn borer (Calcagno et al. 2017). More recently *Pentastiridius leporinus,* the reed glass-winged cicada was able to shift its host to sugar beet, potato and carrot (Behrmann et al. 2023; Gatineau et al. 2001; Pfitzer et al. 2022; Witczak et al. 2025).

The species *P. leporinus* belongs to the order Hemiptera within the family Cixiidae. Its common name "reed glass-winged cicada" origins from common reed (*Phragmites australis* L.) where it has been first reported by Linné in 1761. *Pentastiridius leporinus* is a phloem sap feeding insect which undergoes a hemimetabolous development of five nymphal instars during its juvenile stages before it emerges as an adult (Pfitzer et al. 2022). In 1991 *P. leporinus* has been firstly associated with the spread of the sugar beet disease syndrome "Basses Richesses" (SBR) in central France, where it caused devastating damage followed by an income loss of around 50 % on over 1000 ha (Gatineau et al. 2002). From that day onwards SBR has spread to Austria, Czech Republic, Germany, Hungary, Romania, Serbia, Slovakia and Switzerland (Duduk et al. 2024; EPPO 2025). However, the economic relevance of SBR varies significantly among the countries mentioned. In Czech Republic, Hungary, Romania and Slovakia, the economic influence is to be determined. Serbia is predominantly afflicted by a related pathosystem called Rubbery Taproot Disease (Kosovac et al. 2023). Furthermore, Austria and Switzerland have witnessed a recent increase in the pertinence of SBR (Kreitzer et al. 2025; Mahillon et al. 2022). On the other hand, the abandoning of sugar beet cultivation in the affected regions of France led to the interruption of the epidemic. In contrast, Germany anticipates that approximately one third of its total sugar beet cultivation area will be affected in 2025 (Wirtschaftliche Vereinigung Zucker 2025).

Prior to the transition of *P. leporinus* to the host sugar beet, *P. leporinus* had not been linked to any phytopathogens and thus was not regarded as an insect vector (personal communication). Moreover, it was listed as an endangered species for extinction in Germany (Nickel et al. 2016). Now *P. leporinus* adults can transmit two phytopathogens during feeding on the phloem sap of sugar beet leaves and petioles (Gatineau et al. 2002): the γ-3 proteobacterium *Candidatus* Arsenophonus phytopathogenicus (ARSEPH) and the phytoplasma (16SrXII) *Candidatus* Phytoplasma solani (PHYPSO). Both pathogens are associated with the outbreak of SBR in Burgundy and Franche-Comté, France, in 1991 (Gatineau et al. 2001). However, ARSEPH was determined the dominant causal agent in France (Sémétey et al. 2007a) and is still regarded as the driving force of the SBR epidemic in central Europe. Even though in the recent years higher pathogen prevalences of PHYPSO than ARSEPH are reported in Germany and Austria (Kreitzer et al. 2025; Lang et al. 2025), ARSEPH provides an evolutionary advantage to *P. leporinus* (Kais et al. 2023) which might enabled the host shift to sugar beet and therefore most likely caused the tremendous population increase of *P. leporinus* in Germany.

Candidatus Arsenophonus phytopathogenicus is a long, rod-shaped filamentous proteobacterium which is phloem-limited and considered an endosymbiont (Kais et al. 2023; Sémétey et al. 2007b). Phloem sap feeding insects are known to have evolved evolutional advantages by establishing insect-bacteria-symbiosis (Baumann et al. 2006; Nováková et al. 2009). In the context of an insect-bacteria-symbiosis, the endosymbiont plays a pivotal role in modulating the composition of the phloem sap in susceptible plants. This process involves the enrichment of the sap with nutrients, including sugars (Kais et al. 2023) and amino acids (Sémétey et al. 2007b), thereby facilitating the sustenance of the host organism.

The origin of ARSEPH is still unknown. A coincidental infection of *P. leporinus* with ARSEPH is assumed because *P. leporinus* adults without an ARSEPH-infection have been found in their original habitats (personal communication). *Candidatus* Arsenophonus phytopathogenicus has been localized in the abdomen, salivary glands, midgut and oviduct of adult *P. leporinus* (Bressan 2014). Besides the horizontal transmission of ARSEPH between infected plant material and the insect, the occurrence of ARSEPH in the oviduct enables a vertical transmission to the offspring which is crucial for the preservation of ARSEPH in *P. leporinus* populations. In contrast, PHYPSO is not transmitted vertically to new generations of *P. leporinus,* so that PHYPSO is lost in current laboratory rearing techniques (Pfitzer et al. 2022). Additionally, both ARSEPH and PHYPSO have not been artificially cultivated yet, leaving vector-based transmission of the pathogens as the crucial and only method for artificial infection in controlled experiments.

The propagation of the *P. leporinus* population was additionally promoted in France by the dominant cropping system of winter wheat following sugar beet cultivation (Bressan 2014). The cropping system, sugar beet - winter wheat, provides an optimal environment and living condition for *P. leporinus* throughout all seasons. At the beginning of May, *P. leporinus* adults immigrate from winter wheat fields into neighboring sugar beet fields, mate and lay their waxed eggs in a batch of around 50 together, below ground near sugar beet taproots (Pfitzer et al. 2022). After hatching, the nymphs feed on the thin roots of sugar beet and use dry cracks in the ground for agitation. After sugar beet harvest and sowing of winter wheat, *P. leporinus* nymphs feed on sugar beet taproot debris and winter wheat roots. During winter, the diapause of the nymphs is assumed (Bressan 2014). With rising temperatures in spring, nymphs continue to feed on winter wheat roots, complete the juvenile development and emerge as adults which emigrate into nearby sugar beet fields to start a new life cycle (Bressan 2014). Therefore, substituting winter wheat with crops that do not provide a food source for *P. leporinus*, or even create a breach, is an integrated management option for controlling SBR.

Detring (2022) and Pfitzer et al. (2024) showed maize and soybean as dead-end hosts to *P. leporinus* which consequently reduces the population by starvation when cultivated after sugar beet. Further integrated attempts to control SBR are tillage measures which decimate the number of nymphs in the ground (Pfitzer et al. 2024). Additionally, potent insecticides were approved in emergency admissions in 2025, to control the number of *P. leporinus* adults during sugar beet cultivation, which need to be closely monitored to justify the usage (Bundesamt für Verbraucherschutz und Lebensmittelsicherheit 2025). In general, the high mobility and polyphagia of *P. leporinus* complicate agronomic control measures because nymphs can move deep into the ground, protected from tillage and adults evade into nearby herbaceous areas where they find intermediate hosts.

After the transmission of ARSEPH from *P. leporinus* to sugar beet plants, SBR has a long incubation time before first symptoms appear. Two months after infestation of sugar beet with *P. leporinus*, first visible SBR symptoms are new small, narrow shoots with chlorotic lamina, asymmetrical and lanceolate appearance which are followed by yellowing and vegetation dieback of the older leaves (Bressan et al. 2008; Gatineau et al. 2001). Additionally, a brownish discoloration of the taproot vascular bundles is visible in cross section, which is described in literature as a cause of lignification of the phloem cell walls (Gatineau et al. 2002). Up to now, further phenotypic description of SBR symptoms is missing but urgently needed to enable a robust screening for SBR-tolerant sugar beet varieties. Certain varieties exhibiting tolerance to SBR, including Fitis, Kakadu, Habicht, Ammer, Hibou (SES Vanderhave, Tienen, Belgium) and Multivira (Maribo-Hilleshög, Holeby, Denmark), have been identified within the currently available variety pool (Bundessortenamt 2025). The difficulty controlling SBR with known integrated management measures increases the demand for SBR-tolerant sugar beet varieties. The complex pathosystem and pathogenesis of SBR aggravates the screening for SBR-tolerant varieties. Precise digital phenotyping methods imply broad opportunities to support and establish robust screening methods for sugar beet varieties.

1.2 Digital plant phenotyping techniques

The phenotype is defined by Johannsen (1911) as a distinguishable description of all organisms by direct inspection or by methods of measuring. Thus, phenotyping was practiced long before the development of advanced biotechnology or even the discovery of DNA. For instance, Johannsen (1903) based his findings on the uniformity of pure lines through generations on the grouping of seeds in weight and size and following the selection effect on the descendants. Even today, visual rating by experts is a principal component in the field of plant breeding. Especially environmental impacts such as pests and diseases are still visually scored in plant breeding which could be supported by precise, objective digital phenotyping tools (Mahlein et al. 2019).

Digital cameras, basic image analysis software and early sensor-based tools such as chlorophyll meters and handheld normalized difference vegetation index meters were introduced to plant phenotyping in the 2000s (Mazzetto et al. 2009; Percival et al. 2008). Subsequent to the aforementioned methods, digital phenotyping techniques such as three-dimensional (3D) scanning or hyperspectral imaging (HSI) have been employed. These techniques are broadly available, but their incorporation into plant breeding or variety screening has been limited. Even though advancements in greenhouse automation, in conjunction with these methods, have facilitated high-throughput screening (Furbank et al. 2011). The methods themselves are practically established but need to be adapted to plant specific use cases (Mahlein et al. 2019). In phytopathology fundamental research under controlled conditions is needed to spectrally and morphologically characterize specific diseases and define certain parameters for plant breeding or variety screening. But a standardized data collection and analysis approach is missing (Mahlein et al. 2019) even though non-invasive phenotyping methods such as hyperspectral imaging of the canopy imply the opportunity of a spectral analysis over the whole pathogenesis of a disease (Barreto et al. 2020; Bohnenkamp et al. 2021; Mahlein et al. 2012, 2018, 2019; Okole et al. 2023; Thomas et al. 2018).

The doctrine of spectroscopy is based on the findings of Isaac Newton who described the spectral nature of light and Joseph von Fraunhofer who used a spectroscope to characterize optical properties of glass (Mouroulis et al. 2018). Generally, spectroscopy analysis material compositions based on the interaction of light with matter which was based on the findings from Kirchhoff and Bunsen (1860) who described characteristic spectral lines of various chemicals elements when heated. The basis for this analysis is the sensing of the emitted light from the material or object. Light in this context is considered as electromagnetic waves which are categorized depending on the wavelengths. The electromagnetic waves visible (VIS) to the human eye typically lay between ~380-780 nm (Sliney 2016). Beyond the visible wavelengths, ultraviolet light (UV) lays between 100-400 nm (Coblentz 1932), near infrared (NIR) between 780-1400 nm and short-wave infrared (SWIR) between 1400-3000 nm (Sliney 2016). Depending on the plant phenotyping use case, multi- or hyperspectral sensors are used to measure the emitted light from object of interests between 250-2500 nm (Mahlein et al. 2018). Multispectral sensors can sense a fixed number of certain wavelengths, often considered as spectral bands. Hyperspectral sensors can cover a broad spectral region by sensing a high number of narrow bands (Mahlein et al. 2018). The spectral information of either multi- or hyperspectral data can be allocated in the spatial dimension by spectral imaging systems (Mahlein et al. 2018). If the spatial dimension is added to the spectral measurements, measurements move from single spot to a coverage of the whole object of interest. Hyperspectral imaging not only increases the information in the data but also the complexity in conducting measurements which increases requirements for the imaging system and its set up to produce reliable data.

Generally, HSI-systems are categorized into four different types: push-broom/line scanner, filter-based sensor systems, snapshot and whisk-broom systems. Whisk-broom systems obtain the spatial information pixel by pixel. The interaction of many moving elements inside the camera enables a pixel wise measurement which results in a higher abrasive wear than other systems (Paulus et al. 2020). One of the most established systems is the push-broom/line scanner which records images line by line. This approach implies that either the object or the sensor needs to be moved to enable a second spatial dimension (Sousa et al. 2022). Mobile push broom cameras are equipped with a rotating mirror to mimic the movement which allows a flexible application for various use cases (Behmann et al. 2018). Stationary systems often work with a motorized line scanner. Filter based systems either work with prisms which result in a low spatial resolution or with filters on the sensor chip, in front of an imaging array or as tunable optical filter in front of the cameras optic. Whereas on-chip filter-systems result in low spectral resolution and are more common in multispectral approaches. Tunable filters are often used as an installment on standard imaging devices, e.g.

microscopes (Kong et al. 2013). Thus, the decision to choose the right HSI approach is highly dependent on the intention of use and the measurement setup. One of the most established HSI-systems for plant phenotyping is the push-broom system, because it combines high spectral quality, technological maturity and easy integration into high-throughput, making it ideal for controlled repeatable imaging of large plant populations (Behmann et al. 2015; Habib et al. 2017; Mahlein et al. 2012; Rehman et al. 2020).

Besides the consideration of the HSI-system itself, the illumination needs to be evaluated. Halogen lamps are currently widely used for artificial illumination in HSI because of their high and continuous energy output in the VIS and NIR spectra (Mahlein et al. 2015). Not only the type of illumination but also the positioning and angle can have a tremendous impact on the data quality (Behmann et al. 2015). Every HSI-setup must cope with the 3D-structure of the plant which can be allocated in a xyz coordinate system. In this context, x and y describe the horizontal and vertical axis of the plant and z the areal or depth axis. In terms of illumination, the z axis plays an important role. Thus, plant HSI not only requires a suitable HSI-system but also high-quality illumination. Upon this, the spatial data quality depends on the HSI-system as well as its arrangement in the set up. Most HSI-systems have a fixed focal length binding the focus area to a small distance in the z axis. Therefore, when 3D-objects such as plant canopies are considered, sharpness of the hyperspectral image needs to be evaluated as well. Based on an exhaustive review of existing studies, one must conclude that a plant phenotyping specific workflow for the evaluation of HSI-setups in practice, is missing but highly needed to ensure the highest possible data quality for extensive machine-driven data analysis.

A measurement technique which focuses on the z axis in context with the x and y axis of objects is 3D-scanning. 3D-scanning is an active approach which can measure the 3D-structure of an object by using controlled sources of structured energy emissions such as lasers or light patterns (Harandi et al. 2023). A common technique for measuring small objects such as plants is structured-light-scanning (Paulus et al. 2014b). To receive the 3D-information of the plant, patterns of light with a known dimension are projected onto the target, deformed and imaged by cameras (Winkelbach et al. 2006). The resulting data is a 3D point cloud or mesh which has its data points precisely allocated on the x, y and z axis. Subsequently, the geometry of an object or plant can be derived. Therefore, it offers the possibility to geometrically characterize and quantify the alteration of abiotic and biotic stress on plant source and sink organs. Especially systemic sugar beet diseases such as SBR which infect the vascular system are often associated with reduced and stunted growth of source and sink organs (Gatineau et al. 2001; Hillnhütter et al. 2012; McGrann et al. 2009). To effectively integrate 3D-scanning into variety-screening, the description of distinct morphological parameters is needed. Additionally, connecting morphological alterations to plant physiological changes induced by plant diseases can support the identification of tolerance traits, respectively. Specific physiological traits of sugar beet varieties such as marc contents or alcohol insoluble residues (AIR) have been intensively studied in the context of post-harvest processing (Hoffmann et al. 2018; Kleuker et al. 2021, 2022). Effects of plant physiological parameters on the pathogenesis of systemic diseases such as SBR are missing, even though SBR causes clear deformations on the sugar beet taproot and canopy (Gatineau et al. 2001). Additionally, the hypothesized lignification of the phloem cell walls in the taproot caused by SBR (Gatineau et al. 2002) might affect the taproot structure and therefore texture.

The taproot texture is an important parameter for storability of sugar beets in clamps on the field. Several studies have been conducted to connect physiological parameters with taproot texture and tissue profiles (Hoffmann et al. 2018; Kleuker et al. 2019, 2021, 2022; Nause et al. 2020; Schnepel et al. 2016). The established methods could be applied to phytopathological use cases such as SBR to evaluate the effect on the described parameters. Especially the flexural strength of the taproot might be an additional pathogen specific characteristic of SBR. Higher prevalence of PHYPSO in sugar beet in south Germany (Lang et al. 2025) have recently been associated with similar symptoms as the Rubbery Taproot Disease (Ćurčić et al. 2021). Effects of an ARSEPH-infection on the taproot texture have not been described yet.

The diverging pathogenesis of PHYPSO and ARSEPH depending on the pathogen abundance underlines the need for molecular diagnostics. Primers described from Zübert (2021) to detect the heat shock protein 20 in ARSEPH enables quantitative pathogen detection in sugar beet tissue via quantitative polymerase chain reaction (qPCR). Pathogen detection in ARSEPH inoculation trials via vector transmission provides information about the success of the transmission and infection resulting in infection rates over experimental replicates. Infection rates are the reference data for the analysis of any phenotyping data in phytopathology, which underlines the necessity of molecular diagnostic for phenotyping of SBR.

1.3 Analysis of complex phenotyping data

The analysis of complex phenotyping data in an integrated approach between different methods to draw combined conclusions evolved as a key challenge for plant phenotyping. Especially in high-throughput and image-based phenotyping, vast and multidimensional data sets are assessed which can create a bottleneck in data processing (Mahlein et al. 2019) when relied on classical statistical methods like the analysis of variance or principal components analysis (Fisher 1919; Hotelling 1933). The emergence of machine learning (ML) enabled the handling of complex data sets and created new methods for pattern recognition, making it a cornerstone in plant phenotyping data analysis until today (Gill et al. 2022; Mahlein et al. 2019). But aligning with the opportunities for digital plant phenotyping, also ML-algorithms need to be adapted for the specific use case. Classical linear regression ML-algorithms such as super vector networks can be used for basic classification purposes on one dimensional data (Cortes et al. 1995) like plant height, volume or leaf area. Advanced ML-methods such as nonlinear regression and deep learning are needed if multidimensional data is considered like hyperspectral images (Barreto et al. 2020, 2023; Yamati et al. 2024). Nonlinear regression like Random Forest can analyze the course of the spectral curve in addition to the single band reflectance values (Breiman 2001). Furthermore, deep learning, also known as neural networks, can comprehend spatial information together with spectral information (Barreto et al. 2020, 2023; Yamati et al. 2024). Thus, deep learning techniques consider spectral and morphological changes of a plant leaf under pathogen stress. In the field of phytopathology, biological conclusions drawn from phenotyping data are very valuable for understanding a plant pathosystem. Therefore, explainable ML should be aimed at, rather than the highest possible performance metrics of a ML model.

In addition to data analysis, the utilization of ML-algorithms is imperative for the effective preprocessing of data. It is particularly noteworthy that imaging data comprises a substantial amount of redundant information, including the background. Depending on the experimental hypothesis and use case, image segmentation can be a crucial step before data analysis in addition to the elimination of redundant data. For instance, the plant canopy can be divided into different canopy organs such as leaves, flowers, fruits, petioles, stems and buds. Depending on the phenotyping method and use case, a differentiation between those organs might be necessary. Sugar beet canopies consist of leaves and petioles in their first year of vegetation. Petioles and leaves have significantly different physiological properties and functions (Geiger et al. 1969) and can therefore diverge in their reaction to stress. If a specific stress, such as SBR, is to be phenotyped, the analysis of hyperspectral images of sugar beet canopies necessitates segmentation between leaves, petioles, background and other objects, including the tip of the taproot, which can be visible in the image. Thus, segmentation is crucial for conducting spectral analysis of individual organs. This preliminary processing step is referred to as "semantic segmentation", a procedure that involves the systematic classification of each pixel within an image (Ulku et al. 2022). Semantic segmentation has become a relevant research topic in the field of computer vision. Several supervised algorithms have been established for image segmentation such as Mask R-CNN, SAM or U-Net (He et al. 2017; Kirillov et al. 2023; Ronneberger et al. 2015). U-Net compared to other image segmentation algorithms is a robust solution which can score high accuracies if annotated data is limited.

Independently from the type of algorithm or network, humanly annotated data is required for supervised ML. In supervised ML the objective is to learn patterns from annotated inputs and find them in unknown data (Liakos et al. 2018). For accurate predictions, large amounts of humanly annotated data are needed which can create a second bottleneck in HSI for plant phenotyping. Unsupervised ML does not require annotated data and is looking for patterns by clustering the given data. Because there is no reference data, the interpretation of the results is often complicated and difficult to refer to any biological traits when plant data is used. Thus, for disease characterization and classification supervised ML is often preferrable when annotated data is available.

Random Forest is a widely used supervised ML algorithm for classification and regression tasks in various types of research fields such as medicine, ecology and remote sensing (Belgiu et al. 2016; Fox et al. 2017; Yang et al. 2009). The construction of numerous "decision trees" during the training phase, in conjunction with the integration of predictions, has been demonstrated to yield high and stable accuracies. Each "decision tree" is trained on a random subset of the data, thereby introducing diversity among the trees and helping to prevent the model from learning noise in the training data (Breiman 2001). Random Forest is a popular choice for ML-algorithms due to its ability to easily identify the importance of each feature used for training. This is achieved by summing up the reductions in node impurity across all splits for which a feature is used (Breiman 2001). Additionally, Random Forest is used as a backbone for feature selection methods such as Boruta. Boruta adds permuted features and compares them to the real features. Features which cause a significant better performance than the best permuted feature are considered relevant (Kursa et al. 2010). Furthermore, Shapley additive explanations (SHAP) can be assigned a contribution value to each feature, thereby quantifying the positive and negative effects of each feature on a specific prediction. Thus, SHAP can rank the features and can evaluate dynamics within a feature when feature values are shifted from high to low (Nohara et al. 2022).

In digital plant phenotyping, defining the importance of elevated features in complex data such as hyperspectral images or 3D point clouds is a crucial step to lay the foundation for the characterization of certain stresses or diseases, especially when systemic diseases such as SBR are focused on. Most systemic diseases do not have distinct symptoms, unlike fungal induced leaf spots, which can be allocated in the spatial dimension. This underlines the need for a comprehensive phenotyping approach not only for SBR but also other systemic diseases in any other crop species. Assembling such an approach and elevating high quality data on the phenotype of SBR to support variety screening for highly needed SBR-tolerant varieties is the objective of this thesis.

CHAPTER 2: Research objectives

The main objective of this thesis is to establish a phenotyping routine for assessing the systemic effects of SBR on different sugar beet varieties. To support this objective, high quality data sets are needed to identify characteristic spectral traits during pathogenesis of SBR. However, the usage of HSI in plant phenotyping faces critical technical challenges making quality evaluation of the collected data crucial. Moreover, a systematic approach, considering host-pathogen interaction and routines for a bioassay to provide representative plant material for HSI is needed. In an integrated approach, the digital phenotyping methods HSI and 3D-scanning combined with physiological and molecular techniques, are aimed to be used for evaluating the alterations caused by SBR on the canopy and taproot of different sugar beet varieties. By ML-driven data analysis, crucial features and parameters should be elevated to characterize SBR to assess the tolerance levels of different varieties. This results in the following objectives:

I. The establishment of a data-driven quality assurance pipeline for HSI-systems. The pipeline should include evaluation methods for the spectral and spatial accuracy of HSI-systems and the quality of the resulting data. Furthermore, an optimal illumination scenario for HSI of plants under controlled conditions must be assembled. The data-driven quality assurance pipeline for HSI-systems should be used on a phytopathological scenario for setting up a sophisticated ML-driven HSI-data processing and analysis pipeline.

II. Characterizing and parameterizing the effects of SBR on sugar beet canopies and taproots with HSI, 2D- and 3D-scanning. Consequently, the development of a comprehensive experimental workflow is imperative, encompassing the cultivation of ARSEPH-infected plant material and the meticulous evaluation of spectral and morphological data. For accurate analysis of the canopy hyperspectral information, hyperspectral images need to be segmented between leaves, petioles and redundant objects. This should be followed by an automatic assessment of relevant disease parameters and morphological alterations using ML-algorithms verified by molecular diagnostic.

III. Investigation of the effects of SBR on sugar beet taproots, with a focus on the physiology and texture of different varieties. The investigation should include an analysis of the alterations caused by SBR on marc content, AIR (celluloses, hemicelluloses, lignin, pectin), fresh mass, dry matter, volume, length and width of the sugar beet taproot. Infection of ARSEPH must be verified via molecular diagnostic.

CHAPTER 3: Quality assurance of hyperspectral imaging systems for neural network supported plant phenotyping – Publication I

Accepted manuscript and published online in Plant Methods 20:189 (2024), https://doi.org/10.1186/s13007-024-01315-y.

Justus Detring[1*], Abel Barreto[1], Anne-Katrin Mahlein[1], Stefan Paulus[1]

[1]Institute of Sugar Beet Research, 37079 Göttingen, Germany

[*]Corresponding author: Detring@ifz-goettingen.de

Keywords: Image resolution, Image sharpness, Spectral accuracy, Spatial accuracy, Illumination, Machine learning, Remote sensing, Plant diseases, Computer vision

Author contributions: Conceptualization: JD, SP. Methodology: JD, AB, SP. Investigation: JD. Visualization: JD. Funding Acquisition: SP, AKM. Project Administration: AKM. Supervision: AKM, SP. Writing - Original Draft: JD. Writing - Review & Editing: JD, AB, AKM, SP

Detring *et al. Plant Methods* (2024) 20:189
https://doi.org/10.1186/s13007-024-01315-y

Plant Methods

METHODOLOGY Open Access

Quality assurance of hyperspectral imaging systems for neural network supported plant phenotyping

Justus Detring[1*], Abel Barreto[1], Anne-Katrin Mahlein[1] and Stefan Paulus[1]

Abstract

Background This research proposes an easy to apply quality assurance pipeline for hyperspectral imaging (HSI) systems used for plant phenotyping. Furthermore, a concept for the analysis of quality assured hyperspectral images to investigate plant disease progress is proposed. The quality assurance was applied to a handheld line scanning HSI-system consisting of evaluating spatial and spectral quality parameters as well as the integrated illumination. To test the spatial accuracy at different working distances, the sine-wave-based spatial frequency response (s-SFR) was analysed. The spectral accuracy was assessed by calculating the correlation of calibration-material measurements between the HSI-system and a non-imaging spectrometer. Additionally, different illumination systems were evaluated by analysing the spectral response of sugar beet canopies. As a use case, time series HSI measurements of sugar beet plants infested with Cercospora leaf spot (CLS) were performed to estimate the disease severity using convolutional neural network (CNN) supported data analysis.

Results The measurements of the calibration material were highly correlated with those of the non-imaging spectrometer ($r > 0.99$). The resolution limit was narrowly missed at each of the tested working distances. Slight sharpness differences within individual images could be detected. The use of the integrated LED illumination for HSI can cause a distortion of the spectral response at $677nm$ and $752nm$. The performance for CLS diseased pixel detection of the established CNN was sufficient to estimate a reliable disease severity progression from quality assured hyperspectral measurements with external illumination.

Conclusion The quality assurance pipeline was successfully applied to evaluate a handheld HSI-system. The s-SFR analysis is a valuable method for assessing the spatial accuracy of HSI-systems. Comparing measurements between HSI-systems and a non-imaging spectrometer can provide reliable results on the spectral accuracy of the tested system. This research emphasizes the importance of evenly distributed diffuse illumination for HSI. Although the tested system showed shortcomings in image resolution, sharpness, and illumination, the high spectral accuracy of the tested HSI-system, supported by external illumination, enabled the establishment of a neural network-based concept to determine the severity and progression of CLS. The data driven quality assurance pipeline can be easily applied to any other HSI-system to ensure high quality HSI.

Keywords Image resolution, Image sharpness, Spectral accuracy, Spatial accuracy, Illumination, Machine learning, Remote sensing, Plant diseases, Computer vision

Background

Hyperspectral imaging systems

Hyperspectral imaging (HSI) originated in 1986 when the first airborne hyperspectral spectrometer for mineral

---

*Correspondence:
Justus Detring
Detring@ifz-goettingen.de
[1] Institute of Sugar Beet Research, Göttingen, Niedersachsen 37079, Germany

mapping was launched by GER Corp. This was soon followed by a more advanced HSI-systems from NASA/JPL capable of collecting images in the range of 400 to 2500nm [1]. From this on, the development of various spectral sensors increased. Today, HSI has a wide variety of applications ranging from medicine, food safety, environment, geology and agriculture [2–6]. The potential of hyperspectral sensors to remotely measure spectral characteristics of objects is based on the fact that materials emit electromagnetic energy in signatures that correspond to their chemical composition and physical structure [7]. The emitted electromagnetic energy is considered as reflected light, which forms certain characteristic spectral signatures depending on the sensed object and its state. The advantage of HSI-systems compared to non-imaging systems is the acquisition of spatial information in the form of pixels. Each of these pixels contains the spectral information according to the spectral and spatial resolution of the HSI-system used.

In general, HSI-systems are categorized into four different types: push broom or rather line scanner, the filter-based systems, snapshot systems, and whisk broom systems [8]. One of the most established systems is the line scanner, which acquires images line by line. This approach implies that either the object or the system must be moved to enable a spatial measurement [9]. Currently available handheld line scanning systems are mirror based to enable line scanning [10], allowing flexible application for different use cases [11–14].

HSI quality aspects for plant phenotyping

The introduction of high-end technologies such as HSI has greatly improved plant phenotyping. In general, plant phenotyping describes the response of a plant with its specific genetic background to various environmental factors and vice versa [15]. Especially in the field of plant disease detection, HSI has not only improved variety screening [16, 17], but also promoted precision agriculture by supporting decision making for crop protection, yield cataloging and fertilization [18–20]. Fungal plant diseases have become highly investigated objects for HSI in phytopathology [18, 21, 22] because of their strong influence on yield and food quality. There are multiple studies investigating Cercospora leaf spot (CLS) with HSI on different scales [11, 21, 23]. CLS causes distinct leaf spots that can be accurately localized in the spatial information of a hyperspectral image [11, 21].

In order to draw meaningful conclusions from the analysis of hyperspectral images, it is essential to increase the image quality as much as possible. The quality is characterised by several technical specifications, such as the spectral or the spatial resolution. Modern non-imaging hyperspectral sensors can measure in a spectral range between 350-2500nm of the electromagnetic spectrum [6]. This covers the visible (VIS, 400-750nm), near infrared (NIR, 750-1000nm), shortwave (SWIR, 1000-2500nm), and partially the ultraviolet (UV, 100-400nm) portion of the electromagnetic spectrum. The measurement of the spectral range is divided by spectral wavebands. The proximity and width of these wavebands define the spectral resolution of a given system, which can be less than 1nm in high resolution non-imaging spectrometers. Nevertheless, the correlation between wavebands situated in close proximity enables the measurement of systems with reduced spectral resolution, a common occurrence in the case of HSI-systems. [6]. To exploit the full sensitivity of a hyperspectral sensor and obtain the best possible image quality, it is important to consider additional factors before and during the measurement, such as illumination, spatial resolution, and image sharpness. Since the sensor measures the reflected energy originated from the illumination, spectral range and intensity of the illumination source have a significant impact on the image and data quality. In-field illumination conditions with sunlight as the source of illumination can change within seconds. Therefore, it is essential to use a reference material within each measurement.

The standard illumination for laboratory HSI setups are currently halogen lamps [8, 24]. Halogen lamps have high energy output in the VIS and NIR spectra [24] which are spectral regions covered by most HSI-systems. Light-emitting diodes (LEDs) have recently been introduced to HSI as a supplement to halogen lamps in the UV-blue region [25] and also as exclusive illumination [24, 26]. The strong light emission in the NIR spectral region of halogen lamps is beneficial for various plant phenotyping applications, since its considered as an important spectral region for plant spectroscopy. The light emission in the UV and VIS-blue region of halogen lamps may be insufficient depending on the application and HSI-system, where LEDs may be more convincing. In plant phenotyping, both illumination systems have to cope with the geometric structure of leaves and plants for HSI. Depending on the position of the illumination and its angle of incidence, the illumination may not be evenly distributed on the leaf or plant of interest. In addition, measurement angle and distance have a strong influence on data quality and the level of detail [12, 27]. This is one of the major challenges in HSI for plant phenotyping.

Spatial accuracy of hyperspectral images depend on the spatial resolution and image sharpness. Line scanning spectral sensors have a fixed line length defined by a certain number of pixels, which determines the spatial dimension of the y-axis of the image. The length of the x-axis is variable and depends on the movement distance of either the system or the object of interest.

To apply line scanning HSI in uncontrolled conditions, devices have been developed with a fixed spatial dimension where neither the HSI-system nor the object has to be moved for measuring. Handheld line scanning HSI-systems with a fixed focal length, have limitations in varying the measurement distance when a sharp hyperspectral image is desired. The focal length combined with the sensor chip size defines the field of view. The focal ratio which is describing the light gathering ability is influencing the sharpness of an image in relation to the distance of the measured object as well. In this context the plant geometry is once more challenging. Since plants are three dimensional structures not every latitude in the z-dimension can be measured with the maximum sharpness of an HSI-system. The sine-wave based spatial frequency response (s-SFR) is the international standard method for evaluating image resolution and sharpness of digital cameras [28]. This method is based on the Nyquist-Shannon sampling theorem [29], which has not been applied to hyperspectral images before in literature. There is always a trade-off between latitude focus, depth of field, and region of interest in relation to the field of view and measuring distance. Handheld line scanning HSI-systems, in particular, face difficulties in meeting these requirements. Therefore, it is essential to validate every newly developed HSI-system for its use in plant phenotyping.

Machine learning in hyperspectral imaging driven plant phenotyping

The use of HSI in plant phenotyping produces complex and vast datasets that are challenging to handle. Machine learning, a subfield of artificial intelligence, allows for in-depth analysis of HSI data. Classical regression models typically rely on one-dimensional parameters. For example, if the model is designed to classify a pixel in an image based on its spectral characteristics, it only takes into account individual spectral values within the measured spectral range. More advanced machine learning methods, such as neural networks, can take the entire complexity of spectral signatures of the pixel's spectrum into consideration for classification [30]. In addition, neural networks are capable of recognizing the morphology of objects in images, expanding data analysis to include spatial information. Neural networks are favourable for pattern recognition, which enables precise understanding of HSI data and improves the extraction of plant traits. In particular, convolutional neural networks (CNN) are predestined for image analysis. CNN's main architectures consist of several convolutional layers in which the data is analyzed, causing a reduction of unnecessary parameters and creating a holistic understanding on the analyzed data points [31]. Liu et al. [30] designed a CNN architecture specifically for analyzing spectral data. The designed CNN architecture leads to a one-dimensional analysis of the whole spectrum, making it highly applicable for multiclass pixel classification based on HSI data.

To accomplish high accuracys for such classifications high quality hyperspectral images are necessary. Following a pipeline is proposed (Fig. 1) to evaluate critical quality aspects of hyperspectral images such as spatial and spectral accuracy and illumination systems for HSI. Furthermore, a usecase is presented to analyse quality assured hyperspectral images supported by neural networks for phenotyping of plant disease severity progression.

Methods

Hyperspectral imaging system technical aspects

A handheld hyperspectral line scanning imaging system (Blackmobile, HAIP Solutions GmbH, Hannover, Germany; Fig. 2; hereafter: HC) was used to proof and demonstrate the proposed pipeline to ensure high quality HSI measurements for plant phenotyping.

The HC is equipped with a metal-oxide-semiconductor (CMOS) VNIR hyperspectral sensor and an ultra high resolution (4K) RGB sensor (Tab. 1). The built-in CMOS sensor is capable of measuring incident electromagnetic energy between 500-1000nm with a spectral resolution of 5nm, resulting in 100 spectral bands per measurement (z-dimension). The spatial resolution of the image outcome consists of 640*480px (x,y-dimension). The exposure time for the line scan procedure can be adjusted between 1000-5000μs per line. A gain function is provided to adjust the sensitivity of the sensor by increasing or decreasing the current supply of the sensor. The optimal working distance of 50cm between the object and the lenses can be assigned by a laser system that calculates the distance between the object and the lenses by a trigonometric measurement. A novelty in handheld HSI-systems is the integrated illumination consisting of 70 broadband VIS/NIR high-power LEDs mounted on the back of the HC next to the sensor lenses (Fig. 2). Further technical details of the HC and the installed sensors are given in Table 1.

The HC is operated via a 7" full high-definition (HD) LED touch screen and two physical buttons for booting the system and triggering the measurement. Besides setting options, such as exposure and gain, the user interface includes processing functions for the acquired data. By measuring an image-filling reference material, this measurement can be set as a "global reference" for pixel-by-pixel normalizing of the hyperspectral image. If the reference material is placed within the measurement of an object of interest, a round area of interest marker can be set at that location and adjustable in size to match the

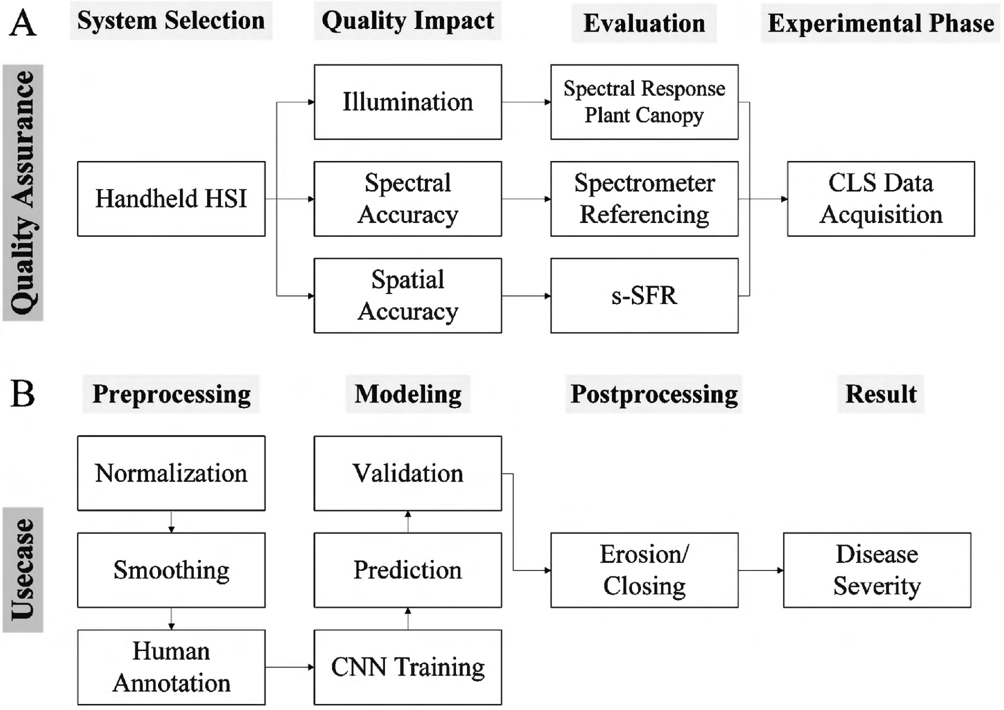

Fig. 1 Quality assurance pipeline of hyperspectral imaging (HSI) systems with a convolutional neural network (CNN) supported data analysis concept. In Fig. 1 **A** an evaluation of three crucial parameters is presented. The spatial accuracy was tested by analyzing the sine-wave based spatial frequency response (s-SFR). To investigate the artificial illumination, spectral responses of plant canopy's were compared. The spectral accuracy of the HSI-system is validated by compering measurements of a calibration material with a spectrometer. After evaluating the parameters and adapting the measurements according to the results, the HSI-system is used to measure the disease progression of Cercospora leaf spot (CLS) infected sugar beet plants. In Fig 1 **B** the concept for CNN supported HSI data analysis is presented. In the first step common spectral and image preprocessing steps such as normalization and smoothing are conducted. For supervised machine learning, the training data set has to be humanly annotated to define certain classes of interest. After training the model with humanly annotated data, the model can predict the classes for the whole dataset, which can be validated by comparing the results with humanly annotated data which has been excluded from the training process. To enhance the models' performance, image postprocessing steps such as erosion and closing have been applied. After postprocessing the CLS disease severity has been derived from the model output

Fig. 2 Blackmobile front and back view. The frontside shows a 7" LED touchscreen that displays the user interface running the hypercube view widget. The backside shows the broadband VIS/NIR LED array, the lenses of the hyperspectral and RGB camera, and the laser system for vertical alignment

Table 1 HAIP Blackmobile technical details sensors

Parameter	HSI	RGB
Sensor	CMOS	CMOS
Sensor size	5568*3132μm	7680*4320μm
Sensor resolution	2 Megapixel	8 Megapixel
Pixel size	2.9*2.9μm	2.0*2.0μm
Focal ratio	1.8	1.8
Focal length	12mm	12mm
Spectral range	500-1000nm	NA
Spectral resolution	5nm	NA
Spectral bands	100	NA
Exposure	1000-5000μs	Auto-Exposure/0.1-33.3s
Gain (analog)	1-15.5 (Multiplier)	1-15.5 (Multiplier)
Image resolution	640*480px	3840*2160px
Data depth	10bit	8bit
Peak signal-to-noise ratio	40.8dB	39dB
Working distance	45-55cm	45-55cm
FOV at 50cm distance	22*16.5cm	33*18cm
Data format	ENVI	JPG

size of the reference material. By selecting this marker as the "global reference," an average spectrum of the adjusted area of the marker is calculated and set as the global reference value used for normalizing of each pixel in the selected hyperspectral image. Both normalization methods calculate the reflectance following the formula.

$$reflectance = \frac{HSI - sensordarkcurrent}{referenceHSI - sensordarkcurrent}$$

Due to technical variability such as heat or voltage, the noise produced by hyperspectral sensors varies with each measurement. To eliminate these differences during the normalization process, a dark current is recorded with each measurement and subtracted from the HSI, respectively. The normalized hyperspectral image can be examined in the widget, and multiple markers of interest can be set in the widget to display the average spectrum of the set area. The acquired data is saved as an ENVI formatted hyperspectral cube and the RGB image as a JPG image, which is automatically recorded before the spectral measurement starts, if enabled. Further technical details of the camera and its operating software are given in Table 2.

Measuring setup

The framework of the measurement chamber is made of aluminum profiles and has a dimension of 1.5*1.5*2m (L*W*H). Light interference in the measurement chamber was prevented by blackening the walls with polyurethane-coated black nylon fabric (Blackout Fabric, Thorlabs Inc., Newton, United States), the floor was covered with a matte black lacquered wooden panel. The ceiling was left open to ensure adequate ventilation and to prevent heat stress to the plants (Fig. 3).

The external halogen illumination consisted of four 70*watt* voltage stabilized quartz tungsten halogen lamps

Table 2 HAIP Blackmobile technical details of the operating software and system hardware

Parameter	Value
User interface	HAIP Blackmobile Software
Operation System	L4T 32.5 - Ubuntu 18.04 - Linux kernel 4.9
Embedded Computer	NVIDIA® Jetson Nano™
CPU	Quad-Core ARM® Cortex® - A57 MP core
GPU	NVIDIA Maxwell™, 128 NVIDIA CUDA®
RAM	4 GB 64-bit LPDDR4
Storage integrated	16GB eMMC 5.1-flash storage
Storage external	256GB SD
Battery	Li-Ion 14.4 V
Operational time	100 measurements
Display and operating unit	7" LED touch screen (full HD) and 2 buttons
Serial Connection and power socket	USB type-c
WIFI	2.4 GHz IEEE 802.11
Supply voltage	20VDC
Size (L*W*H)	250*165*70mm
Weight	1.5kg
Operational temperature	10 − 30°C
Integrated illumination	Broadband VIS/NIR LED array
LED quantity	70

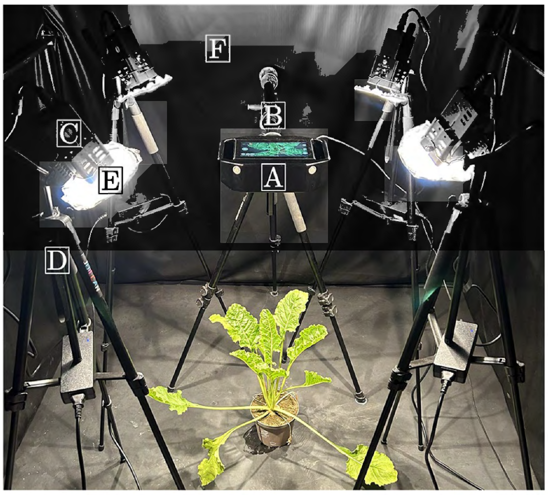

Fig. 3 Measurement setup for hyperspectral imaging. **A**: HC, **B**: Tripod HC (height: about 80*cm*), **C**: External illumination, **D**: Tripod illumination (height: 108*cm*, angle: 40°), **E**: Diffusing screen, **F**: Blacked out measurement chamber (dimensions: 1.5*1.5*2*m* (L*W*H))

(Illuminator Lamp, Malvern Instruments, Malvern, United Kingdom). To ensure evenly distributed illumination, round diffusing screens were fixed to the lamps with metal wires at a distance of 2*cm*. (nylon silk with an approximate light reduction of 1.0 f-stop). The lamps were mounted on 137*cm* tripods at an angle of about 40°. The tripods were adjusted to a height of 108*cm* above the ground and placed in a rectangle around the centre in a measurement chamber. The HC was mounted on an additional tripod. An barium sulfide plate with a dimension of 43*43*cm* (Specim Spectral Imaging Ltd., Oulu, Finland) was used as an image filling white reference material for all measurements.

Plant material

Two sugar beet varieties were chosen for the experiments. BTS 8750 (Betaseed GmbH, Frankfurt, Germany) for investigating the quality of the hyperspectral illumination, and Vasco (SESVanderHave, Tienen, Blegium) for phenotyping plant disease dynamics. The seeds were sown 1*cm* deep in polypropylene pots filled with Fruhstorfer soil type P 25 (HAWITA Gruppe GmbH, Vechta, Germany). After seven days, 15 germinated seedlings of the variety BTS 8750 were individually transplanted into 1*l* round polypropylene pots filled with fertilized sandy topsoil (Gustav Lehmann Mörtel- u. Kieswerke GmbH, Burgdorf, Germany). The sugar beet plants were then cultivated for 66 days (14:10*h* light/dark photoperiod, $25.5 \pm 5.5^{\circ}C$, 55.4±18% relative humidity and about $225\mu mol/[sm]$ full spectrum light) in the greenhouse until they reached BBCH-Code 19 [32]. During cultivation, the plants were watered daily and fertilized every three weeks with 50*ml* of a 1:40 liquid fertilizer (liquid universal fertilizer, EDEKA, Hamburg, Germany) tab water mixture.

For the usecase data assessment 14 sugar beet plants of the variety Vasco were split into two variants: inoculated and non-inoculated. The inoculated variant was treated with liquid *Cercospora beticola* spore suspension produced from the strain 145 (BASF SE, Ludwigshafen, Germany) by spraying 7*ml* of the suspension with a concentration of ca. 30,000 spore per millilitre equally distributed on abaxial and adaxial side of the sugar beet leaves twice, in a time spawn of one hour. Afterwards the plants were covered with foil and the temperature in the greenhouse was increased to a minimum of $28^{\circ}C$ for six days. After six days the foil was released and the temperature was decreased. The sugar beets were then cultivated for the time of the data collection at $26.6 \pm 6.1^{\circ}C$, 55.2±18.8% relative humidity and ca. $225\mu mol/[sm]$ of full spectrum light.

Measurements

Spatial quality assessment

The spatial resolution of the HC was tested using the international standard method called sine-wave based spatial frequency response (s-SFR) for measuring resolution and image sharpness of digital cameras [28]. Therefore, a sinusoidal Siemens star SFR chart with 144 cycles (ISO 12233:2023) [33] was measured with the HC at different working distances. Before measuring the SFR chart, the white reference was measured with the external illumination at a distance of 50*cm* and with an exposure time of 1000μs and a gain of 12. To replicate the referencing scheme of a plant measurement, the referencing measurement was done only once at the optimal working distance. The varying working distances are resembling the z-axis latitude of a plant canopy. The distance of the s-SFR chart to the lens was varied ± 5, 7.5 and 10*cm* from the optimal working distance of 50*cm* for the different measurements to simulate a plant canopy height of 20*cm*. The exposure time for the s-SFR chart measurements was set to 5000μs to increase the sensitivity of the HSI-system.

Spectral quality assessment

To validate the spectral accuracy of the HC, a calibration material (ColorChecker Classic, Calibrite LLC, Wilmington, USA) was measured with the same setup as described in section 2.2. The calibration material and the white reference was measured at the optimal working distance of 50*cm* with the external halogen illumination. In order to compare measurements with a high resolution non-imaging spectrometer (ASD Fieldspec Hi-Res, Malvern Instruments, Malvern, United Kingdom, software: RS_3^{TM}) the calibration material and the white reference were measured with the same exposure time ($5000 \mu s$) and gain (3.1) to enable comparison between the spectrometer and the HC. Prior to measurements, the spectrometer was warmed up for $30 min$ and a contact probe was mounted. Reference measurements were made by placing the contact probe on the same white reference used for the HSI reference measurement. For the measurements of the calibration material with the spectrometer, the contact probe was pointed into the tiles of the calibration material and 10 repetitions of each tile were assessed.

Illumination quality assessment

The variability of the integrated high-power LED array of the HC was investigated for plant phenotyping routines and compared to external halogen illumination. For this purpose, sugar beet plants were measured with the HC illuminated by the integrated LED array and external halogen lamps respectively. Therefore, five sugar beet plants were placed in the center of the rectangle formed by the halogen illumination tripods in the measuring setup (Fig. 3) on the same position for individual measurements. The HC was leveled at a distance of $50 cm$ to the approximate vertical center of the plant canopy. The distance between the halogen lamps and the canopy was about $75 cm$. Before measuring the plant material, the white reference was measured with the integrated and external illumination at a distance of $50 cm$ and with an exposure of $1000 \mu s$ and a gain of 12. The exposure time for the measurements was set to $5000 \mu s$. Each plant was measured with the external and integrated illumination in exactly the same position, respectively.

Subsequently, the selected plants were measured with the non imaging spectrometer. Five leaves of each plant were randomly selected and the adaxial side of the leaves was measured in the middle next to the leaf vein with the leaf clip attachment of the spectrometers contact probe.

Time series measurement of disease dynamics

The optimal working distance of $50 cm$ between the object and the lens was adjusted to the vertical center of the sugar beet canopy. The external halogen illumination setup was adjusted to account for the different heights of the sugar beet pots, resulting in different sugar beet canopy distance. The height of the halogen lamps was adjusted to $79 cm$, which resulted in a distance of approximately $60 cm$ between the lamps and the sugar beet canopy and an angle of approximately 45°. Plants were measured with the HC one day before inoculation and 7, 11, 14, 21, 24 and 31 days after inoculation (dai). As reference data, disease severity was visually assessed as a percentage of infected leaf area via human expert rating [34].

Data analysis

Spatial resolution

The acquired hyperspectral images for spatial quality assessment, considered as raw data, were processed in R (version: 4.3.1) [35] and RStudio (version: 2023.12.0+369, Posit PBC, 2023) using the package "hsdar" (version 1.0.4) [36]. First, the hyperspectral images of the plant material were normalized pixel by pixel with the corresponding illumination reference measurement using the following formula.

$$reflectance = \frac{HSI - sensordarkcurrent}{referenceHSI - sensordarkcurrent} \times \frac{exposure\ reference}{exposure\ data}$$

Then RGB images of the normalized hyperspectral images were visualized (png, version: 0.1-8) [37]. The wavelengths chosen for RGB visualisation were $525 nm$, $550 nm$ and $600 nm$. The RGB images of the different measuring distances were analyzed in the MathWorks tool IE-Resolution (Single Star Version, Image Engineering, Frechen, Germany) [38] to calculate the limiting resolution. The tool divides the sinusoidally modulated starburst pattern into 8 segments and calculates the Nyquist-frequency by a modulation transfer function (MTF) for each segment. In addition, the sum of the modulation for each distance and each segment was calculated to compare the sharpness of each segment within a working distance. The standard deviation of the modulation between segments was also calculated for each working distance.

Spectral accuracy

The hyperspectral images of the color calibration material measurements were normalized as described in section 2.5.1. Arrays of size $60*60 px$ were extracted from different calibration material tiles of the hyperspectral images. From each array an average spectrum of the 10 measurement repetitions was calculated in R (asdreader, version: 0.1-3) [39]. For further analysis, only spectral bands measured by both sensors, the spectrometer (with a spectral resolution of $1 nm$) and the HC (spectral resolution: $2 nm$) were considered. A Pearson correlation was calculated between the measurements of each tile from the HC and the spectrometer using the "cor" function of the "stats" package (version: 4.3.1) [35]. Differences between the measurements from the HC and the spectrometer in reflectance of the considered spectral bands were calculated for each tile by subtracting the reference values of the spectrometer data from the HC data. For graphical presentation, of the results of this research the “ggplot2” package (version: 3.4.4) [40] was used.

Illumination comparison

The hyperspectral images of the illumination system comparison were normalized as described in section 2.5.1. The sugar beet canopies of the normalized data were segmented by creating two binary masks with the optimized soil adjusted vegetation index (OSAVI) and the difference vegetation index (DVI) [41, 42] with the following formulas.

$$OSAVI = 1.16 \times \frac{800nm-670nm}{800nm+670m+0.16} \quad ;$$

$$DVI = 800nm - 680nm$$

Both masks were merged to increase the segmentation performance using the “OR” operator [43]. After merging the masks, an image erosion was performed (mmand, version: 1.6.3) [44] to eliminate false segmented individual pixels. In addition, an average spectrum and the standard deviation of the average spectrum were calculated for each merged mask of the sugar beet canopy. Ten reference measurement repetitions of the non-imaging spectrometer per leaf, were averaged and the arithmetic mean of five leaf measurements per plant was calculated to estimate a representative spectrum for each of the five sugar beet canopies.

Image preprocessing and CNN training for CLS disease severity estimation

Plant masks were plotted for human annotation of the dataset which had been separated in training and test dataset for machine learning. After normalization as described in section 2.5.1, the first 2 spectral bands have been deleted due to sensor noise for further analysis. The Savitz-Golay smoothing filter [45] was applied to the hyperspectral images using the R package “gsignal” [46] (filterorder = 3, filterlength = 5). The smoothing filter was applied to reduce noise in the spectral data and to compute the first and second derivatives of the smoothed hyperspectral images. Pseudocolor images of the OSAVI index, as described in Section 2.5.3, were plotted with the smoothed, normalized data to improve the visibility of borders between different objects which supports human class annotation for machine learning. Three classes were defined for annotation of the pseudocolor images: “background”, “healthy” plant tissue, and CLS “diseased” plant tissue. The pseudocolor images of 2 inoculated and 2 non-inoculated sugar beet plants of each measurement date were randomly selected and the pixels of the images were annotated to the three defined classes using the software GIMP (version: 2.10.36, The GIMP Team). This resulted in the establishment of 3 separate masks of the defined classes. The training and test data sets were separated by measuring time points: 2 of the 8 time points (14 and 24 dai) were kept for the test dataset and the other 6 (0, 7, 11, 18, 21, 24 and 31 dai) for the training dataset. This division was made to establish two completely unknown disease progression states (early and late) in the time series for the CNN to test its performance. Which resulted in assigning 8 hyperspectral images to the test data and 24 hyperspectral images to the training dataset. The masks of the training dataset were used to generate matrices from the arrays of normalized and smoothed hyperspectral images by summarizing the reflectance values of the smoothed hypercube, the first and second derivatives for each pixel. The matrices of the training data set were then accumulated and outliers were removed (Rlof, version: 1.1.3) [47] by deleting the top 1% of the maximum and minimum values of each class. After removing the outliers, the three classes were balanced in terms of their total number of pixels to prevent the model from becoming biased towards one class. Since the total number of pixels of the diseased class is the lowest, 2 times the total number of pixels of the diseased class was set as the downsampling size for the other two classes.

The preprocessed training data set was then used to train a CNN specifically designed to analyze spectral data [30]. The implemented CNN focuses on analyzing and classifying the spectral data of each pixel. The input data were individual pixels with the corresponding spectral values combined from the smoothed spectrum and its first and second derivatives. The architecture of the CNN was adapted as described in [48] (retrieved: 2023.11.27). In addition, the batch size was set to 1024 pixels per epoch and the total number of epochs was set to 50. For the training and testing process, the smoothed hypercubes and the first and second derivatives were summarized for each pixel. 20% of the training data was retained to validate the training process. The training process was focused on the disease and background classes to better discriminate these classes the “classweight” function of the R package “keras” (version: 2.13.0) [49] was used. Furthermore, the adam optimizer with a learning rate of 0.001 was used for the training process. The trained model was then used to predict the affiliation of the pixels to three defined classes of the entire dataset which was centralized and scaled by the coefficient calculated in the training process. The trained model then predicted the affiliation of each pixel to the three defined classes from the summarized spectral values. With the predicted affiliation of each pixel, pseudocolor masks of each hyperspectral images were generated. To improve the performance of the CNN, post-processing steps were performed. First, the masks of the diseased and healthy classes were merged, then an image closing and erosion (mmand, version: 1.6.3) [44] was conducted to assign the mixed edge pixels to the class background and to assign single misaligned diseased pixels to the class "healthy". A confusion matrix for the metrics precision, recall, specificity and F1 was calculated to analyze the performance of the disease severity estimation pipeline by comparing the predicted and post processed pixel class affiliation of the test data set compared to the human annotated masks.

With the final predicted and post-processed masks, the disease severity of each plant and each time point was calculated using the following formula which enumerates the leaf area affected by the disease [50].

$$disease\ severity = \frac{pixel\ count:\ diseased}{pixel\ count:\ healthy + pixel\ count:\ diseased} \times 100$$

In addition, the disease severity values of each time point from either the calculated CNN results or the visual assessment were checked for outliers by Dixon's extreme value analysis [51] with a significance level of 5%, which was performed in R using the outliers package (version: 0.15) [52]. A single outlier was detected in the CNN derived disease severity data set at 18 days after inoculation and removed for further analysis. To obtain comparable hyperspectral images, all plants were measured from the same perspective. Since plants grow differently even when grown under the same conditions, important parts of the plant may be missed in the measurements, leading to outlying measurement results. In addition, a Wilcoxon signed rank test [53] was performed in R with the "coin" package (version: 1.4-3) [54] to test for statistically significant differences between the disease severity of inoculated and non-inoculated variants for each measurement time point after 14 days post inoculation, which was the starting point for CLS symptom development. The mean disease severity for each variant at each time point and the standard deviation were calculated.

Table 3 Image sharpness of the HC at working distances between 40-60*cm*. SD shows the standard deviation between the summed modulation transfer function results for each segment

Distance[*cm*]	Nyquist frequency	Best segment (∑MTF)	Worst segment (∑ MTF)	SD
40	239.5	5 (154.8)	7 (31.2)	43.4
42.5	239.5	5 (122.0)	7 (36.0)	28.3
45	238.5	1 (103.9)	7 (43.0)	19.7
50	238.5	5 (63.5)	7 (29.7)	12.5
55	237.5	8 (36.4)	2 (12.7)	9.0
57.5	235.5	8 (30.1)	2 (8.2)	8.3
60	228	8 (23.4)	2 (5.0)	7.5
50 (4K)	1080	3 (297.5)	5 (237.8)	19.4

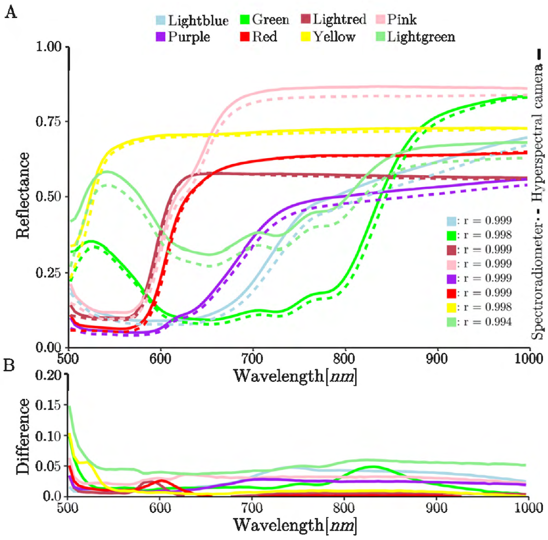

Fig. 4 Spectral accuracy results. Spectral response of 8 tiles of the calibration material measured by the HC and the spectrometer are shown (**A**). The colors correspond to the colors of the measured calibration material tiles. "r" values present Pearson correlation coefficients between measurements from the spectrometer (reference) and the HC of the corresponding tiles. In addition, the differences in reflectance between the HC measurements and the spectrometer measurements are presented (**B**)

Results

Spatial resolution and image sharpness

The Nyquist frequency of the hyperspectral images measured at the different working distances with the HC between 40-60*cm* (Table 3) slightly increased with narrow working distances and slightly decreases with further working distances. The Nyquist frequency of the image recorded by the RGB sensor (1080) was exactly half the sampling rate of the RGB sensor (2160). The standard deviation between the segments of the HC increased as the working distance decreased. Furthermore, the HC presented differences between the segments by the summed modulation within a working distance, which allows to distinguish between sharpness of the different segments. Images measured in narrow and optimal working distances constitute mostly segment 5 as the sharpest and segment 7 as the most blurred segment. The results of the increased working distance identified segment 8 as the sharpest and segment 2 as the most blurred segment.

Spectral accuracy of the hyperspectral camera

The displayed color calibration material measurements presented strong similarities between the HC and the reference measurements of each calibration material color tile with an r >0.99 for all the measured color tiles of the calibration material. In addition, the differences between the HC and spectrometer measurements were all less than 0.1 reflectance between 512-1000*nm* (Fig. 4B).

Illumination system quality

Differences in the arithmetic mean of reflectance values were identified around 677*nm* in the VIS and around 752*nm* in the NIR. (Fig. 5A). The spectral curve of the spectrometer reference measurement corresponds to the curve of the halogen-illuminated measurements. However, the reference curve has an increased offset of approximately 30% compared to the halogen-illuminated curve. The LED illumination caused high standard deviation at 525*nm* and 1000*nm*, which reaches more than 0.1 reflectance at approx. 720*nm* (Fig. 5B). The spectrometer measurements constantly had the lowest standard deviation over the entire measured spectrum. Furthermore, the LED illumination produces the highest spatial reflectance variance over the sugar beet canopy in all three spectral bands (Fig. 5C) compared to the halogen illumination. In particular, the spectral band at 752*nm* of the LED illumination hyperspectral images includes pixels located at the highest leaf base with reflectance values that are off scale and therefore displayed in white.

Cercospora leaf spot disease severity prediction

The CNN and the human expert detected the first symptoms of CLS on the inoculated plants 18 days after inoculation (Fig. 6A). During the following seven days, the mean disease severity increased by 4.5% according to the expert rating and 0.57% according to the CNN. At the final day of measurement, the disease severity was 8.57% for the expert rating and 3.49% for the CNN pipeline. The disease severity rating by the expert for the non-inoculated variant was zero percent throughout the observation period. The CNN pipeline showed a low false positive rate for disease severity results of the non-inoculated variant, with a maximum of 0.081%. The standard deviation increased for both assessment methods as the CLS infection progresses. The inoculated and non-inoculated variants showed statistically significant

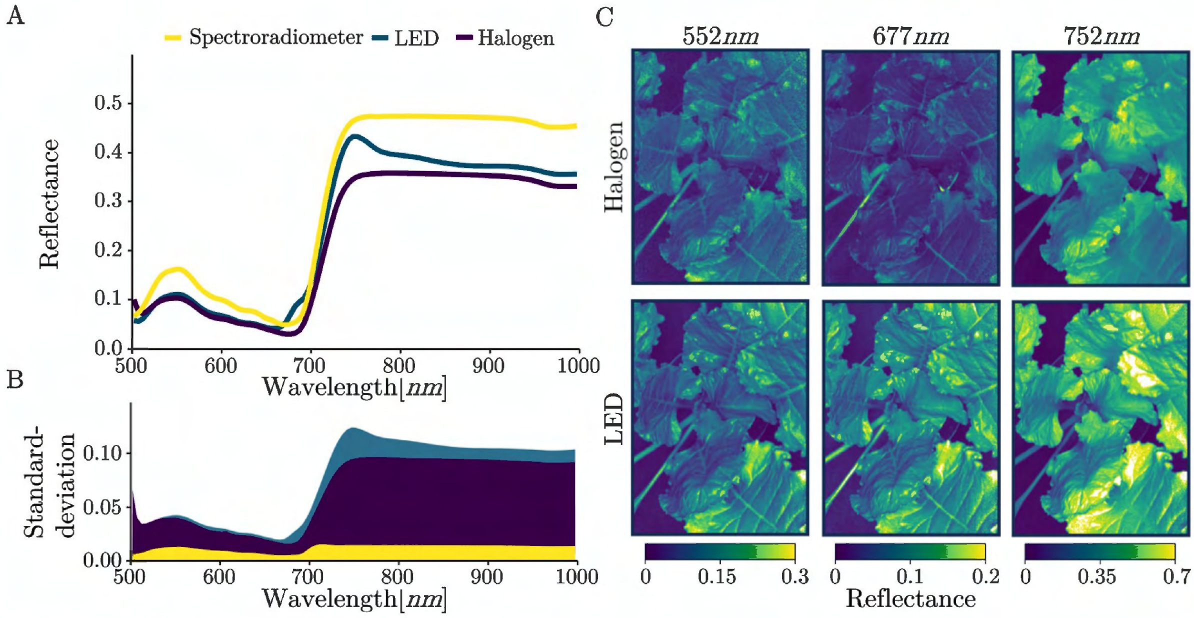

Fig. 5 Comparison of illumination systems by sugar beet canopy spectral responses. The arithmetic mean of the five averaged canopy reflections between 500 and 1000*nm* of the two different illumination systems and the spectrometer measurement is shown (**A**). In addition, the arithmetic mean of the standard deviations of the reflectance of the averaged canopy masks and the averaged spectrometer reference measurements is displayed (**B**). Furthermore, the variance of the measured reflectance over a plant canopy of the spectral bands 552*nm*, 677*nm* and 752*nm* is presented (**C**)

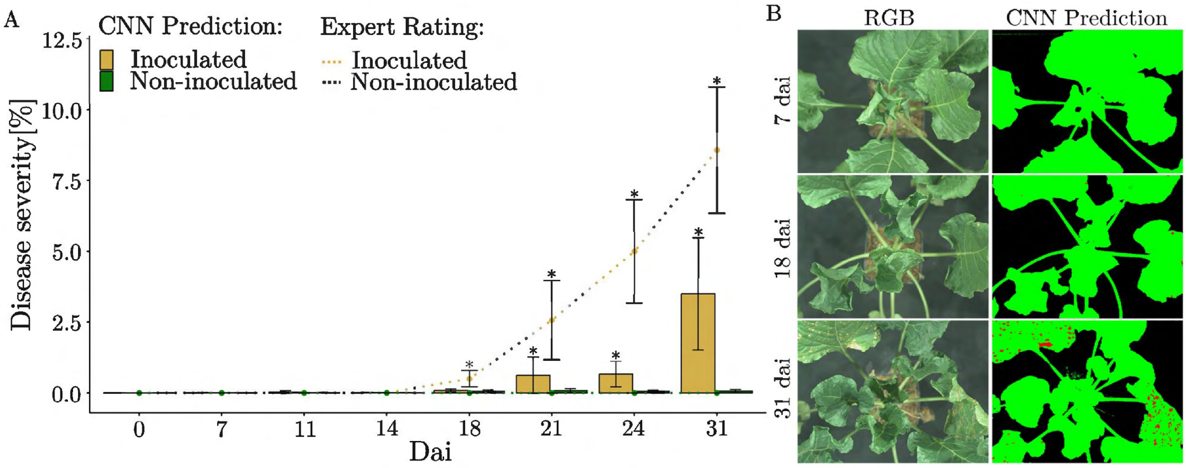

Fig. 6 Disease severity results from CNN and expert scoring. Bars show disease severity from the CNN pipeline and dotted lines show the expert assessment. Error bars show ± standard deviation and stars show statistically significant difference between variants at a given time point at a significance level of $p<0.05$ (**A**). RGB images from the 4K sensor of the HC and colored masks from the CNN pipeline of the three classes background (black), healthy (green), disease (red) at three selected measurement times (early, intermediate, late) of a replicate of the inoculated variant are shown (**B**)

Table 4 CNN performance matrix of the pixel wise classification from the test dataset

	Precision	Recall	Specificity	F1
Background	0.98	0.98	0.98	0.98
Diseased	0.62	0.60	0.99	0.61
Healthy	0.98	0.98	0.98	0.99

differences for both rating methods at 21, 24, and 31 days after inoculation. The CNN pipeline pixel affiliations of one repetition of the inoculated class to the RGB images of the same plant at the respective time points are compared (Fig. 6B). The RGB and pseudo color images of the CNN pipeline display comparable infection patterns at all time points upon visual analysis.

The CNN has a precision of over 98% for the background and healthy classes. For the diseased class, the precision is approximately 62% (Table 4). The false positive rate of pixel affiliations in falsely predicted classes is consistently below 5% for every class combination except when healthy is predicted but truly diseased, which has a false negative rate of 33% (Table A1). The CNN consistently achieves over 98% in classifying healthy and background pixels in terms of recall, specificity, and F1 score. In the classification of diseased pixels, the specificity is above 99% and the precision, recall and F1 score are above 60%.

Discussion

Hyperspectral imaging quality assurance for plant phenotyping

Accurate imaging of three-dimensional (3D) objects such as plants is challenging, especially in the field of HSI. Every image has the phenomenon of edge pixels, which contain a mixed spectral signature of the overlapping objects. In the case of plant phenotyping, for example, this can occur at the boundary between leaves and background or healthy leaf tissue and diseased leaf tissue. In conclusion, high image resolution resulting in a small ground sampling distance (GSD) is advantageous for segmenting objects in a hyperspectral image. However, this requires an adequate image sharpness. The Nyquist frequency takes the image sharpness into account and describes the resolution limit of an image and therefore also the resolution limit of an imaging system [28]. Apart from the technical limitation of the system, the GSD can only be influenced by the measuring altitude. The image sharpness, on the other hand, is mainly influenced by the focal ratio of the camera, which is fixed for the HC and determines an optimal working distance of $50cm$, resulting in a GSD of $0.2mm$ [55]. Even though an optimal working distance has been determined, changing the distance may be necessary in certain scenarios, such as in including the entire plant in the hyperspectral image or in reducing the GSD to measure small objects.

The critical sample value of half of the maximum image pixel height (240) was narrowly missed by the HC at any working distance, resulting in a small aliasing and loss of information [56]. By changing the working distance ± 10*cm* the GSD changed ±0.04*mm* which can be the reason for the slight variation in the Nyquist frequency. The technical aspects of the HC concerning the low focal ratio would not assume any remarkable changes in the image resolution between at least ±5*cm* from the optimal working distance which is corresponding with the image resolution test results. Low focal ratios are associated with a wide image focus which is beneficial for measuring 3 dimensional objects. The differences in sharpness between the segments within a working distance could have been caused by faulty technical components of the HC. Defects related to the hardware of the sensor chip would have resulted in a locally uniform degradation of quality at any working distance. Since the blur of the segments varies over the working distances, defects in the installed lens may have caused this problem. Point defects on the lens can occur during the manufacturing process, such as bubbles and uneven coating, and during the manufacturing and assembly of the camera [57]. The position of the sinusoidal Siemens star chart under the lens of the HC was automatically corrected by the MathWorks tool IE-Resolution. Shifting the angle between the chart and the lens when the working distance was adjusted might have caused the shifting of the weak spot concerning the sharpness. In addition to the technical aspects of the camera, the resulting image resolution and sharpness is affected by the signal processing within the system. The actual sensor resolution of the HC is 1920*1080*px*. The stored hyperspectral image only has a resolution of 640*480*px*, which means that spatial binning is applied to probably increase the spectral signal-to-noise ratio [58].

In summary, the international standard method for the evaluation of image sharpness of digital cameras [28] can be considered to be applicable to HSI-systems. Since the method evaluates contrast, simple black and white images can also be evaluated, allowing the analysis and comparison of the image sharpness of each spectral band measured by an HSI-system, if needed.

To investigate the spectral accuracy of the HC, the spectral measurements of a calibration material for digital cameras were compared to the spectral measurements of the same calibration material of a high spectral resolution non-imaging spectrometer. The average Pearson correlation between the measurements of the 8 tiles of the calibration material resulted in a correlation of about 99.8%, certifying the installed spectral sensor in the HC a high accuracy. The reflectance differences of all measured tiles between 512-1000*nm* are below 0.1, which corresponds to a high average correlation. However, between 500-512*nm*, the differences increase due to the low signal-to-noise ratio of the first measured bands of the HC. This is a common problem in spectroscopy, often resulting in the elimination of the first noisy spectral bands for analysis. The low irradiance of the halogen illumination in the blue light region commonly used for HSI exacerbates the effect, as shown by the distortion of the spectrum in the affected spectral region [25]. The slight spectral shift between the HC and the reference measurements which occurs for most of curves may be caused by technical differences in the spectral measurements or by different processing of the measured signals. In general, comparing the spectral measurements of a calibration material's spectral response with those of a reliable spectrometer is an easy-to-apply method for evaluating the accuracy of an HSI-system.

Illumination for hyperspectral imaging

The accuracy of HSI is heavily influenced by the light conditions during measurements [25, 59]. Stable and sufficient illumination is crucial for generating high-quality data in laboratory setups under controlled conditions. In-field measurements are the most reliable source for extracting plant traits because environmental influences are considered. Generating high-quality and accurate hyperspectral images in the field is challenging due to unpredictable and unstable natural light conditions. To stabilize the light conditions for hyperspectral measurements, the tested HC supports illumination by an integrated light source. The integrated LED light of the HC was evaluated by comparing measurements of sugar beet plants in controlled conditions with common halogen-illuminated and non-imaging spectrometer measurements.

When comparing the courses of the spectral curves, it is noticeable that the spectrometer and halogen-illuminated measurements exhibit similar trends. However, there is a significant shift between these curves, which can be attributed to the 3D structure of the plant. The spectrometer measurements were conducted using a plant probe with a leaf clip attachment that flattened the leaf for the measurement, resulting in a two-dimensional equally illuminated measurement. Creating equally distributed illumination on a 3D structure is challenging. Additionally, combining this with a two-dimensional normalization for hyperspectral measurements, which is still the state of the art in the field of plant phenotyping [12, 14, 60, 61], shifting of the spectral response can occur. Research has been conducted to correct the calibration of HSI by taking into account the plant geometry [12] and shadowing effects [62]. Though, both approaches do not take into consideration the light distribution of the illumination source in the set up. Another approach to correct this issue would be to measure the calibration material at different altitudes of the z-axis and correspond this to the depths of the hyperspectral image in the normalization process. This can already be achieved with tools like Depth Anything [63].

Between 650-775*nm*, the spectral curves of halogen and LED illumination significantly diverge, exhibiting two abnormal peaks in the LED illumination measurements at approximately 677*nm* and 752*nm*. Additionally, certain hotspots exceeding a reflectance value of 1.0 are visible in the reflectance heat maps of LED-illuminated hyperspectral images. These abnormal spectral responses may have resulted from mirroring effects caused by the non-diffuse integrated LED light which incidents at a 90° angle. To prevent mirroring effects, the halogen illumination was mounted at an angle of approximately 45° to the plant, and diffusing screens were attached. The lambertian property of leaves is generally dependent on surface characteristics, particularly the amount of epicuticular wax, which can enhance mirroring effects [64]. In principle, LEDs as an illumination source for HSI imply a lot of advantages compared to halogen illumination such as cost effectiveness, longer lifetime, less heat emission and increased irradiance in the blue light region [24, 25, 65]. However, the comparison of illumination sources in this research highlights the importance of evenly distributed diffuse illumination for HSI.

Proof of concept: Neural network supported CLS disease severity estimation

In addition to the HSI-system quality evaluation pipeline, this research proposes a concept for a CNN multiclass classification of quality assured hyperspectral images in the context of phytopathology. A CNN specifically designed for the analysis of spectral data [30] was trained for the detection of CLS diseased pixels. The trained CNN was used to estimate the disease severity of CLS-infected plants in a time series and compared with visual expert assessments. The CNN underestimated the disease severity over the whole time series compared to the expert rating. However, the use of human expert ratings as reference data has been widely discussed in the literature for the last 100 years [66]. To establish a true image-based reference dataset, the entire dataset must be classified by human annotation. With the increasing amount of data in high throughput plant phenotyping, this approach is impractical. The performance of the trained CNN for multiclass classification shows high precision, recall, specificity and F1 for the healthy and background classes, which means the CNN is very accurate in segmenting the vegetation from the background in a hyperspectral image. In addition, the diseased class has a high specificity, which describes the relationship between the true negative and all negative pixels of this class. Precision, recall and F1 for the diseased class are above 0.6, which is a positive result for disease classification. The presented CNN performance for the classification of the diseased class explains the possible underestimation of the CLS disease severity. The early symptoms of CLS are small reddish-brown lesions with a white to grayish center in which black pseudostroma are formed. As the infection progresses, the lesions grow and coalesce, which can lead to a complete collapse of the leaf [21]. Detecting early symptoms using a pixel-by-pixel approach is difficult as a single lesion at this stage may contain more edge pixels with mixed spectral responses than clear central lesion pixels. In addition, CLS induced non-visible spectral changes may occur that are not considered in human annotation and are also overrepresented in early stages of infection. Possible non-visible symptoms around the lesions prohibited human-driven post-processing steps such as mask closure applied to the diseased class. An increased performance of the CNN on more advanced infection stages is expected. In addition, an increased number of repetitions, apart from a proof-of-concept trial, which consequently enlarges the training dataset, will result in a reduced standard deviation of the disease severity estimation and presumably an improvement of the CNN performance as well. Additionally, the not adjustable spatial binning of the HC reduced the resolution from 1920*1080*px* to 640*480*px* of the hyperspectral image which consequently reduces possible precision of localizing symptoms in the spatial dimension. Furthermore, changing the pixel-by-pixel disease classification approach to a semantic segmentation approach by using a mask r-cnn or a U-net [67, 68] would focus the analysis on the spatial arrangement of pixels. The benefits of focusing the analysis on the spatial rather than the spectral information need to be tested. In summary, the proposed concept consists of a reliable pipeline for estimating the disease severity of CLS based on quality assured hyperspectral images under controlled conditions.

Conclusion

A neural network supported analysis concept was successfully applied to quality assured hyperspectral imaging data for a phytopathological usecase. Furthermore, the assessment of spatial and spectral accuracy of an HSI-system by the proposed pipeline supports decision making for the selection of the right HSI-system for the required application. Furthermore, internal signal processing, such as spatial or spectral binning, can be evaluated and adjusted for the desired hyperspectral image quality. Illumination for HSI in coherence with real radiometric correction rather than simple normalization is still complex, especially for the measurement of 3D objects. The results confirm the importance of diffuse and uniform illumination for HSI. If the results of the spectral accuracy assessment and the illumination testing are compared, the effect on the spectral response of measuring 3-dimensional objects which are based on two-dimensional normalization is presented. For physically accurate radiometric correction of 3D measured objects the light distribution in the z-axis must be considered. Quality assured hyperspectral images can reduce limitations in the data analysis and provide high quality data sets for plant phenotyping. The presented concept for CNN supported CLS disease severity estimation based on hyperspectral images was successfully implemented. Furthermore, reducing spatial binning for pixel-by-pixel classifications, or switching the approach to a semantic segmentation classifications by using a Mask R-CNN or U-Net instead of a 1-dimensional spectral response focused CNN can enhance the performance.

In conclusion, the quality assurance pipeline is independent concerning the type of the HSI-system because it is data based, analysing the resulting hyperspectral image. Therefore, it can be easily applied on any other HSI-system to assess and assure the presented quality parameters.

Appendix A

See Table 5

Table 5 CNN confusion matrix of the pixel wise classification from the test dataset

Prediction/Target	Background	Diseased	Healthy
Background	1148565	152	22040
Diseased	41	1985	1272
Healthy	13861	1055	1268629

Author contributions

Conceptualization: JD, SP. Methodology: JD, AB, SP. Investigation: JD. Visualization: JD. Funding Acquisition: SP, AKM . Project Administration: AKM. Supervision: AKM, SP. Writing - Original Draft: JD. Writing - Review & Editing: JD, AB, AKM, SP

Funding

Open Access funding enabled and organized by Projekt DEAL. This work has been funded by the Deutsche Forschungsgemeinschaft (DFG, German Research Foundation) under Germany's Excellence Strategy-EXC 2070-390732324. Additionally, this study was supported by federal funds and by the ELER Fond of the European Union for development of rural space in Lower Saxony and Bremen 2014-2020 (PFEIL) as part of the PRo-MAPPER project (EIP AGRI - 276032540210329). Further, the project was partly supported by funds of the Federal Ministry of Food and Agriculture (BMEL) based on a decision of the parliament of the Federal Republic of Germany via the Federal Office for Agriculture and Food (BLE) under the strategy for digitalisation in agriculture FKZ 28DE104A18 - Farmerspace.

Availability of data and materials

Upon request.

Declarations

Ethics approval and consent to participate

Not applicable.

Consent for publication

Not applicable.

Competing interests

The authors declare that they have no competing interests.

Received: 27 June 2024 Accepted: 6 December 2024

References

1. Gomez RB. Hyperspectral imaging: a useful technology for transportation analysis. Optical Eng. 2002;41:2137–43.
2. Lu G, Fei B. Medical hyperspectral imaging: a review. J Biomed Optics. 2014;19:010901–010901.
3. Feng Y-Z, Sun D-W. Application of hyperspectral imaging in food safety inspection and control: a review. Critical Rev Food Sci Nutri. 2012;52:1039–58.
4. Banerjee BP, Raval S, Cullen P. Uav-hyperspectral imaging of spectrally complex environments. Int J Remote Sens. 2020;41:4136–59.
5. Kurz TH, Buckley SJ, Howell JA. Close-range hyperspectral imaging for geological field studies: Workflow and methods. Int J Remote Sens. 2013;34:1798–822.
6. Mahlein A-K, Kuska MT, Behmann J, Polder G, Walter A. Hyperspectral sensors and imaging technologies in phytopathology: state of the art. Annual Rev Phytopatho. 2018;56:535–58.
7. Elmasry G, Kamruzzaman M, Sun D-W, Allen P. Principles and applications of hyperspectral imaging in quality evaluation of AGRO-food products: a review. Critical Rev Food Sci Nut. 2012;52:999–1023.
8. Paulus S, Mahlein A-K. Technical workflows for hyperspectral plant image assessment and processing on the greenhouse and laboratory scale. *GigaScience* 2020;**9**, giaa090.
9. Sousa JJ, et al. Uav-based hyperspectral monitoring using push-broom and snapshot sensors: A multisite assessment for precision viticulture applications. Sensors. 2022;22:6574.

10. Behmann J, et al. Specim iq: evaluation of a new, miniaturized handheld hyperspectral camera and its application for plant phenotyping and disease detection. Sensors. 2018;18:441.
11. Mahlein A-K, Steiner U, Hillnhütter C, Dehne H-W, Oerke E-C. Hyperspectral imaging for small-scale analysis of symptoms caused by different sugar beet diseases. Plant Methods. 2012;8:1–13.
12. Behmann J, et al. Calibration of hyperspectral close-range pushbroom cameras for plant phenotyping. ISPRS J Photogram Remote Sens. 2015;106:172–82.
13. Habib A, Xiong W, He F, Yang HL, Crawford M. Improving orthorectification of uav-based push-broom scanner imagery using derived orthophotos from frame cameras. IEEE J Select Topics Appl Earth Observa Remote Sensing. 2016;10:262–76.
14. Rehman TU, Ma D, Wang L, Zhang L, Jin J. Predictive spectral analysis using an end-to-end deep model from hyperspectral images for high-throughput plant phenotyping. Comput Elect Agricult. 2020;177: 105713.
15. Furbank RT, Tester M. Phenomics-technologies to relieve the phenotyping bottleneck. Trends Plant Sci. 2011;16:635–44.
16. Busemeyer L, et al. Breedvision - a multi-sensor platform for non-destructive field-based phenotyping in plant breeding. Sensors. 2013;13:2830–47.
17. Walter A, Liebisch F, Hund A. Plant phenotyping: from bean weighing to image analysis. Plant Methods. 2015;11:1–11.
18. Thomas S, et al. Benefits of hyperspectral imaging for plant disease detection and plant protection: a technical perspective. J Plant Dis Protect. 2018;125:5–20.
19. Migdall S, Bach H, Bobert J, Wehrhan M, Mauser W. Inversion of a canopy reflectance model using hyperspectral imagery for monitoring wheat growth and estimating yield. Precision Agricult. 2009;10:508–24.
20. Agrahari RK, Kobayashi Y, Tanaka TST, Panda SK, Koyama H. Smart fertilizer management: the progress of imaging technologies and possible implementation of plant biomarkers in agriculture. Soil Sci Plant Nut. 2021;67:248–58.
21. Leucker M, Mahlein A-K, Steiner U, Oerke E-C. Improvement of lesion phenotyping in Cercospora Beticola-sugar beet interaction by hyperspectral imaging. Phytopathology. 2016;106:177–84.
22. Kuska MT, Behmann J, Großkinsky DK, Roitsch T, Mahlein A-K. Screening of barley resistance against powdery mildew by simultaneous high-throughput enzyme activity signature profiling and multispectral imaging. Front Plant Sci. 2018;9:1074.
23. Brugger A, et al. Hyperspectral imaging in the uv range allows for differentiation of sugar beet diseases based on changes in secondary plant metabolites. Phytopathology. 2023;113:44–54.
24. Lawrence KC, Park B, Heitschmidt G, Windham WR. *LED lighting for use in multispectral and hyperspectral imaging* 2005.
25. Mahlein A-K, et al. Supplemental blue led lighting array to improve the signal quality in hyperspectral imaging of plants. Sensors. 2015;15:12834–40.
26. Mo C, et al. Non-destructive quality evaluation of pepper (*Capsicum annuum L.*) seeds using led-induced hyperspectral reflectance imaging. Sensors. 2014;14:7489–504.
27. Schaepman ME, Koetz B, Schaepman-Strub G, Itten KI. Spectrodirectional remote sensing for the improved estimation of biophysical and chemical variables: two case studies. Int J Appl Earth Observa Geoinform. 2005;6:271–82.
28. Parulski K, Wueller D, Burns P, Yoshida H. Creation and evolution of iso 12233, the international standard for measuring digital camera resolution. Elect Imag. 2022;34:1–7.
29. Salehi M, Proakis JG. *Communication Systems Engineering* (Prentice Hall, 2002).
30. Liu J, et al. Deep convolutional neural networks for Raman spectrum recognition: a unified solution. Analyst. 2017;142:4067–74.
31. Li S, et al. Deep learning for hyperspectral image classification: An overview. IEEE Trans Geosci Remote Sens. 2019;57:6690–709.
32. Meier U. Bbch *monografie*: Entwicklungsstadien mono- und dikotyler pflanzen 2001. https://www.openagrar.de/receive/openagrar_mods_00036305.
33. ISO. *ISO 12233:2023(en) Photography - Electronic still picture imaging - Resolution and spatial frequency responses* 2023.
34. Wolf P, Verreet J. An integrated pest management system in germany for the control of fungal leaf diseases in sugar beet: The ipm sugar beet model. Plant Dis. 2002;86:336–44.
35. R Core Team. *R: A Language and Environment for Statistical Computing*. R Foundation for Statistical Computing 2022. https://www.R-project.org/.
36. Lehnert LW, *et al. Hyperspectral data analysis in R: The hsdar package* 2018. https://cran.r-project.org/web/packages/hsdar/index.html.
37. Simon Urbanek. *Read and write PNG images* 2022. http://www.rforge.net/png/.
38. Loebich C, Wueller D, Klingen B, Jaeger A. *Digital camera resolution measurements using sinusoidal Siemens stars* 2007;6502 .
39. Roudier P, Lalibert E. *asdreader: Reading ASD Binary Files in R* 2017. http://github.com/pierreroudier/asdreader.
40. Wickham H. ggplot2: Elegant Graphics for Data Analysis. New York: Springer-Verlag, New York; 2016.
41. Rondeaux G, Steven M, Baret F. Optimization of soil-adjusted vegetation indices. Remote Sens Environ. 1996;55:95–107.
42. Richardson AJ, Wiegand C, et al. Distinguishing vegetation from soil background information. Photogrammetric Eng Remote Sens. 1977;43:1541–52.
43. Barreto A, Paulus S, Varrelmann M, Mahlein A-K. Hyperspectral imaging of symptoms induced by Rhizoctonia solani in sugar beet: Comparison of input data and different machine learning algorithms. J Plant Dis Protect. 2020;127:441–51.
44. Clayden J, Clayden MJ, Rcpp L. *Package 'mmand'* 2023. https://cran.r-project.org/web/packages/mmand/index.html.
45. Savitzky A, Golay MJ. Smoothing and differentiation of data by simplified least squares procedures. Analyt Chem. 1964;36:1627–39.
46. Van Boxtel, et al. *gsignal: Signal processing* 2021. https://github.com/gjmvanboxtel/gsignal.
47. Hu Y, Murray W, Shan Y. *R Parallel Implementation of Local Outlier Factor(LOF)* 2022. https://CRAN.R-project.org/package=Rlof.
48. Derek Kakness. *Semi Supervised Learning with DCGAN on Raman Spectra Data* 2023. https://github.com/DerekKaknes/raman.
49. Kalinowski T, *et al. R Interface to 'Keras'* 2023. https://tensorflow.rstudio.com/.
50. Nutter F, Teng P, Shokes F. Disease assessment terms and concepts. Plant Dis. 1991;75:31187–8.
51. Dixon WJ. Analysis of extreme values. Ann Mathe Statist. 1950;21:488–506.
52. Komsta L. *Tests for Outliers* 2022. https://www.R-project.org,http://www.komsta.net/.
53. Wilcoxon F, Katti S, Wilcox RA, et al. Critical values and probability levels for the wilcoxon rank sum test and the wilcoxon signed rank test. Selected Tables Mathe Statist. 1970;1:171–259.
54. Komsta L. *Conditional Inference Procedures in a Permutation Test Framework* 2023. http://coin.r-forge.r-project.org.
55. Leachtenauer JC, Driggers RG. *Surveillance and reconnaissance imaging systems: modeling and performance prediction* 2001.
56. Millette PA. The Heisenberg uncertainty principle and the Nyquist-Shannon sampling theorem. Progress Phys. 2013;9:9–14.
57. Wang F, Chen J, Xie Z, Ai Y, Zhang W. Local sharpness failure detection of camera module lens based on image blur assessment. Appl Intell. 2023;53:11241–50.
58. Cappellari M, Copin Y. Adaptive spatial binning of integral-field spectroscopic data using voronoi tessellations. Monthly Noti Royal Astronomi Soci. 2003;342:345–54.
59. Geladi P, Burger J, Lestander T. Hyperspectral imaging: calibration problems and solutions. Chemom Intell Lab Syst. 2004;72:209–17.
60. Mishra P, Lohumi S, Khan HA, Nordon A. Close-range hyperspectral imaging of whole plants for digital phenotyping: Recent applications and illumination correction approaches. Comput Elect Agricult. 2020;178: 105780.
61. Asaari MSM, et al. Close-range hyperspectral image analysis for the early detection of stress responses in individual plants in a high-throughput phenotyping platform. ISPRS J Photogram Remote Sens. 2018;138:121–38.

62. Liu H, Lee S-H, Chahl JS. Transformation of a high-dimensional color space for material classification. JOSA A. 2017;34:523–32.
63. Yang L *et al.* Depth anything: Unleashing the power of large-scale unlabeled data. arXiv preprint arXiv:2401.10891 2024.
64. Liu H, Bruning B, Garnett T, Berger B. Hyperspectral imaging and 3d technologies for plant phenotyping: From satellite to close-range sensing. Comput Elect Agricult. 2020;175: 105621.
65. Islam K, Ploschner M, Goldys EM. Multi-led light source for hyperspectral imaging. Optics Express. 2017;25:32659–68.
66. Bock CH, Chiang K-S, Del Ponte EM. Plant disease severity estimated visually: a century of research, best practices, and opportunities for improving methods and practices to maximize accuracy. Trop Plant Pathol. 2022;47:25–42.
67. He K, Gkioxari G, Dollár P, Girshick R. *Mask r-cnn* 2017.
68. Ronneberger O, Fischer P. & Brox, T. U-net: Convolutional networks for biomedical image segmentation; 2015.

Publisher's Note

CHAPTER 4: Phenotyping of syndrome “Basses Richesses” in sugar beet by morphological and spectral traits – Publication II

Accepted manuscript and published online in Phytopathology (2025), https://doi.org/10.1094/PHYTO-07-25-0239-R.

Justus Detring[1*], Jonas Bömer[1], Ayan Gupta[1,2], Omid Eini[1], Anne-Katrin Mahlein[1]

[1]Institute of Sugar Beet Research, 37079 Göttingen, Germany

[2]Institute of Computer Science, 37077 Göttingen, Germany

[*]Corresponding author: Detring@ifz-goettingen.de

Keywords: Syndrome “Basses Richesses”, phenotyping, 3D-scanning, hyperspectral imaging, machine learning, computer vision, plant spectroscopy, sugar beet, Boruta-SHAP, U-Net, Random Forest, disease monitoring, CNN

Author contributions: Conceptualization: JD, JB, AKM. Methodology: JD, JB, AG, OE. Investigation: JD, JB. Visualization: JD, JB. Funding Acquisition: AKM. Project Administration: AKM. Supervision: AKM. Writing Original Draft: JD, JB. Writing Review & Editing: JD, JB, AKM.

Phytopathology® • 2026 • 116:310-319 • https://doi.org/10.1094/PHYTO-07-25-0239-R

Molecular and Physiological Plant Pathology

Phenotyping of Syndrome "Basses Richesses" in Sugar Beet by Morphological and Spectral Traits

Justus Detring,[1,†] Jonas Bömer,[1] Ayan Gupta,[1,2] Omid Eini,[1] and Anne-Katrin Mahlein[1]

[1] Institute of Sugar Beet Research, 37079 Göttingen, Germany
[2] Institute of Computer Science, 37077 Göttingen, Germany
Accepted for publication 22 September 2025.

Abstract

Syndrome "Basses Richesses" (SBR) is a rapidly emerging sugar beet disease in central Europe that has a severe economic impact on the sugar beet industry and thus requires control. The cultivation of tolerant varieties is a promising method to reduce SBR. Digital plant phenotyping can support the screening process for tolerant varieties by characterizing traits of interest and quantifying tolerance. This research provides foundational work for digitally phenotyping SBR. Morphological and spectral traits were analyzed with machine learning, supporting disease monitoring and screening for tolerant varieties under controlled conditions. A susceptible sugar beet variety was infected with the dominant causal agent of SBR, '*Candidatus* Arsenophonus phytopathogenicus' (ARSEPH). Hyperspectral images of the canopy were recorded weekly between 20 and 62 days after inoculation and segmented by leaves and petioles. Sixty-seven days after inoculation, each leaf was two-dimensionally (2D) and each taproot three-dimensionally (3D) imaged by angle-corrected 2D imaging and structured-light 3D scans, respectively. The results indicated substantial decreases in leaf area (19.7%), leaf length (6.9%), leaf blade length (13.1%), and leaf blade width (12.1%) resulting from ARSEPH infection. The most important wavelengths for machine learning classification of ARSEPH-infected sugar beet were from the petioles (97% accuracy) in the range 623 to 659 nm and 421 to 432 nm. The 22 most relevant taproot 3D parameters were evaluated with Boruta-SHAP based on their importance to characterize SBR-induced taproot deformation. Certain value and spatial regions were characteristic, indicating thresholds for 3D parameters and taproot regions to analyze when comparing varieties.

Keywords: 3D scanning, Boruta-SHAP, CNN, computer vision, disease monitoring, hyperspectral imaging, machine learning, plant spectroscopy, random forest, U-Net

Syndrome "Basses Richesses" (SBR) has become a substantial threat to sugar beet production in central Europe. The first occurrence was reported 1991 in eastern France (Gatineau et al. 2002). Since then, SBR has spread to Germany, Switzerland, Hungary, and Austria (EPPO 2012). SBR is caused by two bacterial pathogens: '*Candidatus* Arsenophonus phytopathogenicus' (ARSEPH) and '*Candidatus* Phytoplasma solani' (PHYPSO), both of which are transmitted to sugar beet primarily by the planthopper *Pentastiridius leporinus* (Gatineau et al. 2002). Neither pathogen has been cultured axenically. Using infective adult *P. leporinus* is the sole method to artificially inoculate sugar beet plants. ARSEPH can be transmitted through *P. leporinus* generations horizontally and vertically. PHYPSO is not transmitted to the offspring of *P. leporinus*, which results in loss of PHYPSO in *P. leporinus* colonies when artificially reared (Bressan 2014; Pfitzer et al. 2022). ARSEPH, the dominant causal agent of SBR, belongs to a genus of symbiotic insect-associated bacteria (Bressan et al. 2012; Nováková et al. 2009). The present SBR control measures prioritize management of the primary vector *P. leporinus* through agronomic interventions such as crop rotation or tillage (Bressan 2014; Pfitzer et al. 2024). However, the high mobility and polyphagia of *P. leporinus* hinders the efficacy of these measures. Consequently, the cultivation of varieties demonstrating tolerance to ARSEPH emerges as a pivotal strategy for SBR management. Additionally, tolerant sugar beet varieties that can suppress the infection of the endosymbiont ARSEPH have the potential to interfere with the synthesis of sugar and amino acids for *P. leporinus* by ARSEPH, thereby contributing to the containment of the population in sugar beet (Bressan et al. 2012; Gonella et al. 2019). The first visible symptoms of SBR in sugar beet are yellowing of the older leaves and new small, narrow shoots with a chlorotic lamina, which is asymmetrical and has a curved appearance (Gatineau et al. 2001). The taproot develops a brownish discoloration of the vascular tissue, which can be seen when the taproot is cut into cross-sections (Gatineau et al. 2002). Precise methods for determining the tolerance of a variety against SBR by assessing the canopy or the taproot have not been developed.

Precise phenotypic information is needed to enable screening via remote sensing for potential resistance sources and for the subsequent development of tolerant or resistant varieties against SBR. Novel phenotyping methods such as hyperspectral imaging (HSI) offer the possibility of providing high-quality data in spatial and spectral dimensions (Detring et al. 2024; Mahlein 2016). Red, green, and blue (RGB) images provide useful spatial information, such as canopy morphology, but lack the spectral resolution to detect physiological or biochemical traits captured beyond the visible spectrum. Several studies have shown that RGB spectral regions are informative for plant phenotyping, especially

---

[†]Corresponding author: J. Detring; Detring@ifz-goettingen.de

Author contributions: J.D., J.B., and A.K.M. conceptualized the study. J.D., J.B., A.G., and O.E. developed the methodology. J.D. and J.B. conducted the investigation and performed the visualization. A.K.M. acquired the funding, administered the project, and supervised the study. J.D. and J.B. wrote the original draft of the manuscript. J.D., J.B., and A.K.M. reviewed and edited the manuscript.

Funding: This work has been funded by the Deutsche Forschungsgemeinschaft (DFG, German Research Foundation) under Germany's Excellence Strategy–EXC 2070–390732324, and the Federal Ministry of Food and Agriculture (BMEL) based on a decision of the Parliament of the Federal Republic of Germany. The Federal Office for Agriculture and Food (BLE) provided coordinating support for artificial intelligence (AI) in agriculture as a funding organization (grant number 28DK108C20).

e-Xtra: Supplementary material is available online.

The author(s) declare no conflict of interest.

to determine pathogen-induced alteration to the plant canopy (Barreto et al. 2023a; Ispizua Yamati et al. 2024; Mahlein et al. 2018). Recent research in spectral imaging has focused primarily on fungal pathogens, which manifest distinct symptoms that can be readily mapped in the spatial dimension (Barreto et al. 2020; Bohnenkamp et al. 2021; Kuska et al. 2017; Mahlein et al. 2012). Systemic diseases caused by viruses or bacteria, which are often vector transmitted, such as SBR, are more difficult to spatially and spectrally characterize with HSI (Cubero et al. 2024; Okole et al. 2023). Also, most hyperspectral plant phenotyping approaches do not differentiate between canopy organs, such as leaves and petioles, despite the significant physiological differences between them and assume general differences in the spectral response of these plant organs (Geiger et al. 1969).

Besides two-dimensional (2D) imaging-based measuring methods, three-dimensional (3D) scanning has been widely introduced for plant phenotyping (Paulus et al. 2013, 2014b). Depending on the precision needed, 3D models can be generated using various measurement techniques (Paulus 2019). The methods result in generation of a 3D point cloud or mesh. One of the most common 3D scanning techniques for smaller objects is structured light scanning (Paulus et al. 2014a). A structured light scanner projects a pattern of light (e.g., stripes or grids) with known dimensions onto the target. By the deformation of the known patterns, the 3D model can be calculated (Winkelbach et al. 2006). Acquiring such 3D models of plants enables digital and highly precise quantification of morphological differences between varieties and morphological changes caused by environmental stress (Akhtar et al. 2024). Vascular plant pathogens such as ARSEPH can have profound effects on the health and growth of plant sink organs. The taproot of sugar beet is considered the sink organ and the most important organ with regard to yield and therefore economic return. The utilization of 3D parameters derived from acquired 3D models of ARSEPH-infected sugar beet taproots has the potential to facilitate measurement of the characteristics and severity of the disease effects on growth.

How SBR affects the spectral reflectance properties and morphology of the leaves or the taproot has yet to be determined, although some reports indicate change. Agyei et al. (2025) described significant taproot volume and cambium ring width reduction caused by SBR using magnetic resonance imaging but stated that further phenotypic description and a better understanding of morphological change was needed to characterize the effect of the pathogen.

Thus, our research objective was to develop an integrated digital SBR phenotyping approach of ARSEPH-infected sugar beet canopies and taproots (Fig. 1) using machine learning methods for extracting crucial features associated with the disease.

Materials and Methods

Plant material and molecular diagnostics

To investigate the phenological alteration caused by SBR, ARSEPH-infected sugar beet plant material was prepared. Pre-infection trials showed that the sugar beet variety BTS 8750 (Betaseed GmbH, Frankfurt, Germany) was susceptible to ARSEPH. Therefore, seeds of BTS 8750 were sown at a depth of 1 cm in polypropylene pots filled with Fruhstorfer soil type P 25 (HAWITA Gruppe GmbH, Vechta, Germany). After a germination period of 7 days, 30 BTS 8750 seedlings were transferred individually into 1-liter round polypropylene pots filled with fertilized sandy topsoil (Gustav Lehmann Mörtel- u.; Kieswerke GmbH, Burgdorf, Germany). The sugar beet plants were cultivated in the greenhouse for 11 days (14:10-h light/dark photoperiod, 25.0 ± 5.7°C, 49.0 ± 15.7% relative humidity, and approximately 225 μmol/[sm] full-spectrum light) until growth stage BBCH 12 (Meier et al. 2009). The sugar beet plants were placed in six insect-rearing tents (Mega View Science Co., Taichung, Taiwan), each having dimensions of 60 × 60 × 60 cm (length × width × height) and a mesh size of 150 × 150 (160-μm aperture). Five sugar beet plants were placed in each insect-rearing tent. The tents were transferred into a climate chamber (16:8 h light/dark photoperiod, 23.0 ± 5.3°C, 52.1 ± 6.6% relative humidity and approximately 250 μmol/[sm] full spectrum light), and 25 *P. leporinus* adults were added to each of three tents using an insect exhauster (Ø 35 mm; Ehlert and Partner GbR, Niederkassel-Rheidt, Germany). The three remaining tents were maintained as a noninoculated comparison check, resulting in 15 replicates of each variant. The *P. leporinus* adults for inoculation were obtained by rearing them in the laboratory as described by Pfitzer et al. (2022). The inoculation period with the *P. leporinus* adults lasted for the subsequent 11 days. After inoculation, the *P. leporinus* adults were removed from the tents, and all sugar beet plants were sprayed with insecticide (0.35% Confidor WG 70; Bayer Crop Science AG, Monheim, Germany). After insecticide treatment, the sugar beets were removed from the tents and transferred to the greenhouse for 56 days until harvest (14:10-h light/dark photoperiod, 26.3 ± 5.9°C, 58.2 ± 19.4% relative humidity, and approximately 225 μmol/[sm] full-spectrum light). The sugar beet plants were watered daily and fertilized every 3 weeks with 50 ml of a 1:40 liquid fertilizer (liquid universal fertilizer: 4% nitrogen, 2% phosphorus pentoxide, 2% potassium oxide) mixed with tap water. The sugar beet plants were harvested 67 days after inoculation (dai). The pathogenesis of SBR is presented in Figure 2.

During harvest, taproot tissue samples were collected from all inoculated and nine noninoculated plants for molecular detection

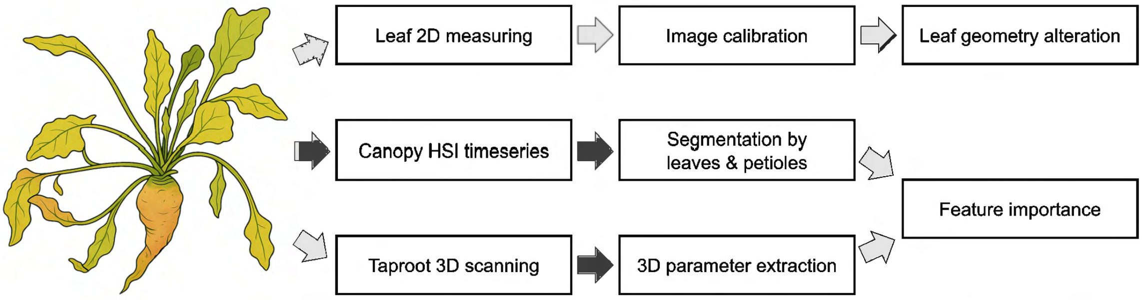

Fig. 1. Digital phenotyping of sugar beet with symptoms of syndrome “Basses Richesses” (SBR) caused by ‘*Candidatus* Arsenophonus phytopathogenicus’ (ARSEPH). The digital phenotyping approach includes four major steps (from left to right): the experimental phase, data acquisition, data processing, and results. The experimental phase consists of inoculating sugar beet plants with ARSEPH-infected *Pentastiridius leporinus* adults under controlled conditions. The methods used for digital phenotyping data acquisition were weekly noninvasive hyperspectral imaging (HSI) of the canopy between 20 and 62 days after inoculation (dai), invasive 2D image-based measuring of single leaves at 67 dai, and invasive 3D scanning of the taproot at 67 dai. To analyze the hyperspectral images, the canopy was separated into two components as leaves and petioles to differentiate the most important features for spectral characterization and classification between infected and noninfected sugar beet. The image angle of single leaves was calibrated to extract geometrical leaf parameters that describe the changes caused by SBR. The extracted 3D parameters were analyzed to find the most important for describing SBR-induced taproot deformation.

of ARSEPH. The tissue samples were collected from brownish discolored taproot tissue below the hypocotyl. Approximately 100 mg per taproot was collected in 1.5-ml Eppendorf tubes (Eppendorf SE, Hamburg, Germany), frozen in liquid nitrogen, and stored at −80°C. The frozen samples were ground in the tubes to obtain a powdery texture in preparation for deoxyribonucleic acid (DNA) extraction. The DNA extraction was conducted using a NucleoSpin Plant II Mini Kit for DNA for plants (MACHEREY-NAGEL GmbH & Co. KG, Düren, Germany). The purified DNA of each inoculated sample and the nine noninoculated samples was transferred into a well on a 96-well plate (Bio-Rad Laboratories GmbH, Feldkirchen, Germany). Two technical replicates were included. Additionally, two negative and positive control samples were added. Two replicates of a dilution series of the purified amplicon of the target gene, heat shock protein 20 (*hsp20*), were added to the plate. To detect *hsp20* of ARSEPH in the inoculated plants, TaqMan qPCR was used with previously described primers (Zübert and Kube 2021). The qPCR mixture contained 6.3 µl of distilled water, 10 µl of Maxima Probe qPCR Mix, 0.9 µl of each primer, 0.4 µl of probe (10 µM; Fam-BHQ1 labeled), and 1.5 µl of sample DNA. A CFX96 Real-Time System C1000 Touch Thermal Cycler (Bio-Rad Laboratories GmbH) was used for the qPCR with the following cycle conditions: 95°C for 3 min and 40 cycles at 95°C for 15 s and 60°C for 30 s. The qPCR results were processed in CFX Manager (version 3.1; Bio-Rad Laboratories GmbH). Samples are considered infected with ARSEPH if the cycle quantification (C_q) value is $\leq$36.00, which constitutes all inoculated sugar beet plants as infected with ARSEPH (Supplementary Table S1).

Canopy HSI

The measurements were conducted in a dark chamber made of aluminum with dimensions of 1.5 × 1.5 × 2 m (length × width × height). To prevent light interference in the chamber during the measurements, the walls were covered with polyurethane-coated black nylon fabric (Blackout Fabric; Torlabs, Newton, NJ). Plant heat stress was prevented by leaving the ceiling of the dark chamber uncovered. The sensor carrier platform installed (Supplementary Fig. S1A) in the dark chamber was modified as previously described by Mahlein et al. (2012) and Behmann et al. (2015).

The linear axis of the sensor carrier platform was mounted on the top of the dark chamber (BiSlide; Velmex, Bloomfield, NY). An aluminum cage with dimensions of 0.25 × 0.25 × 0.3 m (length × width × height) was also attached to the linear axis. Inside the cage, a line scanning hyperspectral camera (FX10; Specim Spectral Imaging Ltd., Oulu, Finland) was mounted with an operating computer (DAC & PCU Kestrel; Specim Spectral Imaging Ltd.). The hyperspectral camera had a spectral range of 400 to 1,000 nm and a spectral resolution of 5.5 nm. This resulted in 224 distinct spectral bands. The spatial resolution of the hyperspectral camera was 1,024 pixels. The external halogen illumination apparatus comprised six 70-watt voltage-stabilized quartz-tungsten halogen lamps (Illuminator Lamp; Malvern Instruments, Malvern, United Kingdom). To ensure an even distribution of illumination, diffusive screens were attached 2 cm from the lamps using metal wires. The screens were composed of nylon silk, which exhibited an approximate light reduction of 1.0 f-stop.

Three lamps were attached on each side of the sensor at an angle of about 45° to prevent light-mirroring effects between illumination and sensor. A matte black lacquered wooden panel was installed 74 cm below the objective of the hyperspectral camera. The center of the linear axis was marked on the wooden panel for the placement of the plant material. The hyperspectral camera and the linear axis were operated with the software Lumo Scanner (version 2023.631; Middleton Spectral Vision, Middleton, WI).

The focus of the hyperspectral camera was set to 49 cm (the distance to the middle of the plant material canopy) from the objective and calibrated with the application of Lumo Scanner. The scanning parameters were set to 1,710 lines, 37.5 fps, speed 14.5 mm/s, exposure time 25 ms, spatial binning 1, and spectral binning 2. The HSI began at 20 dai and was conducted weekly for 6 weeks. On each date, each plant was imaged three times by rotating the plant by 120°. Additionally, a barium sulfide plate (43 × 43 cm; Specim Spectral Imaging Ltd.) was scanned for white referencing prior to each scanning sample date.

To adjust the sensitivity of the sensor to the white reference plate and avoid oversaturation, the exposure of the white reference measurement was reduced to 5 ms. The dark reference measurements were done with the same exposure as the plant material to capture the sensor noise and conducted by closing the shutter of the hyperspectral camera.

Leaf 2D measuring

To investigate the effect of SBR on the morphological characteristics of sugar beet leaves, an invasive 2D measurement of individual leaves was carried out at harvest time (67 dai) using calibrated RGB images. A stationary imaging design was used comprising a standard digital single-lens reflex camera (Alpha 58; Sony Group Corporation, Tokyo, Japan) mounted on a tripod with a flat background board for placing the single leaves (Supplementary Fig. S1B). Prior to the acquisition of leaf images, a calibration checkerboard image (9 × 6 cm) was captured. The calibration image was subsequently utilized in the image processing procedure for leaf image rectification. Subsequently, each leaf of a sugar beet plant was separated from the beet body at its base and photographed. The leaves were positioned on the background board and flattened using a plexiglass board. A total of 209 leaf images of the noninfected and 220 images of the infected sugar beet plants were captured.

To ensure the accuracy and consistency of the parameter extraction process, the captured images of the individual leaves underwent rectification and transformation to an orthographic view. This procedure was essential for correcting perspective distortion due to image capture angle and camera intrinsics. Consequently, a homograph-based image rectification approach was employed using OpenCV (Bradski 2000) based on the calibration checkerboard image, which resulted in a calibrated top-down view of each leaf image. The known geometry of the checkerboard pattern was utilized to detect the corners of the pattern. Subsequently, a homograph matrix was

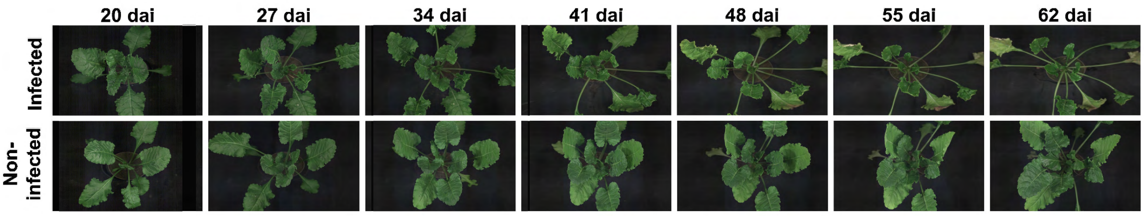

Fig. 2. Pathogenesis of syndrome "Basses Richesses" after inoculation (top row) of sugar beet with '*Candidatus* Arsenophonus phytopathogenicus'-infected *Pentastiridius leporinus* adults compared with noninoculated (bottom row) sugar beet at 20, 27, 34, 41, 48, 55, and 62 days after inoculation (dai; from left to right).

computed to map the detected pattern to an orthographic view. The same matrix was then applied to the leaf image, effectively warping it so that it appeared to be captured from a nadir perspective. Subsequently, a masked version of the transformed leaf image was generated using scikit-image (Van Der Walt et al. 2014), excluding the background and preparing the image for parameter extraction.

Taproot 3D scanning

At harvest, the taproots of all cultivated sugar beet plants were measured in 3D to analyze possible cross-sectional deformation of the beet body induced by SBR. A structured light 3D scanner (HP Pro S3; HP, Pato Alto, CA) including two monochromatic cameras was employed to generate the 3D models of the taproots (Supplementary Fig. S1C). The scanner can measure objects 30 to 500 mm in size with a resolution of up to 0.05 mm. Before scanning, the leaves were detached from the taproots, and the taproots were placed upside-down on a turntable. To generate occlusion-free 3D models, the taproots were scanned from eight viewpoints. The registration of the individual point clouds of each single taproot into a unified point cloud was achieved by leveraging the rotational information provided by the turntable and utilizing the iterative closest point algorithm for fine registration. The turntable itself and other scanning artifacts were subsequently removed from the model manually using the open-source software CloudCompare (version 2.13.2).

Leaf and petiole segmentation and determining primary spectral features for classification of ARSEPH-infected sugar beet

Analyses were performed in R (version 4.3.1; R Core Team, Vienna, Austria) and RStudio (version 2024.04.2+764; Posit Team 2025). Normalization and smoothing were applied as preprocessing steps to the hyperspectral data before canopy organ segmentation and spectral analysis using the package "hsdar" (version 1.0.4; Lehnert et al. 2018) for hyperspectral data management. Therefore, the white reference hyperspectral image was cropped to the size of the barium sulfide reference plate, and a vertical mean pixel line for each spectral band corresponding to the line length of the hyperspectral camera was calculated. The same was done for the dark reference data. The resulting reference pixel lines were used to normalize each pixel line from the acquired hyperspectral data with the following formula:

$$\text{Reflectance} = \frac{\text{hyperspectral image} - \text{dark reference hsi}}{\text{white reference} - \text{dark reference white}} \times \frac{\text{exposure white reference}}{\text{exposure hyperspectral image}}$$

After normalization, the first five spectral bands (400 to 409 nm) were excluded from further processing and analysis due to sensor-specific technical noise. The normalized hyperspectral data were smoothed by applying he Savitz–Golay smoothing filter (filter order = 3, filter length = 5) with the package "gsignal" (version 0.3.7; van Boxtel 2021) to reduce noise in the spectral data (Savitzky and Golay 1964).

RGB images were generated from the normalized and smoothed hyperspectral images using the package "png" (version 0.1-8; Urbanek 2022). The hyperspectral bands at 525, 550, and 600 nm were chosen for visualization. The three classes background, leaves, and petioles were defined by manual annotation of the RGB images. The images were annotated for training and validating a convolutional neural network for semantic segmentation of the three classes of each RGB image to create masks for further analysis of the hyperspectral data. Each pixel of 120 chosen RGB images was manually annotated to one of the three defined classes using the software GIMP (version 2.10.36; The GIMP Team). For annotating the training dataset, images of 10 leaves of sugar beet plant repetitions per date and variant were randomly chosen, whereas five leaf sugar beet plant repetitions and two dates of the time series were preserved for validating the performance of the convolutional neural network on segmentation of the three classes on unknown plants and time points. A pretrained U-Net model with a ResNet18 encoder backbone was chosen for the semantic segmentation (He et al. 2016; Ronneberger et al. 2015). The U-Net model has become a cornerstone in the field due to its effectiveness in learning from limited datasets and producing precise segmentation results. Although the original U-Net model was designed for binary segmentation; it was adapted for multiclass segmentation. Instead of applying an activation function, the model outputs raw logits for each class at every pixel location. A categorical cross-entropy loss function was employed that operates on raw logits and is suitable for multiclass segmentation tasks in which each pixel belongs to exactly one class. The established ResNet18 backboned U-Net achieved a segmentation performance (intersection over union) of 98% for the class "background," 95% for the class "leaves," and 67% for the class "petioles" (Supplementary Table S2). The performance of the class "petioles" was reduced due to the high number of edge pixels compared with the overall number of pixels in this class caused by the natural shape of this plant organ. Segmenting the edges of an object in the image is difficult because of the mixed spectral values. Furthermore, validating the performance of a class with a lot of edge pixels is biased because human annotation of edge pixels is challenging as well. Evaluating the generated masks from the U-Net (Supplementary Fig. S2) and the low standard deviation of the spectral signature indicates that the manual annotation might have caused the bias in the performance by spuriously annotating the edge pixels to the petiole class compared with the segmentation results.

The masks generated by the U-Net were used to calculate an average spectrum for the leaves and the petioles from each of the 630 hyperspectral images. Two random forest machine learning models (Breiman 2001) were trained using the package "randomForest" (version 4.7.1.2, number of trees: 500; Liaw and Wiener 2002) to classify ARSEPH-infected sugar beet plants based on hyperspectral information from leaves and petioles and to extract the most important wavelengths for classification. One model was trained with the hyperspectral data of the leaves and the other with the hyperspectral data of the petioles. The hyperspectral images of both the leaves and the petioles were annotated for visible SBR symptoms as a reference for training and validating the models. A sugar beet plant was labeled SBR symptomatic if new, small, narrow shoots with a chlorotic lamina and a curved appearance were observed (Gatineau et al. 2002). The training data comprised 12 plants from the ARSEPH-infected group and 12 plants from the noninfected group (a total of 552 hyperspectral images). The validation data contained the remaining three plants of each group (totaling 138 hyperspectral images), resulting in a data split of 80% for training and 20% for validating. During the training process, random forest ranks the given wavelengths for their importance for classifying between infected and noninfected sugar beet plants. The extracted importance of the leaf and the petiole model was normalized with the following formula:

$$\text{Normalized importance} = \frac{\text{importance} - \text{minimum importance}}{\text{maximum importance} - \text{minimum importance}}$$

2D image calibration and extraction of geometrical parameters

The processed images were subsequently utilized for the extraction of six morphological parameters by employing customized Python (Van Rossum and Drake 2009) algorithms. This included the total leaf length, the leaf blade length, the petiole length, the leaf blade width, the leaf area, and a leaf blade symmetry index.

The total leaf length was defined as the maximum distance from the petiole basis to the leaf blade tip. The calculation of the leaf blade length and the petiole length required the identification of the leaf blade basis, which corresponds to the transition point between the petiole and the leaf blade. Therefore, a 2D version of the definition proposed by Bömer et al. (2024) was implemented. The width of the leaf blade was measured perpendicular to the length axis of the leaf blade, thereby providing a quantitative description of the maximum distance between the leaf edges. The leaf area could be calculated by a simple pixel count, made possible by the previous homograph-based image rectification. The leaf blade symmetry index was similarly determined by manually marking the leaf vein and counting the pixels of the leaf blade on either side of the vein. The index was subsequently calculated by dividing the smaller side of the leaf blade by the bigger side, ensuring a maximum index of 1 (perfect symmetry). The smaller the index value, the higher the asymmetry of the leaf blade.

All extracted morphological leaf parameters were statistically analyzed to determine if there were significant differences between leaves of the noninfected and ARSEPH-infected sugar beet plants. This analysis was performed using SciPy (Virtanen et al. 2020) with a significance threshold of $\alpha = 0.05$. Initially, the data were assessed for normality using the Shapiro–Wilk test. Due to all parameters showing deviations from normality, nonparametric Mann–Whitney U tests were conducted.

3D parameter extraction and feature impact on Borut-SHAP

A processing pipeline for the 3D scans of the taproots was implemented in Python to automate the remaining processing steps for extracting cross-sections. The point clouds of the taproots were initially aligned along their length axis. Consequently, the root tip and the center of the beet body were identified, and the point clouds were rotated so that these two points lay on a line (z axis). Subsequently, for each taproot, 15% of its height was removed at the top and 25% at the root tip. This was performed to guarantee the reliability of the downstream parameter extraction algorithms, as these have difficulties handling small and thin objects. From the point cloud that was prepared in this manner, cross-sections in the xy-plane were cut into wafers of 1.0 mm. This resulted in 707 cross-sections of the noninfected and 665 cross-sections of the ARSEPH-infected sugar beet plants.

The initial step in the extraction of the morphological parameters of the cross-sections involved the projection of the cross-sections onto the xy plane, effectively eliminating the previous 1.0-mm-thick wafer and reducing them to a 2D plane. Subsequently, a polygon was fitted through the cross-sections' 2D point cloud in accordance with the method of Taubin (1991) This circle served as the foundation for the subsequent collection of all other cross-sectional morphological parameters. These parameters can be grouped into the four main categories of shape descriptors (roundness, skewness, axial measures), spatial descriptors (perimeter, area, convex hull), notch descriptors (area, quantity, depth), and ratio measures, which express proportions between the various extracted descriptors. All extracted parameters are listed and explained in detail (Supplementary Table S3).

To identify the most relevant morphological cross-sectional parameters associated with SBR, first, a correlation analysis was performed to remove redundant information. For each pair of parameters with a correlation $r > 0.95$, the more difficult to calculate parameter of the pair was removed from the dataset (Supplementary Fig. S3). Subsequently, a feature selection procedure was conducted (Supplementary Fig. S4) using the Boruta-SHAP algorithm (Keany 2022). The algorithm combines the robustness of the Boruta feature selection method (Kursa et al. 2010) with the interpretability of SHapley Additive exPlanations (SHAP) values (Lundberg and Lee 2017). The approach evaluates the importance of each parameter by comparing it against a randomized copy of the parameter, which serves as a baseline. SHAP values were derived from a random forest model and quantify each parameter's contribution to the prediction of the model.

All predictor variables were standardized prior to analysis using z-score normalization. The Boruta-SHAP algorithm was run in classification mode for 100 trials with a fixed random seed to ensure reproducibility. Features were accepted or rejected based on their statistical relevance across multiple iterations. To visualize and interpret the individual parameters' effects, SHAP summary plots were generated for all parameters.

Results

Spectral response from ARSEPH-infected sugar beet canopies and the most important spectral features for classification of infection

Canopy reflectance of ARSEPH-infected sugar beet plants exhibited an increasing change in the spectral response of leaves and petioles over time (Fig. 3). The reflectance of the leaves from the ARSEPH-infected sugar beet plants was continuously lower at all three infection stages (early infection, first visible symptoms, late infection) and showed differences with low standard deviations in the region 410 to 700 nm at all three time points.

A clear shift with a large standard deviation was visible at 41 dai in the region 700 to 1,000 nm, which was further increased at 62 dai. The most important wavelengths (>85% importance) for classifying ARSEPH-infected sugar beet by the spectral response of the leaves at any time point were all between 604 and 632 nm (Fig. 3A).

The reflectance of the petioles from the ARSEPH-infected sugar beet shifted from below the noninfected at 20 dai to above at 41 dai and decreased until late infection at 62 dai to a similar level compared with the noninfected group (Fig. 3B). The most divergent regions between two groups were at 20 and 62 dai between 410 and 460 nm. Whereas the average spectrum between 700 and 1,000 nm at 62 dai was similar between groups, the standard deviation was increased, especially for the ARSEPH-infected group. The most important wavelengths (>85% importance) for classifying ARSEPH-infected sugar beet by the spectral response of the petioles at any time point were between 623 and 659 nm and between 421 and 432 nm. Considering the distribution of importance across all bands (a total of 219 bands analyzed), 68 bands from the petiole model and 50 bands from the leaf model had a normalized importance >50%. Additionally, 147 bands from the petiole model and 159 bands from the leaf model had a normalized importance >25%.

Determination of ARSEPH-infected sugar beet is best classified based on petiole hyperspectral data, with an accuracy of 97%. In comparison, detection based on leaf hyperspectral data exhibited an accuracy of 60% (Table 1).

Moreover, the models for classification between ARSEPH-infected and noninfected sugar beet based on leaf and petiole hyperspectral data showed excellent performance in classifying noninfected sugar beet, with both scoring >90% accuracy.

Geometrical leaf parameters of ARSEPH-infected and noninfected sugar beet

The leaves of ARSEPH-infected sugar beet plants exhibited significant reductions in leaf area (19.7%), leaf length (6.9%), leaf blade length (13.1%), and leaf blade width (12.1%), respectively (Fig. 4A to D). There was no significant difference in petiole length (Fig. 4E) or in symmetry (Fig. 4F) between ARSEPH-infected and noninfected sugar beet leaves.

The interquartile range of leaves of ARSEPH-infected sugar beet plants was broader for all six leaf geometric parameters compared with the noninfected group, indicating greater variability in the data. The leaves of noninfected sugar beet plants with narrower interquartile ranges and less variability showed outliers in all parameters except leaf area. With the exception of the symmetry index, there were no outliers for any leaf parameters of ARSEPH-infected sugar beet plants. The leaves of ARSEPH-infected sugar beet plants presented a reduction in the median of all geometrical leaf parameters except for petiole length, with a statistical significance in four of the parameters, which suggests a major influence of ARSEPH on the leaf geometry of sugar beet.

3D parameters for describing SBR-induced taproot deformation

The assessment of feature importance was executed through the utilization of the Boruta-SHAP method, which integrates the Boruta algorithm for the selection of robust features with SHAP values to enhance the interpretability of the model. The resulting SHAP bee swarm plot illustrates the relative importance and influence of the 22 selected 3D parameters on the model's predictions of ARSEPH infection of a given taproot slice (Fig. 5A). The SHAP bee swarm plot is a visual representation of the impact of feature values on the model's output. For instance, elevated values of the "Biggest notch vs. biggest notch perimeter" were associated with substantial negative SHAP values, indicating that increasing the "Biggest notch vs. biggest notch perimeter" consistently led to a reduction of the model's performance. Therefore, low values of "Biggest notch height vs. biggest notch perimeter" had a greater impact on the model than high values. However, for "Roundness fitted biggest circle," the high values had a higher impact than the low values. Even though the mean absolute SHAP value of "Biggest notch area vs. notches area" was lower than "Biggest notch height vs. biggest notch perimeter," high values of "Biggest notch area vs. notches area" had the greatest impact on the model; low values of "Polygon perimeter vs. axis minor" also had a major impact on the model.

If the spatial dimension is considered, the upper part of the taproot SHAP values for "Roundness fitted biggest circle" had a greater impact on the model compared with the lower part (Fig. 5B). The lower part of the taproot was important due to its impact on the model when "skewness" was considered. Whereas no distinct region of "Biggest notch area vs. polygon area" could be identified with a high importance. "Biggest notch height vs. biggest notch perimeter" was ranked the most important 3D feature with an absolute mean SHAP of 0.04. The scattering of the mean SHAP values of all features is small. The 10 most important features presented a mean SHAP between 0.04 and 0.02. The mean SHAP of the remaining features ranged between 0.02 and 0.01.

Discussion

ARSEPH-induced SBR in sugar beet has severe effects on the plant, causing chlorosis, necrosis, and deformation of leaves and brownish discoloration of the taproot vascular tissue (Gatineau et al. 2002). This research supports and extends previous descriptions of SBR symptoms with digital phenotyping technologies under controlled laboratory conditions. Furthermore, effects of ARSEPH infection were quantified, such as overall leaf area, length, blade

TABLE 1. Random forest classification performance (accuracy, precision, and recall) of '*Candidatus* Arsenophonus phytopathogenicus'-infected and noninfected sugar beet canopies separated between leaf or petiole spectral response

Organ	Group	Accuracy	Precision	Recall
Leaf	Noninfected	0.90	0.88	0.90
	Infected	0.60	0.64	0.60
Petiole	Noninfected	0.91	0.99	0.91
	Infected	0.97	0.76	0.97

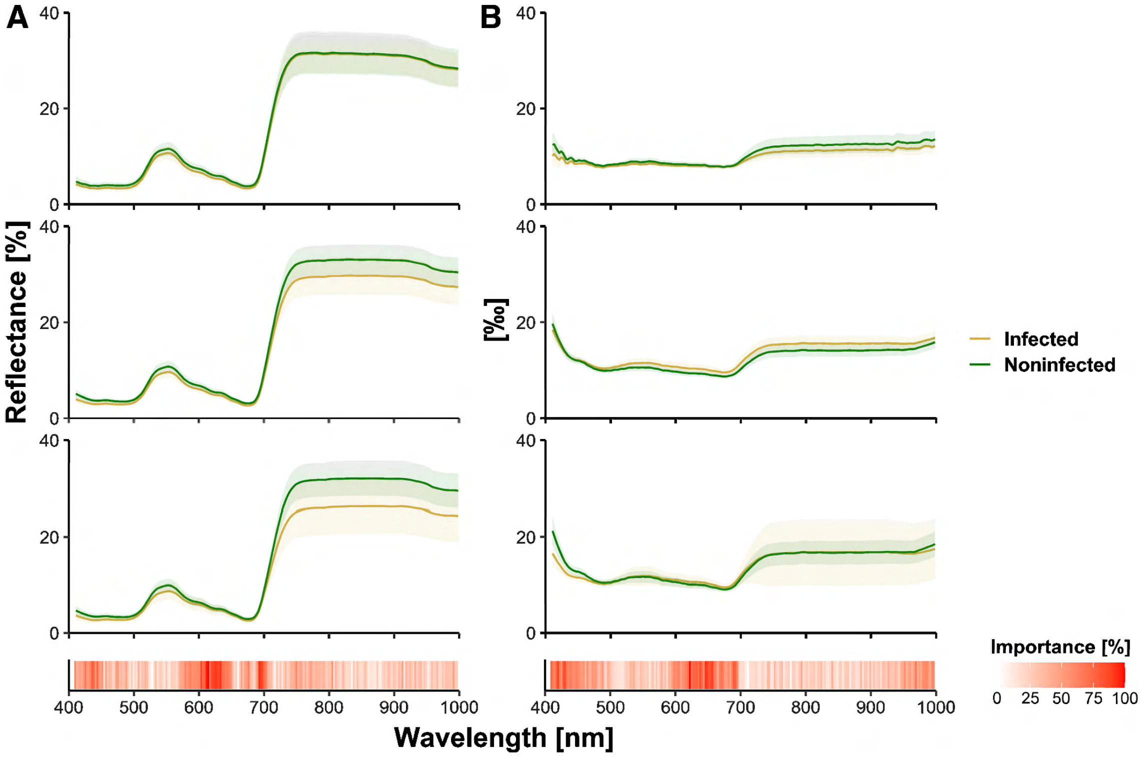

Fig. 3. Mean reflectance ± standard deviations ($n = 45$) of sugar beet canopies at 20 (early infection), 41 (first visible symptoms), and 62 (late infection) days after inoculation (from upper to lower panel) with '*Candidatus* Arsenophonus phytopathogenicus' (ARSEPH) via *Pentastiridius leporinus* adults. The canopy was separated between **A,** leaf and **B,** petiole for random forest classification and feature importance of ARSEPH-infected and noninfected sugar beet.

length, and blade width, which are significantly reduced (Fig. 4A to D) by infection, which had not been previously described. Furthermore, the results showed that there was no effect of ARSEPH infection on leaf symmetry, which had previously been suggested (Gatineau et al. 2001), although we did not categorize leaves by their age for the analysis. Leaf morphology effects of ARSEPH may develop differently depending on leaf age, an area for investigation in future research.

As a phloem-limited systemic disease (Gatineau et al. 2002), the reduced leaf area, leaf length, leaf blade length, and leaf blade width may be due to a systemic plant defense reaction. The long, rod-shaped, and often filamentous ARSEPH bacterial cells are not capable of moving through the sugar beet itself and therefore move with the plant's phloem stream (Bressan et al. 2012). After ARSEPH transmission from the vector to the sugar beet leaves, which thus function as source organs, the bacteria are transported through the petioles into the taproot, the sugar beet sink organ (Fellows and Geiger 1974). Effects of ARSEPH on the taproot are visible when cross-sections are taken: there is brownish discoloration, which is assumed to be a lignification of the cell walls (Gatineau et al. 2002). Possibly, the lignification prevents further spread of the pathogen. It may be that the damage to the vascular system and consequent disruption to the nutrient balance caused by the blockage in transport between the leaves and the taproot is responsible for the canopy symptoms, including the reduction in leaf area, leaf length, leaf blade length, and leaf blade width.

Mahillon et al. (2022) did not find ARSEPH in the blades of the older leaves but detected high titers in their petioles, which may be caused by a plant reaction to stop the spread of ARSEPH already in the petioles. Additionally, the vascular system in petioles is denser and can function as a sink organ for translocation (Geiger et al. 1969). This suggests a greater influence of the petioles on the spectral response compared with the leaves, caused by physiological changes due to the plant response. To analyze the influence of SBR on the spectral response of either leaves or petioles, the well-established random forest regression model was used to interpret the spectral data (Breiman 2001). The alteration to the spectral response of sugar beet petioles caused by ARSEPH infection could be detected with an accuracy of 97% at any time point during pathogenesis, compared with the effects of ARSEPH on the sugar beet leaves, which resulted in an accuracy of detection of only 60% (Table 1). The change in spectral response of the leaves was strongest in the NIR region (700 to 1,000 nm) which progresses over time (Fig. 3A). The change manifests as a complete shift of the whole spectrum, which is a common phenomenon for plant stress caused by changes in the cell structure in the mesophyll and not unique to SBR (Sun et al. 2021; Xu and Ye 2023). Linear shifts of the spectral response in any region have high correlations between the curves for both infected and noninfected groups that lack distinct features to be picked up by the machine learning algorithm for classification. The most important bands for classification between ARSEPH-infected and noninfected sugar beets were 623 to 659 nm and 421 to 432 nm, which are known to be the spectral regions for chlorophyll light absorption (Zscheile et al. 1942). Changes in these spectral regions might indicate a change in chlorophyll activity and content, which is predominantly the cause of leave chlorosis. If the average spectral response is considered (Fig. 3), the change between 623 to 659 nm and 421 to 432 nm is greater for the petioles, with a greater standard deviation in these regions, which could explain the diverging classification accuracy of 37% between models. Overall, the variance in the waveband importance for both models is relatively small; more than 50 bands have half the importance, and more

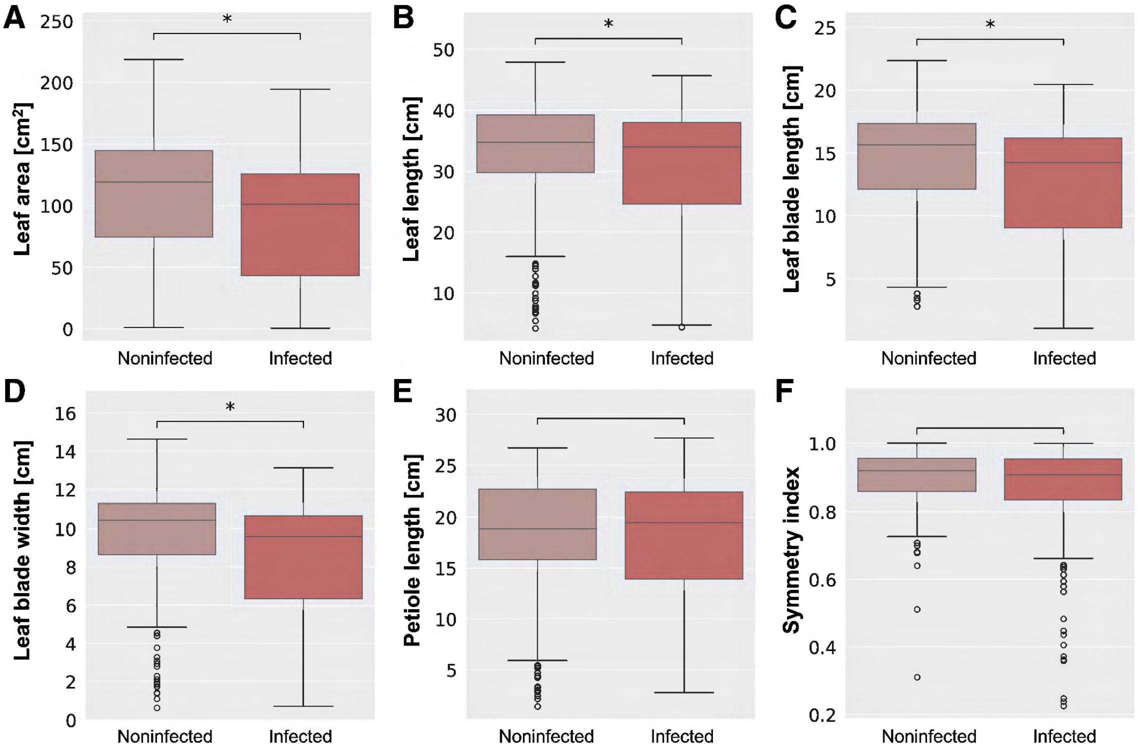

Fig. 4. Comparison of the leaf parameters **A,** area; **B,** length; **C,** blade length; and **D,** blade width, as well as **E,** petiole length and **F,** symmetry index between '*Candidatus* Arsenophonus phytopathogenicus'-infected and noninfected sugar beet plants at 67 days after inoculation. Data are presented as boxplots (noninfected: $n = 209$, infected: $n = 220$); stars mark significant differences at $P \leq 0.05$.

than 140 bands a quarter of the importance, of the most important band for both the petiole and leaf model, which affirms that the whole course of the spectral curve must be considered for classification of an ARSEPH infection rather than single spectral features.

Because disease incidence is the parameter extracted in this analysis, disease severity is not taken into consideration. Assessing the severity of SBR is still a complicated task either visually or digitally. Even in a controlled environment with artificial inoculation, biological biases can occur; for example, *P. leporinus* can feed predominantly on certain sugar beet plants in a grouped inoculation, resulting in faster and more severe symptoms on those individuals. Additionally, symptoms on the leaves can develop at different rates depending on the number of insects and time spent feeding, leveling out effects if average spectral responses are considered. To enhance the classification based on the leaves, it is necessary to consider single leaf samples (Barreto et al. 2023b). This approach facilitates the classification of symptoms at the leaf level rather than the canopy level, thereby enabling more precise estimation of disease severity.

In addition to the alterations in the phenotypic appearance of the sugar beet canopy caused by ARSEPH infection, the taproot also exhibited symptoms (Fig. 5B). Deformations of the sink organ are expected when phytopathogens interfere with the vascular system of the plant (Wei et al. 2023). Boruta-SHAP not only ranked the 22 most important parameters by their impact on the model but also categorized the values of the 3D parameters themselves. The variance of the ranking by absolute mean SHAP indicated a similar effect of all 22 relevant 3D parameters on the Boruta-SHAP model. However, certain value regions of some 3D parameters stood out in terms of their impact on the model. When analyzing the spatial distribution, the “Roundness of the largest circle” has the greatest impact below the hypocotyl of the sugar beet, the region in which brownish discoloration of the vascular bundles is most prevalent. The diverging importance in the taproot’s spatial dimension emphasizes the relevance of evaluating 3D parameters in this dimension as well. To compare the effects on different varieties, the region below the sugar beet hypocotyl should be examined on account of the physiological response to an ARSEPH infection in this region. Morphological effects from phytopathogens on the root system are mostly described with reduced or stunted growth; detailed phenotypic descriptions help to characterize effects and may help to quantify differences in the damage potential on different sugar beet varieties.

Digital phenotyping is emerging as an increasingly important tool for plant breeding. The digital phenotypic description of SBR presented in this research serves as a foundational framework for digital SBR disease monitoring, facilitating the screening of sugar beet varieties for tolerance or resistance under controlled conditions. Distinct changes caused by SBR could be described and can be used as the basis for the comparison of tolerance levels of different sugar beet varieties. The parameters identified can be

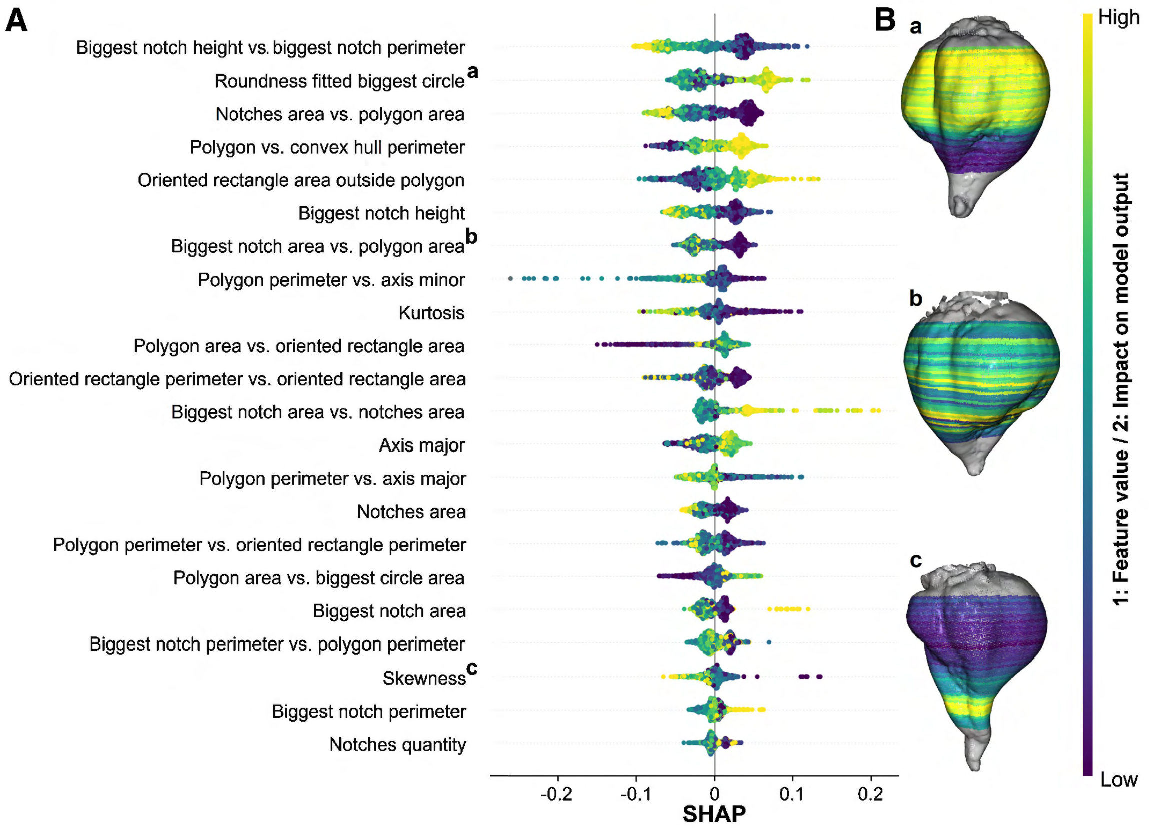

Fig. 5. A, Bee swarm plot of SHAP values from the 3D parameter impact on the Boruta-SHAP model and **B,** spatial importance heatmap of three spatially contrasting 3D parameters. In the graph, each dot is representative of a SHAP value for a taproot slice of a given feature. The color of each dot serves as a visual indicator of the feature value. High values are represented by yellow, and low values are represented by purple. The ranking of the 3D parameters (from top to bottom) and the spatial heatmap are determined by the mean absolute SHAP values from all taproot slices (noninfected: $n = 707$, infected: $n = 665$) of the feature and its height, respectively. The displayed taproot point clouds (Ba and Bc) illustrate the morphological changes caused by a ‘*Candidatus* Arsenophonus phytopathogenicus’ infection compared with a noninfected taproot (Bb). The 3D parameter illustrations (Ba, Bb, and Bc) express the spatial distribution of importance over the sugar beet taproot of different 3D parameters.

used to assess morphological changes to the leaves caused by an ARSEPH infection to compare variety responses. Furthermore, when the average petiole reflectance is considered, the analysis of the spectral response of the canopy is a robust method for assessing disease incidence. A major outcome of this study is that sugar beet petioles are more important indicators of ARSEPH infection compared with leaves. Averaging the reflectance over the whole canopy might have obliterated effects on the leaves because the symptom distribution and severity is not equal over the whole canopy, especially at earlier disease stages. Thus, using single leaves for analysis can increase the accuracy and help to establish a robust estimation of disease severity in the future, which is helpful for comparing the tolerance of different varieties. Beyond the canopy, changes to taproot 3D parameters caused by ARSEPH infection are unequally distributed in the upper, middle, and lower regions of the taproot. Therefore, it is advisable to set thresholds in line with the severity of changes to focus machine learning models for variety comparison on the regions with greatest signal change. However, the potential for variation in parameters caused by SBR, as outlined in this study, necessitates further empirical testing on more sugar beet varieties with an established range in tolerance to SBR.

Acknowledgments

We thank Dirk Koops and Jonathan Eggers for their invaluable contributions to the annotation of reference data, measurements, and the construction of the hyperspectral measurement chamber, and Zahra Shoaei for her assistance during the molecular diagnosis process.

Literature Cited

Agyei, K., Detring, J., Metzner, R., Huber, G., Pflugfelder, D., Eini, O., Varrelmann, M., Mahlein, A.-K., and Koller, R. 2025. Syndrome "basses richesses" disease induced structural deformations and sectorial distribution of photoassimilates in sugar beet taproot revealed by combined MRI-PET imaging. Plant Phenomics 7:100053.

Akhtar, M. S., Zafar, Z., Nawaz, R., and Fraz, M. M. 2024. Unlocking plant secrets: A systematic review of 3D imaging in plant phenotyping techniques. Comput. Electron. Agric. 222:109033.

Barreto, A., Ispizua Yamati, F. R., Varrelmann, M., Paulus, S., and Mahlein, A.-K. 2023a. Disease incidence and severity of Cercospora leaf spot in sugar beet assessed by multispectral unmanned aerial images and machine learning. Plant Dis. 107:188-200.

Barreto, A., Paulus, S., Varrelmann, M., and Mahlein, A.-K. 2020. Hyperspectral imaging of symptoms induced by *Rhizoctonia solani* in sugar beet: Comparison of input data and different machine learning algorithms. J. Plant Dis. Prot. 127:441-451.

Barreto, A., Reifenrath, L., Vogg, R., Sinz, F., and Mahlein, A.-K. 2023b. Data augmentation for mask-based leaf segmentation of UAV-images as a basis to extract leaf-based phenotyping parameters. Kunstliche Intell. 37: 143-156.

Behmann, J., Mahlein, A.-K., Paulus, S., Kuhlmann, H., Oerke, E. C., and Plümer, L. 2015. Calibration of hyperspectral close-range pushbroom cameras for plant phenotyping. ISPRS J. Photogramm. Remote Sens. 106:172-182.

Bohnenkamp, D., Behmann, J., Paulus, S., Steiner, U., and Mahlein, A.-K. 2021. A hyperspectral library of foliar diseases of wheat. Phytopathology 111:1583-1593.

Bömer, J., Esser, F., Marks, E., Rosu, R. A., Behnke, S., Klingbeil, L., Kuhlmann, H., Stachniss, C., Mahlein, A.-K., and Paulus, S. 2024. A 3D printed plant model for accurate and reliable 3D plant phenotyping. Gigascience 13:1-15.

Bradski, G. 2000. The OpenCV library. Dr. Dobb's J. 25:120-123.

Breiman, L. 2001. Random forests. Mach. Learn. 45:5-32.

Bressan, A. 2014. Emergence and evolution of *Arsenophonus* bacteria as insect-vectored plant pathogens. Infect. Genet. Evol. 22:81-90.

Bressan, A., Terlizzi, F., and Credi, R. 2012. Independent origins of vectored plant pathogenic bacteria from arthropod-associated *Arsenophonus* endosymbionts. Microb. Ecol. 63:628-638.

Cubero, J., Zarco-Tejada, P. J., Cuesta-Morrondo, S., Palacio-Bielsa, A., Navas-Cortés, J. A., Sabuquillo, P., Poblete, T., Landa, B., and Garita-Cambronero, J. 2024. New approaches to plant pathogen detection and disease diagnosis. Phytopathology 114:1989-2006.

Detring, J., Barreto, A., Mahlein, A. K., and Paulus, S. 2024. Quality assurance of hyperspectral imaging systems for neural network supported plant phenotyping. Plant Methods 20:1-16.

EPPO. 2012. 'Syndrome des basses richesses' detected in Germany: Addition to the EPPO Alert List. EPPO, Paris, France.

Fellows, R. J., and Geiger, D. R. 1974. Structural and physiological changes in sugar beet leaves during sink to source conversion. Plant Physiol. 54: 877-885.

Gatineau, F., Jacob, N., Vautrin, S., Larrue, J., Lherminier, J., Richard-Molard, M., and Boudon-Padieu, E. 2002. Association with the syndrome "basses richesses" of sugar beet of a phytoplasma and a bacterium-like organism transmitted by a *Pentastiridius* sp. Phytopathology 92:384-392.

Gatineau, F., Larrue, J., Clair, D., Lorton, F., Richard-Molard, M., and Boudon-Padieu, E. 2001. A new natural planthopper vector of stolbur phytoplasma in the genus *Pentastiridius* (Hemiptera: Cixiidae). Eur. J. Plant Pathol. 107:263-271.

Geiger, D. R., Saunders, M. A., and Cataldo, D. A. 1969. Translocation and accumulation of translocate in the sugar beet petiole. Plant Physiol. 44:1657-1665.

Gonella, E., Tedeschi, R., Crotti, E., and Alma, A. 2019. Multiple guests in a single host: Interactions across symbiotic and phytopathogenic bacteria in phloem-feeding vectors – A review. Entomol. Exp. Appl. 167:171-185.

He, K., Zhang, X., Ren, S., and Sun, J. 2016. Deep residual learning for image recognition. Pages 770-778 in: IEEE Conference on Computer Vision and Pattern Recognition (CVPR), Las Vegas, NV.

Ispizua Yamati, F. R., Günder, M., Barreto, A., Bömer, J., Laufer, D., Bauckhage, C., and Mahlein, A.-K. 2024. Automatic scoring of Rhizoctonia crown and root rot affected sugar beet fields from orthorectified UAV images using machine learning. Plant Dis. 108:711-724.

Keany, E. 2022. Boruta-SHAP. GitHub. https://github.com/Ekeany/Boruta-Shap

Kursa, M. B., Jankowski, A., and Rudnicki, W. R. 2010. Boruta - A system for feature selection. Fundam. Inform. 101:271-285.

Kuska, M. T., Brugger, A., Thomas, S., Wahabzada, M., Kersting, K., Oerke, E. C., Steiner, U., and Mahlein, A.-K. 2017. Spectral patterns reveal early resistance reactions of barley against *Blumeria graminis* f. sp. *hordei*. Phytopathology 107:1388-1398.

Lehnert, L. W., Meyer, H., Obermeier, W. A., Silva, B., Regeling, B., and Bendix, J. 2018. Hyperspectral data analysis in R: The hsdar package. https://cran.r-project.org/web/packages/hsdar/

Liaw, A., and Wiener, M. 2002. Classification and regression by randomForest. R News 2:18-22. https://CRAN.R-project.org/doc/Rnews/

Lundberg, S. M., and Lee, S.-I. 2017. A unified approach to interpreting model predictions. Adv. Neural. Inf. Process. Syst. 30. https://doi.org/10.48550/arXiv.1705.07874

Mahillon, M., Groux, R., Bussereau, F., Brodard, J., Debonneville, C., Demal, S., Kellenberger, I., Peter, M., Steiner, T., and Schumpp, O. 2022. Virus yellows and syndrome "Basses Richesses" in western Switzerland: A dramatic 2020 season calls for urgent control measures. Pathogens 11:885.

Mahlein, A.-K. 2016. Plant disease detection by imaging sensors – Parallels and specific demands for precision agriculture and plant phenotyping. Plant Dis. 100:241-251.

Mahlein, A.-K., Kuska, M. T., Behmann, J., Polder, G., and Walter, A. 2018. Hyperspectral sensors and imaging technologies in phytopathology: State of the art. Annu. Rev. Phytopathol. 56:535-558.

Mahlein, A.-K., Steiner, U., Hillnhütter, C., Dehne, H.-W., and Oerke, E.-C. 2012. Hyperspectral imaging for small-scale analysis of symptoms caused by different sugar beet diseases. Plant Methods 8:3.

Meier, U., Bleiholder, H., Buhr, L., Feller, C., Hack, H., Heß, M., Lancashire, P. D., Schnock, U., Stauß, R., van den Boom, T., Weber, E., and Zwerger, P. 2009. The BBCH system to coding the phenological growth stages of plants – History and publications. J. Cult. Plants 61:41-52.

Nováková, E., Hypša, V., and Moran, N. A. 2009. *Arsenophonus*, an emerging clade of intracellular symbionts with a broad host distribution. BMC Microbiol. 9:1-14.

Okole, N., Yamati, F. R. I., Hossain, R., Varrelmann, M., Mahlein, A.-K., and Heim, R. H. 2023. Hyperspectral signatures and betalain indicator for beet mosaic virus infection in sugar beet. Pages 506-511 in: 2023 IEEE International Workshop on Metrology for Agriculture. IEEE.

Paulus, S. 2019. Measuring crops in 3D: Using geometry for plant phenotyping. Plant Methods 15:103.

Paulus, S., Behmann, J., Mahlein, A.-K., Plümer, L., and Kuhlmann, H. 2014a. Low-cost 3D systems: Suitable tools for plant phenotyping. Sensors 14:3001-3018.

Paulus, S., Dupuis, J., Mahlein, A.-K., and Kuhlmann, H. 2013. Surface feature based classification of plant organs from 3D laserscanned point clouds for plant phenotyping. BMC Bioinform. 14:238.

Paulus, S., Schumann, H., Kuhlmann, H., and Léon, J. 2014b. High-precision laser scanning system for capturing 3D plant architecture and analysing growth of cereal plants. Biosyst. Eng. 121:1-11.

Pfitzer, R., Rostás, M., Häußermann, P., Häuser, T., Rinklef, A., Detring, J., Schrameyer, K., Voegele, R. T., Maier, J., and Varrelmann, M. 2024. Effects of succession crops and soil tillage on suppressing the syndrome 'Basses Richesses' vector *Pentastiridius leporinus* in sugar beet. Pest Manag. Sci. 80:3379-3388.

Pfitzer, R., Varrelmann, M., Schrameyer, K., and Rostás, M. 2022. Life history traits and a method for continuous mass rearing of the planthopper *Pentastiridius leporinus*, a vector of the causal agent of syndrome 'Basses Richesses' in sugar beet. Pest Manag. Sci. 78:4700-4708.

Posit Team. 2025. RStudio: Integrated Development Environment for R. Posit Software, PBC, Boston, MA. http://www.posit.co/

Ronneberger, O., Fischer, P., and Brox, T. 2015. U-Net: Convolutional networks for biomedical image segmentation. In: Medical Image Computing and Computer-Assisted Intervention – MICCAI 2015. MICCAI 2015. Lecture Notes in Computer Science, vol. 9351. N. Navab, J. Hornegger, W. Wells, and A. Frangi, eds. Springer, Cham.

Savitzky, A., and Golay, M. J. E. 1964. Smoothing and differentiation of data by simplified least squares procedures. Anal. Chem. 36:1627-1639.

Sun, J., Yang, L., Yang, X., Wei, J., Li, L., Guo, E., and Kong, Y. 2021. Using spectral reflectance to estimate the leaf chlorophyll content of maize inoculated with arbuscular mycorrhizal fungi under water stress. Front. Plant Sci. 12:646173.

Taubin, G. 1991. Estimation of planar curves, surfaces, and nonplanar space curves defined by implicit equations with applications to edge and range image segmentation. IEEE Trans. Pattern Anal. Mach. Intell. 13: 1115-1138.

Urbanek, S. 2022. png: Read and write PNG images. http://www.rforge.net/png/

van Boxtel, G. J. M. 2021. gsignal: Signal processing. https://github.com/gjmvanboxtel/gsignal

Van Der Walt, S., Schönberger, J. L., Nunez-Iglesias, J., Boulogne, F., Warner, J. D., Yager, N., Gouillart, E., Yu, T., and The Scikit-Image Contributors. 2014. Scikit-image: Image processing in Python. PeerJ 2:e453.

Van Rossum, G., and Drake, F. L. 2009. Python 3 Reference Manual. CreateSpace.

Virtanen, P., Gommers, R., Oliphant, T. E., et al. 2020. SciPy 1.0: Fundamental algorithms for scientific computing in Python. Nat. Methods 17:261-272.

Wei, W., Barka, E. A., and Eichmeier, A. 2023. Editorial: Recent advances in crop diseases associated with plant vascular-colonizing bacteria. Front. Plant Sci. 14:1171973.

Winkelbach, S., Molkenstruck, S., and Wahl, F. M. 2006. Low-cost laser range scanner and fast surface registration approach. Lect. Notes Comput. Sci. 4174:718-728.

Xu, K., and Ye, H. 2023. Light scattering in stacked mesophyll cells results in similarity characteristic of solar spectral reflectance and transmittance of natural leaves. Sci. Rep. 13:4694.

Zscheile, F. P., Comar, C. L., and Mackinney, G. 1942. Interlaboratory comparison of absorption spectra by the photoelectric spectrophotometric method—Determinations on chlorophyll and Weigert's solutions. Plant Physiol. 17:666-670.

Zübert, C., and Kube, M. 2021. Application of TaqMan real-time PCR for detecting '*Candidatus* Arsenophonus phytopathogenicus' infection in sugar beet. Pathogens 10:1466.

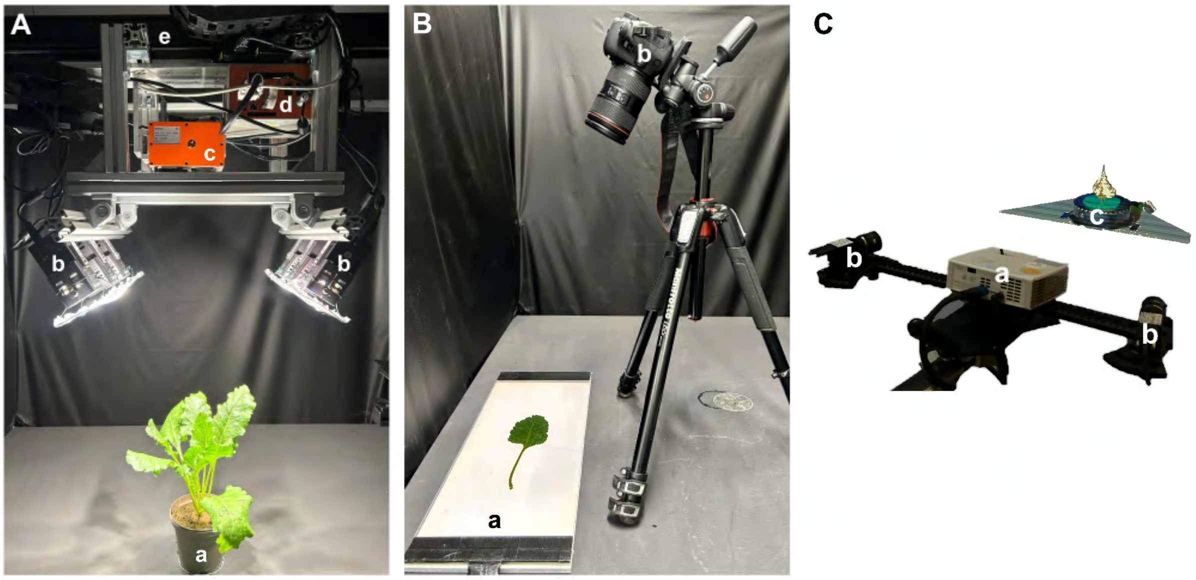

Supplementary Figure S1. Hyperspectral imaging set up (A). a: Sugar beet plant, b: Halogen illumination, c: Hyperspectral camera, d: Operating computer, e: Linear axis. Leaf 2D imaging set up (B). a: RGB camera, b: Leaf measuring cell. Taproot 3D measuring set up (C). a: 3D-scanner, b: Structured-light lamps, c: Sugar beet plant on rotating table.

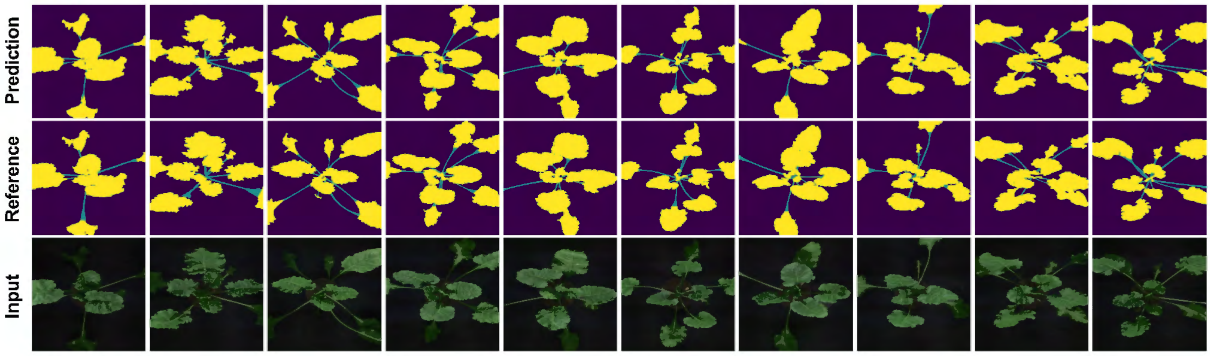

Supplementary Figure S2. Example test data set masks generated from the U-NET trained for canopy organ segmentation. Upper row: RGB images; middle row: Manually annotated reference images; lower row: U-NET segmented masks.

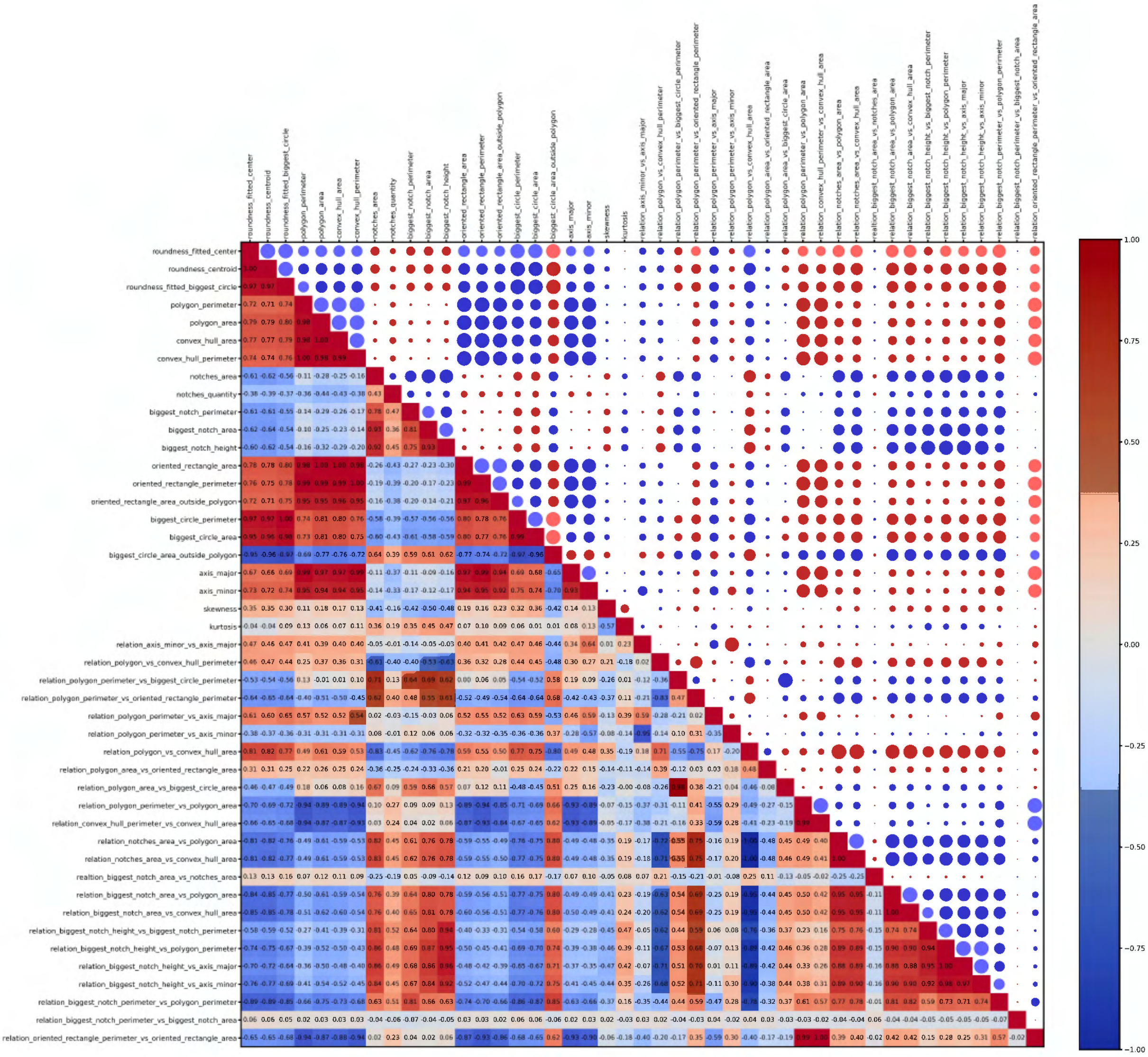

Supplementary Figure S3. Correlation matrix of 45 extracted 3D parameters from the 3D taproot data.

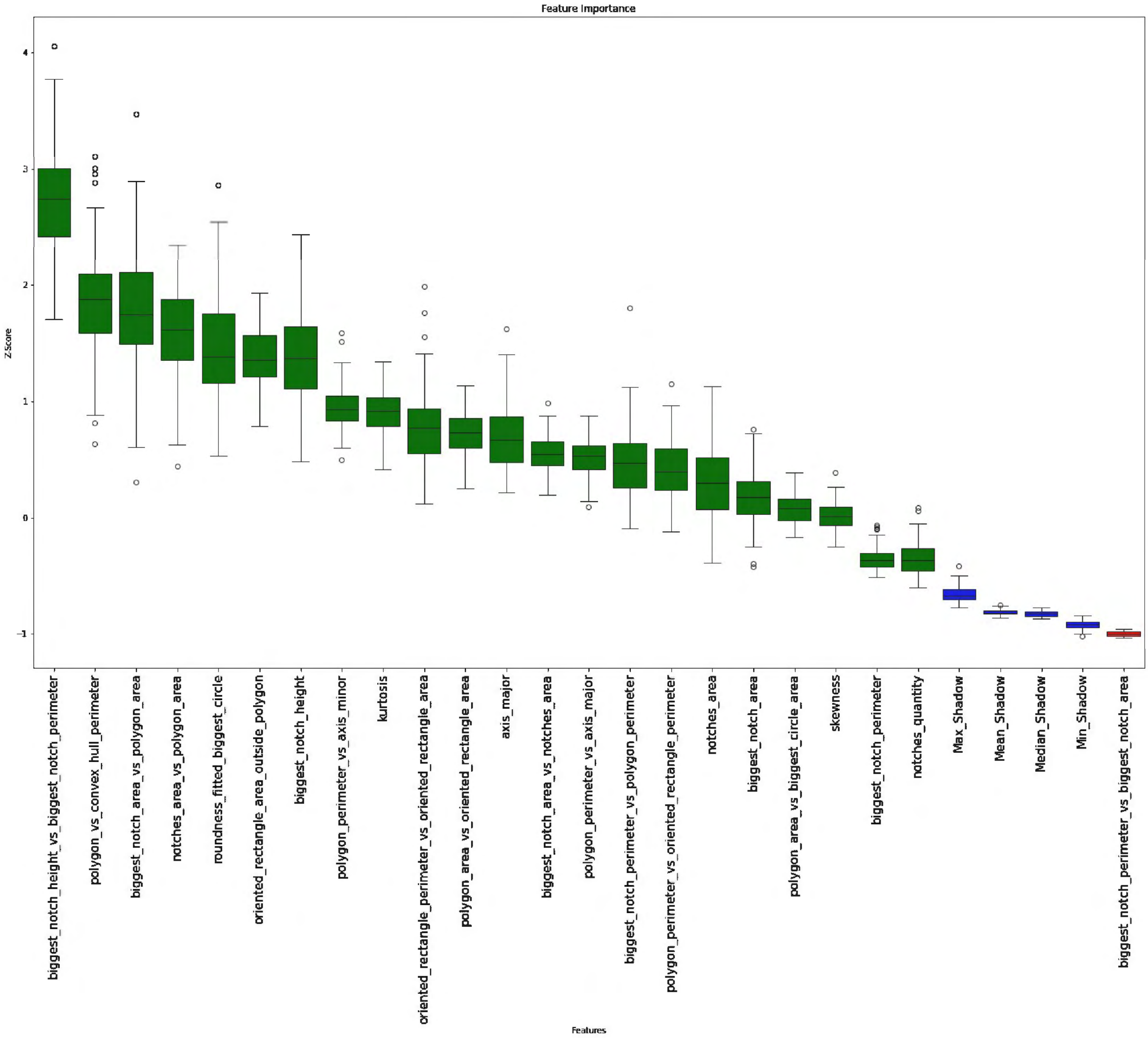

Supplementary Figure S4. Results of the Boruta feature selection for the Boruta-SHAP feature importance of 23 non-correlating 3D-parameter.

Supplementary Table S1. Cycle quantification (C_q) results of the quantitative polymerase chain reaction (qPCR) analysis. All inoculated samples and nine non-inoculated samples were chosen for analysis. All samples, the known positive and negative sample and the dilution series were repeated once.

		C_q repetition		**Mean C_q**
Sample	**Number**	**1**	**2**	
Inoculated	1	29.57	29.11	29.34
	2	27.28	27.00	27.14
	3	29.52	29.03	29.28
	4	27.03	26.92	26.97
	5	28.85	28.94	28.89
	6	28.92	28.58	28.75
	7	29.29	29.04	29.16
	8	27.69	27.19	27.44
	9	28.48	27.50	27.99
	10	28.08	27.70	27.89
	11	27.89	27.86	27.88
	12	28.17	28.04	28.11
	13	29.28	29.39	29.34
	14	28.30	28.64	28.47
	15	29.36	29.27	29.32
Non-	1	0.00	0.00	0.00
	2	39.03	0.00	39.03
	3	0.00	0.00	0.00
	4	39.67	0.00	39.67
	5	0.00	0.00	0.00
	6	0.00	0.00	0.00
	7	0.00	0.00	0.00
	8	0.00	0.00	0.00
	9	0.00	0.00	0.00
Dilution	100pg/µl	14.03	13.91	13.97
	10pg/µl	17.03	17.11	17.07
	1pg/µl	20.39	20.19	20.29
	100fg/µl	23.86	23.77	23.81
	10fg/µl	27.12	27.05	27.09
Positive		26.17	26.14	26.15
Negative		0.00	0.00	0.00

Supplementary Table S2. U-NET segmentation performance of the classes background, petioles and leaves.

Performance Class	Intersection over Union	Precision	Recall
Background	0.98	0.99	0.99
Petioles	0.67	0.78	0.82
Leaves	0.95	0.97	0.97

Supplementary Table S3. Definition of 45 parameters extracted from the 3D taproot cross sections.

Parameter Name	Definition
Roundness fitted center	Ratio of minimum to maximum distance from the polygon to a fitted circle center.
Roundness centroid	Ratio of minimum to maximum distance from the polygon to the centroid of the polygon.
Roundness fitted biggest circle	Ratio of minimum to maximum distance from the polygon to the largest inscribed circle.
Polygon perimeter	Total length of the boundary of the fitted polygon.
Polygon area	Total enclosed area of the polygon.
Convex hull area	Area of the smallest convex shape enclosing the polygon.
Convex hull perimeter	Perimeter of the smallest convex shape enclosing the polygon.
Notches area	Combined area of indentations (notches) between the polygon and its convex hull.
Notches quantity	Number of notches detected as indentations from the convex hull.
Biggest notch perimeter	Perimeter of the largest notch.
Biggest notch area	Area of the largest notch.
Biggest notch height	Maximum orthogonal depth of the largest notch.
Oriented rectangle area	Area of the minimum bounding rotated rectangle enclosing the polygon.
Oriented rectangle perimeter	Perimeter of the minimum bounding rotated rectangle enclosing the polygon.
Oriented rectangle area outside polygon	Area difference between oriented rectangle and polygon.
Biggest circle area	Area of the largest inscribed circle enclosing the polygon.
Biggest circle perimeter	Perimeter of the largest inscribed circle enclosing the polygon.
Biggest circle area outside polygon	Area difference between the largest inscribed circle and polygon.
Axis major	Longest distance between any two points on the polygon boundary.
Axis minor	Longest distance between any two points on the polygon boundary perpendicular to the major axis.
Skewness	Skewness of the radial distance distribution from the center.
Kurtosis	Kurtosis of the radial distance distribution from the center.
Relation axis minor vs. axis major	Ratio of minor axis to major axis length.
Relation polygon vs. convex hull perimeter	Ratio of polygon perimeter to convex hull perimeter.
Relation polygon perimeter vs. biggest circle perimeter	Ratio of polygon perimeter to the biggest inscribed circle perimeter.

Relation polygon perimeter vs. oriented rectangle perimeter	Ratio of polygon perimeter to oriented rectangle perimeter.
Relation polygon perimeter vs. axis major	Ratio of polygon perimeter to major axis length.
Relation polygon perimeter vs. axis minor	Ratio of polygon perimeter to minor axis length.
Relation polygon vs. convex hull area	Ratio of polygon area to convex hull area.
Relation polygon area vs. oriented rectangle area	Ratio of polygon area to oriented rectangle area.
Relation polygon area vs. biggest circle area	Ratio of polygon area to biggest inscribed circle area.
Relation polygon perimeter vs. polygon area	Ratio of polygon perimeter to its area.
Relation convex hull perimeter vs. convex hull area	Ratio of convex hull perimeter to its area.
Relation notches area vs. polygon area	Ratio of total notch area to polygon area.
Relation notches area vs. convex hull area	Ratio of total notch area to convex hull area.
Relation biggest notch area vs. notches area	Ratio of the biggest notch area to total notch area.
Relation biggest notch area vs. polygon area	Ratio of the biggest notch area to polygon area.
Relation biggest notch area vs. convex hull area	Ratio of the biggest notch area to convex hull area.
Relation biggest notch height vs. biggest notch perimeter	Ratio of biggest notch height to its perimeter.
Relation biggest notch height vs. polygon perimeter	Ratio of biggest notch height to polygon perimeter.
Relation biggest notch height vs. axis major	Ratio of biggest notch height to major axis length.
Relation biggest notch height vs. axis minor	Ratio of biggest notch height to minor axis length.
Relation biggest notch perimeter vs. polygon perimeter	Ratio of biggest notch perimeter to polygon perimeter.
Relation biggest notch perimeter vs. biggest notch area	Ratio of biggest notch perimeter to its area.
Relation oriented rectangle perimeter vs. oriented rectangle area	Ratio of oriented rectangle perimeter to its area.

CHAPTER 5: Morphological and physiological alterations caused by *Candidatus* Arsenophonus phytopathogenicus on different sugar beet varieties – Publication III

Accepted manuscript and published online in Sugar Industry 151:60-68 (2026). https://doi.org/10.36961/si34198.

Justus Detring[1*], Jonas Bömer[1], Christa M. Hoffmann[1], Anne-Katrin Mahlein[1]

[1]Institute of Sugar Beet Research, 37079 Göttingen, Germany

*Corresponding author: Justus Detring; E-mail: detring@ifz-goettingen.de

Keywords: Syndrome “Basses Richesses”, 3D-scanning, taproot texture, alcohol insoluble residues, marc content, variety screening, phenotyping

Author contributions: Conceptualization: JD, JB, AKM. Methodology: JD, JB. Investigation: JD, JB. Visualization: JD, JB. Funding Acquisition: AKM. Project Administration: AKM. Supervision: AKM. Writing Original Draft: JD, JB. Writing Review & Editing: JD, JB, CH, AKM.

DOI: 10.36961/si34198 | **Cite this:** *Sugar Industry 151* (2026), 60–68

Sugar Industry international

Morphological and physiological alterations caused by *Candidatus* Arsenophonus phytopathogenicus on different sugar beet varieties

Justus Detring*, Jonas Bömer, Christa M. Hoffmann, Anne-Katrin Mahlein

Institute of Sugar Beet Research, 37079 Göttingen, Germany
* Corresponding author, detring@ifz-goettingen.de

Abstract: First sugar beet varieties with reasonable yield stability under infection with *Candidatus* Arsenophonus phytopathogenicus (ARSEPH), the causal agent of the syndrome "Basses Richesses" (SBR), were discovered, but the mechanisms behind this have not been described yet. Thus, this research aimed at analyzing different morphological, physiological and quality related traits of ARSEPH infected sugar beet taproots to identify methods for SBR variety screening. In a greenhouse experiment, one susceptible and two tolerant varieties were infected with ARSEPH via the vector *Pentastiridius leporinus* (reed glass-winged cicada) under controlled conditions. In the susceptible variety, an infection with ARSEPH caused an average reduction in volume (~40%), length (~6%), width (~21%), fresh mass (~41%) and an increase in dry matter content (~5%). The tolerant varieties exhibited a lower effect on these parameters but showed a greater increase in alcohol insoluble residues (cellulose, hemicellulose, pectin, lignin) and marc content. The significant enhancement in flexural taproot tissue strength observed in the tolerant varieties may be linked to increased levels of structural cell components. The susceptible and one tolerant variety exhibited reduced periderm puncture resistance after infection. This first study of physiological and morphological traits provides deeper insights into host-pathogen interaction and potential variety response. To confirm the relevance and implications of the results as new parameters for screening of SBR-tolerant varieties, further analysis with additional varieties across a larger number of samples is necessary.

Keywords: Syndrome "Basses Richesses", 3D-scanning, taproot texture, alcohol insoluble residues, marc content, variety screening, phenotyping

1 Introduction

Syndrome "Basses Richesses" (SBR) has evolved into one of the most important sugar beet diseases in central Europe. Originally found in Burgundy, France in the early 1990s (Gatineau *et al.* 2002), SBR has spread to Germany, Switzerland, Hungary and Austria in the last decades (Lang *et al.* 2025). The rapid spread, devastating damage and economic significance of the disease create an urgent need for disease control. Two bacterial pathogens are associated with SBR: *Candidatus* Arsenophonus phytopathogenicus (ARSEPH) and *Candidatus* Phytoplasma solani (PHYPSO), both transmitted by *Pentastiridius leporinus*, the main vector of SBR (Gatineau *et al.* 2002). As neither ARSEPH nor PHYPSO has yet been artificially cultivated, vector-based transmission via *P. leporinus* is the only way to establish a controlled infection of sugar beet. *Candidatus* phytoplasma solani is not transmitted to the offspring by *P. leporinus*, leaving a single infection with ARSEPH as the only option when relying on a controlled laboratory rearing of *P. leporinus* for inoculation up to now (Bressan 2014; Pfitzer *et al.* 2022).

Recent investigations have shown a decreasing impact of adapting crop rotations and tillage methods on the *P. leporinus* population (Bressan 2009, 2014; Pfitzer *et al.* 2024). However, the extensive host range of *P. leporinus* complicates the implementation of such methods aimed at reducing the population to achieve adequate disease control. The cultivation of tolerant varieties has been demonstrated to be an effective strategy for disease control. Thus, the search for SBR-tolerant varieties is the most effective strategy for controlling SBR in the strongly insecticide-restricted European Union (Storck *et al.* 2017). The symptoms of SBR have been described by Gatineau *et al.* (2002) with yellowing of the older leaves and new small, narrow shoots with chlorotic lamina, asymmetrical and curvature appearance, as well as brownish discoloration of the taproot vascular tissue. Further description of the canopy and morphological taproot alterations caused by SBR have been provided by Detring *et al.* (2025) but a connec-

---

Paper received November 4, 2025; reviewed November 24, 2025; accepted December 8, 2025.

tion to the physiological changes especially in the taproot is still missing. The hypothesized lignification of cell walls caused by SBR (Gatineau *et al.* 2002) is a wellknown response to other bacterial infections. Lignification makes the plant more resistant to hydrolytic enzymes, limits the pathogens' access to nutrients and decreases the diffusion of their toxins into plant cells (Morkunas *et al.* 2014; Smith *et al.* 2007). Likewise, sugar beet marc, as a structural taproot component, is known to improve taproot storability by enhancing mechanical strength and cell wall integrity, thereby hindering infestations by storage pathogens (Hoffmann *et al.* 2018; Kleuker *et al.* 2022).

However, the role of structural plant components, such as lignin and marc, and their effects on the susceptibility of different sugar beet varieties to SBR are unknown. Additionally, the impact of SBR on morphological taproot parameters such as volume, length and width, has not yet been determined. Moreover, the dynamic spread of *P. leporinus* in Germany has led to an increased prevalence of PHYPSO (Lang *et al.* 2025), with symptoms shifting toward those of rubbery taproot diseases, which are also caused by a cixiid-transmitted phytoplasma (Ćurčić *et al.* 2021). This has raised new questions about the effects of SBR-associated pathogens on the taproot texture and their relevance to screening for SBR tolerant varieties.

The role of the variety-specific taproot texture for harvest and storage quality has been intensely studied, presenting varieties with stronger tissue as more robust against harvest and storage damage, as well as less susceptible to pathogen infestations (Hoffmann *et al.* 2018; Kleuker *et al.* 2021; Nause *et al.* 2020; Schnepel *et al.* 2016). Taproot tissue strength is based on several factors, of which the level and composition of the cell walls are the most important (Kleuker *et al.* 2022). The plant cell wall consists mainly of cellulose, hemicellulose, lignin and pectin. These components are all alcohol insoluble which enables quantification via filtration and the use of ethanol as a solvent. The results of this filtration can then be summarized as alcohol insoluble residues (AIR). The water insoluble residues of the sugar beet taproot cell wall are defined as the marc content (Hoffmann *et al.* 2018). Sugar beet marc content is also described as a relevant parameter for determining tissue strength and is closely related to AIR (Kleuker *et al.* 2022).

If physiological parameters such as AIR and marc content and morphological parameters such as volume, length, width and texture profile, are affected by SBR, they might provide

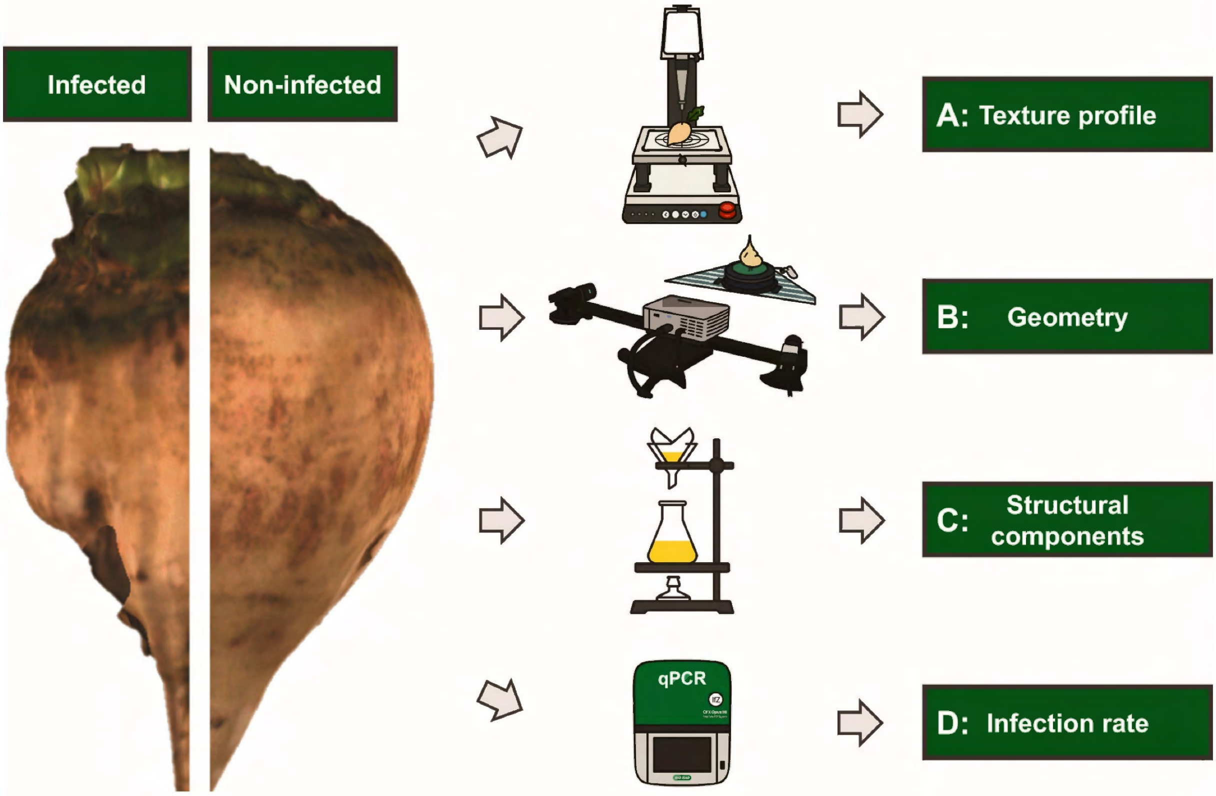

Fig. 1: Approach for the extraction of *Candidatus* Arsenophonus phytopathogenicus (ARSEPH) infected sugar beet taproot (shown left as colorized three-dimensional scan) parameters of varieties with different tolerance levels to syndrome "Basses Richesses". The sugar beet taproot analysis approach consists of four different methods; A: Texture profile analysis, B: Three-dimensional scanning, C: Determination of structural components, dry matter, fresh mass, and D: Molecular diagnostic of ARSEPH.
Texture profile analysis yielded the parameters: Puncture resistance of the periderm, tissue firmness, flexural strength and elasticity. Additionally, three fundamental geometric parameters (volume, length, width) were derived from the three-dimensional measurements. Furthermore, dry matter and fresh mass analysis as well as the filtration of alcohol insoluble residues (cellulosis, hemicellulosis, lignin, pektin) and marc presents information on the distribution of the contents of structural components of the taproot. Lastly, Molecular diagnostics deliver exact ARSEPH infection rates.

information for comparing tolerance levels among different sugar beet varieties. Therefore, this research investigated four fundamental traits (structural components, infection rate, geometry and texture) of the sugar beet taproot (Figure 1) of three varieties under the influence of SBR. The aim is to describe morphological and physiological parameters that can be used to screen varieties for their tolerance to SBR. Furthermore, first indications are drawn from the results on the effects of SBR on the physiology of the taproot. Especially the impact on the contents of structural components such as marc and AIR can reveal physiological alterations of the taproot, possibly caused by plant defense mechanisms induced by SBR. Additionally, future research demands could be derived from this study.

2 Materials and methods

2.1 Cultivation and inoculation of sugar beet

The preparation of *Candidatus* Arsenophonus phytopathogenicus-infected sugar beet plant material under controlled conditions was adapted from Detring *et al.* (2025). One susceptible variety and two tolerant varieties were selected based on their susceptibility and tolerance to SBR (Bundessortenamt 2025).

Seeds were sown at a depth of 1 cm in polypropylene pots filled with Fruhstorfer soil type P 25 (HAWITA Gruppe GmbH, Vechta, Germany) in the greenhouse. After emergence (seven days), ten seedlings were transferred into 1 L round pots containing fertilized sandy topsoil (Gustav Lehmann Mörtel- u. Kieswerke GmbH, Burgdorf, Germany). Subsequently, the sugar beet plants were cultivated in the greenhouse for a period of 14 days (14:10 h light/dark photoperiod, 25.0 ± 5.7 °C, 49.0 ± 15.7% relative humidity, and approximately 225 µmol/[sm] full spectrum light) until BBCH 12 (Meier *et al.* 2009).

For inoculation sugar beet plants were cultivated in 12 insect rearing tents (Mega View Science Co., Taichung, Taiwan) with dimensions of 60 · 60 · 60 cm (length · width · height) and a mesh size of 150 · 150 (160 µm aperture). In each tent, five sugar beet plants were placed. Subsequently, the tents were transferred into a climate chamber, which was configured to maintain a 16:8 h light/dark photoperiod with an average temperature of 24.2 (±1.5) °C, a relative humidity of 54.5 (±4.7)%, and an illumination level of approximately 250 µmol/[sm] full spectrum light during inoculation. Of the 12 tents, six housed 25 *P. leporinus* adults and the other six were the non-inoculated controls without insects. The insects were transferred into the tents using an insect exhauster (Ehlert & Partner GbR, Nieder-Kassel-Rheidt, Germany). In total, there were 10 repetitions per plans for each variety and variant.

The *P. leporinus* adults utilized for inoculation were derived from a laboratory-rearing protocol outlined by Pfitzer *et al.* (2022). The inoculation was conducted over nine days. After the inoculation process, the living *P. leporinus* adults were removed from the tents and all sugar beet plants were sprayed with a 0.35% Confidor WG 70 (Bayer Crop Science AG, Monheim, Germany) water mixture. Following the insecticide treatment, the sugar beets were cultivated in the greenhouse for 62 days until harvest. The greenhouse was maintained under a 14:10 h light/dark photoperiod, with an average temperature of 25.0 (±5.7) °C, relative humidity of 45.2 (±15.9)%, and an approximate full-spectrum light intensity of 225 µmol/[sm]. During the cultivation process, the sugar beet plants were watered daily and fertilized every three weeks with 50 mL of a liquid fertilizer mixture, with 4% nitrogen, 2% phosphorus pentoxide, and 2% potassium oxide, which was mixed with tap water at a ratio of 1:40. The sugar beet plants were harvested 71 days after inoculation (dai).

2.2 Three-dimensional scanning of taproots and morphological parameter extraction

At harvest, the taproots of all cultivated sugar beet plants were three-dimensionally (3D) scanned to analyze possible deformations of the taproot induced by SBR according to Detring *et al.* (2025). The 3D surface meshes of the sugar beet taproots were subsequently analyzed using Python (version: 3.10.14) and the Open3D library (version: 0.17). Prior to parameter extraction, the surface meshes were preprocessed by removing non-manifold edges, degenerate or duplicated elements, and unreferenced vertices. They were finally down sampled to a resolution of 1 mm.

Subsequently, the taproot volume was computed directly from the closed mesh geometry. The length was determined as the maximal vertical extent of the mesh along its length axis, corresponding to the distance between the lowest and highest vertices. The width was defined as the maximum cross-sectional diameter of the root, obtained by slicing the mesh into 1 mm cross-sectional layers perpendicular to the length axis and calculating the largest pairwise Euclidean distance between vertices within each slice. The largest value across all slices was reported as taproot width.

2.3 Texture profile analysis

The texture profile analysis of the sugar beet taproots was modified according to Kleuker *et al.* (2019) and consisted of measuring the puncture resistance of the periderm, the tissue firmness, the flexural strength and the elasticity with a texture analyzer equipped with a 100 kg load cell (TA. XTplus100, Stable Micro Systems, Godalming, UK). The puncture resistance of the periderm was measured with a 2 mm cylindrical probe and a crosshead speed of 60 mm min^{-1}, recording the maximum force until rupture. Three measurements were made in a radial circle at the broadest part of each taproot. After rupture of the periderm at depths of 0.5–5 mm, the tissue firmness was determined. The flexural strength is the force needed to break a taproot slice, while the elasticity is the time needed to break a taproot slice. To assess these parameters, one cuboid of each taproot was cut vertically from the middle part of the taproot with the dimensions of 10 cm · 1 cm · 2 cm (length · height · width). The force and the time until breakage was determined on a three-point bending device with a span of 32 mm.

2.4 Determination of marc content, alcohol insoluble residues and dry matter content

After the texture profile analysis, the respective taproots were mashed by cutting them into small pieces and mixing them in a blender (MultiQuick 9195XLI, Braun, Kronberg im Taunus, Germany). The mashed samples were transferred into small plastic cups, closed and stored at −20 °C for further analysis.

The marc content, which is the water insoluble rest of the taproot material related to fresh mass, was analyzed according to Reinefeld *et al.* (1983) and Werner (1966). For the marc content analysis, the samples were washed 4 times with hot demineralized water to remove the soluble material, then washed with acetone and dried at 105 °C.

The AIR analysis was conducted according to McFeeters *et al.* (1984). Around 25 g of mashed taproot material was washed with 100 mL 97% ethanol and homogenized in a blender (MultiQuick 9195XLI, Braun, Kronberg im Taunus, Germany). The solid remains were again washed with 50 mL of 97% ethanol, in a third step with 50 mL acetone. The remains were dried at 105 °C for 12 hours.

For the determination of the dry matter content, the remaining mashed taproot samples were dried at 105 °C for a duration of 48 h. The dry matter content was expressed as a percentage of the fresh mass.

2.5 Molecular diagnostics of *Candidatus* Arsenophonus phytopathogenicus

During experimental harvest, taproot tissue samples were collected from both inoculated and non-inoculated plants for the molecular detection of ARSEPH. The taproot was cut beneath the hypocotyl to collect approximately 100 mg of brownish, discolored taproot tissue from the infected roots and representative samples from the non-infected roots, respectively. Alterations of the taproot vascular bundles caused by SBR are presented in Figure 2.

The crown of the taproots was discarded and the topped taproots were weighed to determine the fresh mass. The tissue samples were collected in 1.5 mL Eppendorf tubes (Eppendorf SE, Hamburg, Germany). The tubes were frozen in liquid nitrogen and stored at −80 °C. The frozen samples were subsequently manually ground with a metal grinder in the tubes, which resulted in a powdery consistency. This was a preparatory measure for the subsequent purification of deoxyribonucleic acid (DNA). DNA was purified using the NucleoSpin Plant II Mini Kit for DNA from plants, a product of MACHEREYNAGEL GmbH & Co. KG, located in Düren, Germany. The purified DNA was transferred twice into a well on a 96-well plate (Bio-Rad Laboratories GmbH, Feldkirchen, Germany).

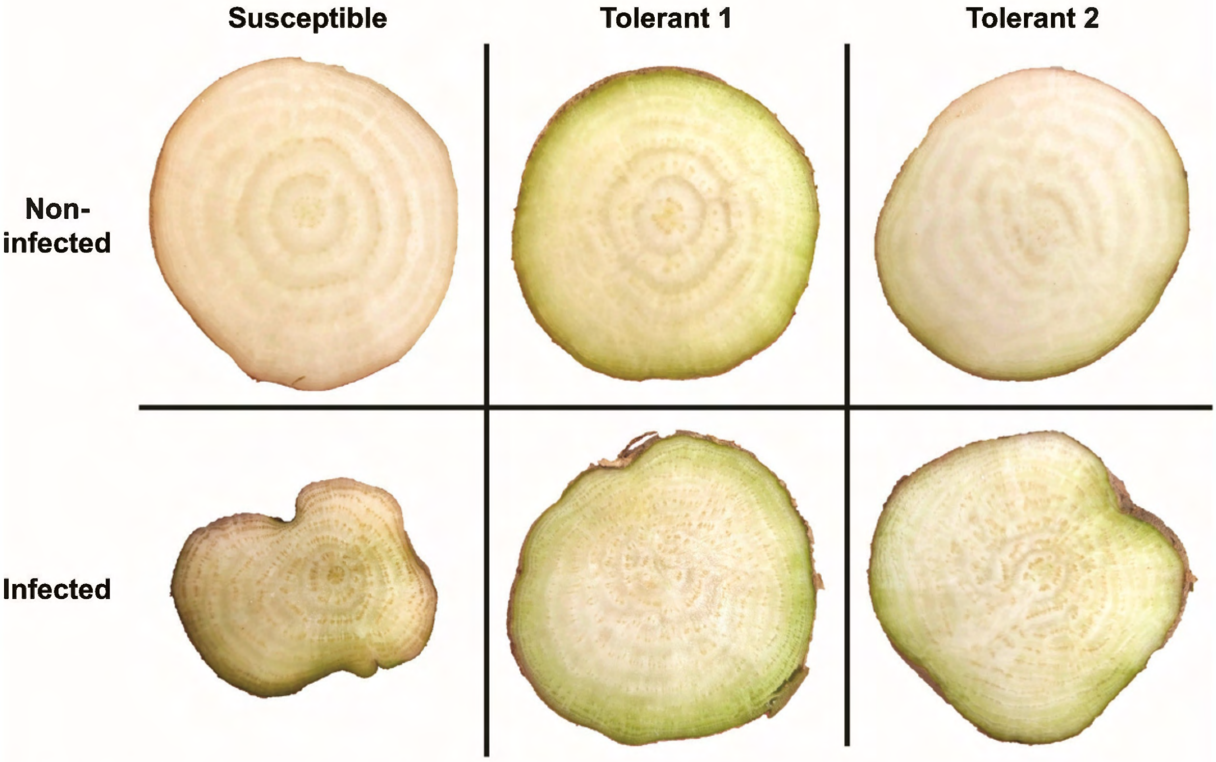

Fig. 2: Cross sections of *Candidatus* Arsenophonus phytopathogenicus infected and non-infected taproots of the varieties 71 days after inoculation with *Pentastiridius leporinus* adults

Furthermore, water and positive samples were added twice to the plate as negative and positive controls, respectively. Additionally, a dilution series of the purified amplicon of the target gene, heat shock protein 20 (*hsp20*), was added twice to the plate. To detect *hsp20* from ARSEPH in inoculated plants, a real-time polymerase chain reaction (qPCR) assay was employed, utilizing primers as described in Zübert *et al.* (2021). The quantitative polymerase chain reaction (qPCR) mixture contained 6.3 µl of distilled water, 10 µl of Maxima Probe qPCR Mix, 0.9 µl of each primer, 0.4 µl of probe (10 µM; Fam-BHQ1 labelled) and 1.5 µl of sample DNA. A CFX96 Real-Time System C1000 Touch Thermal Cycler (Bio-Rad Laboratories GmbH, Feldkirchen, Germany) was utilized for qPCR with the following cycle conditions: the initial temperature was set to 95 °C, and the reaction was allowed to proceed for a duration of three minutes. This was followed by 40 cycles at 95 °C for 15 s and 60 °C for 30 s. After the qPCR, the results were processed in CFX Manager (version 3.1, Bio-Rad Laboratories GmbH, Feldkirchen, Germany). Samples were considered infected with ARSEPH if the cycle quantification (Cq) value was ≤34.00. One inoculated sample was considered infected despite a Cq value >34.00, as it exhibited distinct brown discoloration of the vascular bundles.

2.6 Statistical analysis

The statistical analysis and graphical presentation were conducted using R (version: 4.3.1, R Core Team, Vienna, Austria) and RStudio (version: 2024.04.2+764, Posit team 2025). The data set was subjected to a series of statistical tests to ascertain its distribution and homogeneity of variance. Initially, the Shapiro-Wilk test (Shapiro *et al.* 1972) was employed to assess the normality of the data. This was followed by the Levene test (Levene 1960), which was used to determine the homogeneity of variance within the data. Data that were not normally distributed or had heterogeneous variances underwent data transformation. Subsequently, an analysis of variance was conducted (Fisher 1919) and a post-hoc Tukey test (Tukey 1949) was implemented to ascertain significant differences between treatments and varieties at a significance level of $p \leq 0.05$.

3 Results

3.1 Infection rate, morphological parameters and structural components

The inoculation of sugar beet varieties with *P. leporinus* adults yielded in disparate infection rates with ARSEPH (Table 1). The susceptible sugar beet variety exhibited an average infection rate of 70%, while the tolerant varieties had infection rates of 50% and 90%, respectively. For further analyses, only plants that had been definitively diagnosed with ARSEPH were included.

The impact of an ARSEPH infection on morphological and structural parameters of the varieties is presented in Figure 3 and in conjunction with the subsequent outbreak of SBR, an ARSEPH infection resulted in a significant reduction of 41% of the fresh mass of the taproots from the SBR-susceptible variety compared to the non-infected variant of this variety. In contrast, the tolerant varieties showed a fresh mass reduction of approximately 7% and 14%, respectively, which was not significant. All varieties showed increased in dry matter content. The susceptible variety showed the greatest increase, by ca. 5%, accompanied by a substantial decrease in volume (approximately 40%) and width (21%). No significant reductions in volume or taproot width occurred in the tolerant varieties. All three varieties had no significant reduction in taproot length.

Table 1: *Candidatus* Arsenophonus infection rates of the sugar beet varieties 71 days after an inoculation period of eleven days with five *Pentastiridius leporinus* adults per sugar beet plant

Variety	Infection rate in %
Susceptible	70
Tolerant 1	50
Tolerant 2	90

The ARSEPH-infected treatments of all varieties showed a non-significant increase in AIR and marc content. The susceptible variety had a rise in AIR of approximately 0.4%. Tolerant variety 1 and 2 showed increases of approximately 1.1% and 0.4%, respectively. The marc content was increased by about 0.1% in the susceptible variety and 0.3% in variety tolerant 1 and 0.5% in variety tolerant 2.

3.2 Texture parameters

An infection with ARSEPH altered the texture profile of the taproots of the varieties (Fig. 4). A significantly lower force was required to rupture the periderm of the ARSEPH-infected taproots from the susceptible variety (~19%) and tolerant variety 2 (~9%). For tolerant variety 1, the level of puncture resistance in infected and non-infected plants was comparable.

For all varieties, the firmness of the taproot tissue up to 5 mm below the periderm was not significantly different between infected and non-infected plants.

The flexural strength of the taproot pieces was significantly different among the varieties, with a clear distinction due to the infection with ARSEPH. The susceptible variety exhibited an approximately 11% increase in the force required for breakage after infection. The flexural strength of tolerant variety 1 exhibited an increase of 33%, while tolerant variety 2 demonstrated an increase in flexural strength of 32%. The differences observed in the tolerant varieties were found to be statistically significant. Although data from the susceptible variety showed comparable medians across variants, substantial variability was observed in the infected plants' data. The non-infected pieces of tolerant variety 1 had a lower force requirement for breakage than those of the susceptible variety and tolerant variety 2. A significant distinction between varieties and variants in taproot piece elasticity

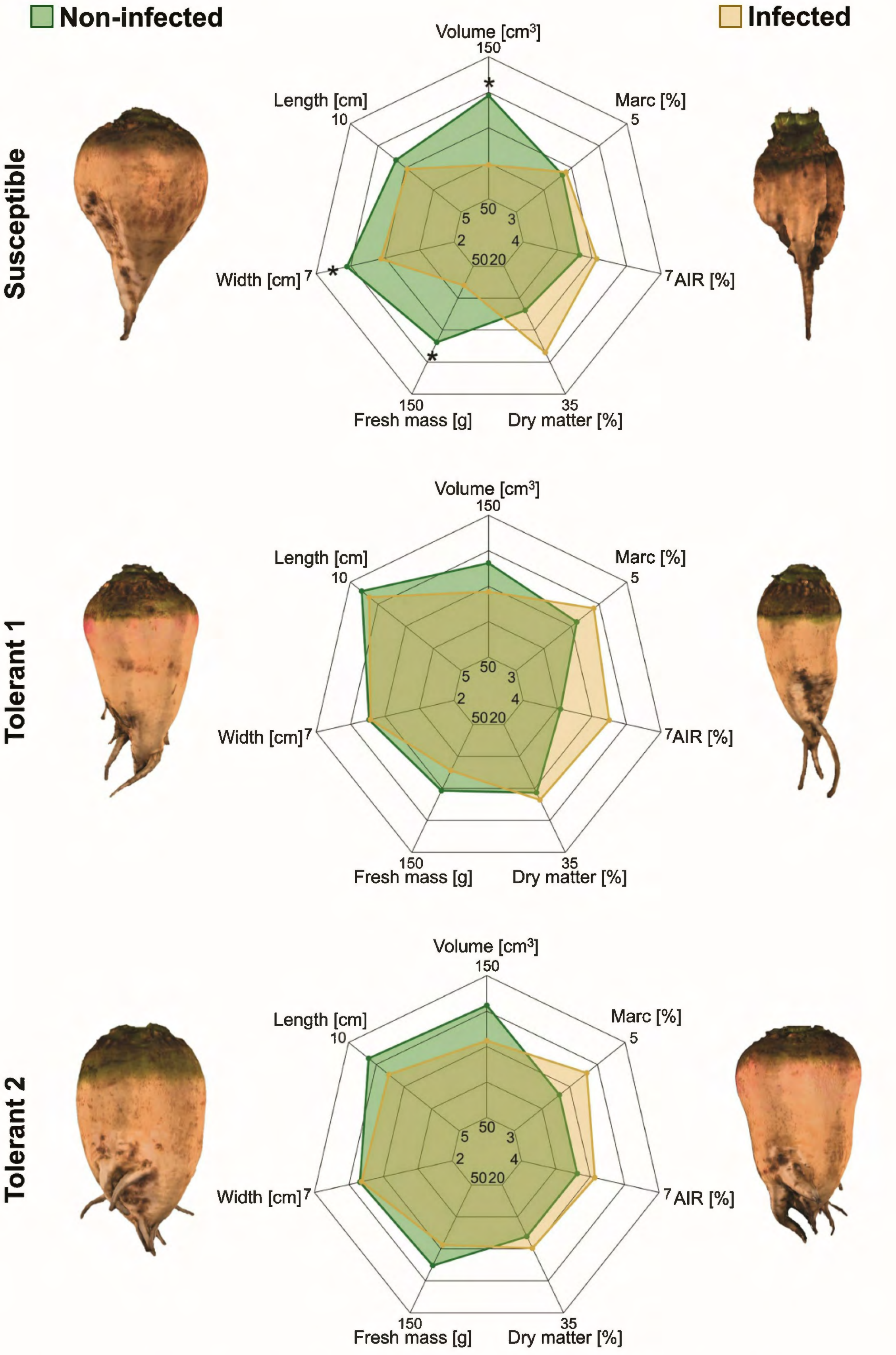

Fig. 3: Comparison of taproot parameters of *Candidatus* Arsenophonus phytopathogenicus infected and non-infected sugar beet: Volume, length, width, fresh mass, dry matter content, content of alcohol insoluble residues (AIR), and marc content at 71 days after inoculation. Significant differences between variants in a variety are marked by * at $p \leq 0.05$. The images above and below show colorized three-dimensional models of the non-infected and infected taproots.

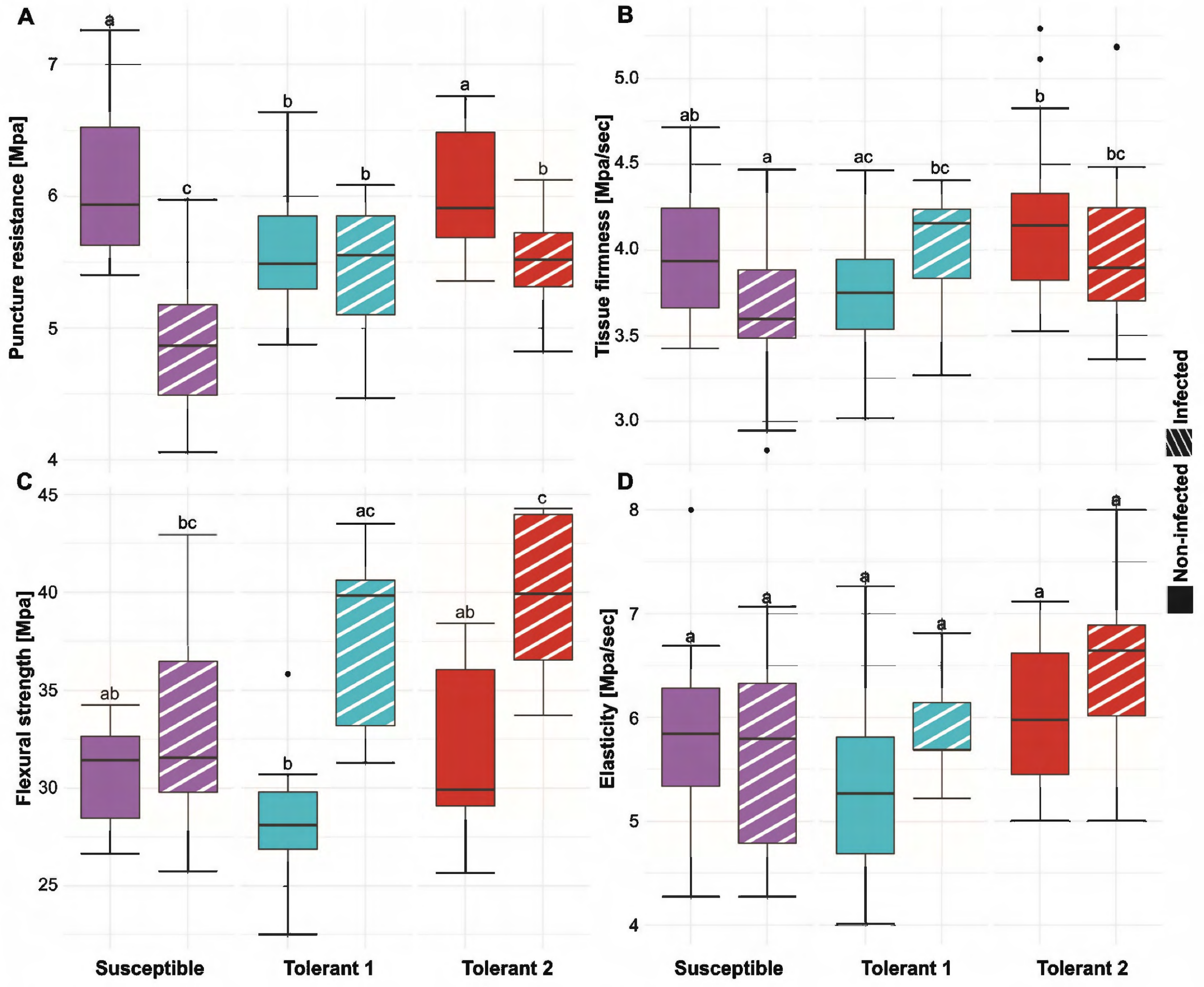

Fig. 4: Taproot texture parameters puncture resistance (A), tissue firmness (B), flexural strength (C) and elasticity (D) of *Candidatus* Arsenophonus phytopathogenicus infected and non-infected sugar beet taproots from the varieties at 71 days after inoculation. The box includes 50% of the data, line indicates the median, points show outliers; letters mark statistically significant differences between variants and varieties at $p \leq 0.05$.

was not observed, although tolerant variety 1 and tolerant variety 2 showed slightly higher elasticity after infection. Despite the presence of observable numerical disparities, the data variability within the whiskers of the boxplots corroborates the findings from the statistical analysis.

4 Discussion

The effects of the syndrome "Basses Richesses", caused by an ARSEPH infection, on the investigated morphological and physiological parameters differed between the varieties. First and foremost, the infection rate of the tolerant variety 2 was the highest at 90% of inoculated plants. In tolerant varieties, infection by a specific pathogen is possible without causing significant effects on the yield (Caldwell *et al.* 1958). Since the included varieties were tolerant, but not resistant, the infection rate cannot be the decisive parameter for variety comparison. Tolerance is supported by the non-significant differences in fresh mass, length, width, and volume of the taproot in tolerant varieties due to ARSEPH infection, indicating no significant effect on yield.

The significant reduction in those parameters in the susceptible variety caused by an ARSEPH infection may be due to alterations in plant cell walls, which have been described as lignification (Gatineau *et al.* 2002). The lignification of the cell walls has both positive and negative effects: it can hinder systemic infection by blocking the pathogen's pathways, but it can also interfere with the nutrient and water flow in the taproot which can cause negative growth effects (Ma 2024; Malavasi *et al.* 2016).

The tolerant variety 1 presented the highest, although not significant increase of AIR caused by an ARSEPH infection which might partly be caused by a plant defence induced lignification (Vance *et al.* 1980). As the amount of AIR is closely correlated with the marc content in sugar beet (Ziemiński *et al.* 2012), both parameters consistently increased after infection for all varieties. Varieties with a stronger synthesis of structural components, such as AIR and the correlated marc under pathogen attack, might have

DOI: 10.36961/si34198 | **Cite this:** *Sugar Industry 151* (2026), 60–68

an advantage in hindering the systemic infection of ARSEPH by blocking pathways that have been described for other post-harvest pathogens (Lee *et al.* 2019).

The increased marc and AIR content in all varieties after infection aligns with the increased flexural strength of infected plants. The adhesion of plant cells to one another is facilitated by the middle lamella, a pectin-rich layer that serves as an intercellular cement (Jarvis 1998). Thus, the enrichment of AIR and marc, with a particular increase in the pectin content, might be the reason for the higher tissue flexural strength. However, there were no significant differences in tissue elasticity or the time till rupture, between ARSEPH-infected and non-infected sugar beet. Hence, the tissue was not rubberier, although in practice, fields of SBR beets with double infection by ARSEPH and PHYPSO are often very rubbery. It is therefore suspected that the rubbery tissue is mainly due to PHYPSO infection, which was not possible under controlled conditions in this experiment.

Generally, ARSEPH-infected taproots of the susceptible variety show more brownish discoloration of the vascular tissue which is assumed to be lignification (Gatineau *et al.* 2002). According to this hypothesis, the most discolored variety should have the strongest tissue, which is inconsistent with the results of this research. Infection with systemic phytopathogens can lead to plant defence mechanisms such as synthesizing reactive oxygen species (ROS) to eliminate the pathogen (Dangl 2001; Morel *et al.* 1997; Torres *et al.* 2006). Besides eliminating the pathogen, ROS causes damage to plant tissue, leading to necrosis, which is visible as discolored tissue (Sullivan 2015). Thus, tolerant varieties may be able to effectively prevent the systemic infection by ARSEPH. In a susceptible variety, a systemic infection might induce further defence mechanisms such as the synthesis of polyphenol oxidases, which are toxic to pathogens but also cause oxidative stress in the plant tissue (Mayer 2006). Furthermore, the taproot shape of the susceptible variety after infection shows an irregular cambium ring distribution. This might have occurred because of a partial restriction of secondary thickening due to constraints on sugar storage. Furthermore, Agyei *et al.* (2025) showed by non-invasive MRT and PET imaging that susceptible ARSEPH infected sugar beet have significantly decreased distances between inner cambium rings.

The significant decrease in puncture resistance of the susceptible and tolerant variety 2, most likely resulted from a loss of tugor in the taproot periderm after an ARSEPH infection. Generally, all varieties showed an increased dry matter content after an ARSEPH infection accompanied by reduced water content. The following measurement of the tissue firmness below the periderm, however, showed no significant differences between infected and non-infected taproots. Plants can form new xylem elements to compensate for blocked vessels, thereby maintaining water transport to inner tissues (Mazur *et al.* 2016). To measure fundamental differences in tissue firmness affected by SBR, deeper measurements beyond 5 mm are necessary, since the pathogen propagates mostly in the centre of the taproot, as shown in Figure 2. It is thus suggested to repeat the conducted point texture measurements on cut samples from the inner part of the taproot.

5 Conclusion

The current study identified, for the first time, parameters describing the individual responses of tolerant and susceptible sugar beet varieties to SBR caused by an ARSEPH infection. A controlled infection of ARSEPH resulted in measurable effects on most of the investigated physiological and morphological parameters in the susceptible variety compared with SBR-tolerant varieties. Especially, taproot volume, width, fresh mass puncture resistance and flexural strength were affected by SBR. This response implies the opportunity to make use of those parameters for SBR tolerance variety screening under controlled conditions. The AIR and marc content are closely related, and both increased, resulting in a higher marc content after infection, especially in the tolerant varieties. If this response can be confirmed in further studies with other varieties, the analysis of the sugar beet marc content after infection could be a practical and simple method for tolerance screening, also applicable for field trials. It could also serve as an approach to estimate the mechanical robustness of plant tissue. In future, a detailed fibre analysis could be applied to get profound information about the single structural components: pectin, hemicelluloses, celluloses and lignin.

Generally, marc content, texture profile and 3D analysis provide the potential to serve as parameters for SBR tolerance screening. Further confirmation of the results is needed by testing more varieties with a higher number of repetitions. Future studies should also address individual infection with PHYPSO and mixed infection with both pathogens, ARSEPH and PHYPSO. These initial results emphasize that variety performance is a key factor in controlling SBR.

Acknowledgements

This work has been funded by the Deutsche Forschungsgemeinschaft (DFG, German Research Foundation) under Germany's Excellence Strategy–EXC 2070–390732324. The project was supported by funds of the Federal Ministry of Food and Agriculture (BMEL) based on a decision of the Parliament of the Federal Republic of Germany. The Federal Office for Agriculture and Food (BLE) provides coordinating support for artificial intelligence (AI) in agriculture as funding organization, grant number 28DK108C20. Gratitude is expressed to Anneke Lisette Eggers for her support during harvest and laboratory analysis and to Zahra Shoaei for her assistance during the molecular diagnosis process.

References

Agyei K., Detring J., Metzner R., Huber G., Pflugfelder D., Eini O., Varrelmann M., Mahlein A.-K., Koller R. (2025): Syndrome “Basses Richesses” disease induced structural deformations and sectorial distribution of photoassimilates in sugar beet taproot revealed by combined MRI-PET imaging, *Plant Phenomics 7*, 100053; DOI: https://10.1016/j.plaphe.2025.100053

Bressan A. (2009): Agronomic practices as potential sustainable options for the management of *Pentastiridius leporinus* (Hemiptera: Cixiidae) in sugar beet crops, *J. Appl. Entomol. 133*, 760–766, DOI: 10.1111/j.1439-0418.2009.01407.x

Bressan A. (2014): Emergence and evolution of *Arsenophonus* bacteria as insect-vectored plant pathogens, *Infect. Genet. and Evol. 22*, 81–90, DOI: 10.1016/j.meegid.2014.01.004

Bundessortenamt (2025): Beschreibende Sortenliste Getreide Mais Öl- und Faserpflanzen Leguminosen Rüben Zwischenfrüchte

Caldwell R., Schafer J., Compton L.E., Patterson F. (1958): Tolerance to cereal leaf rusts, *Science 128*, 714–715, DOI: 10.1126/science.128.3326.714

Ćurčić Ž., Stepanović J., Zübert C., Taški-Ajduković K., Kosovac A., Rekanović E., Kube M., Duduk B. (2021): Rubbery taproot disease of sugar beet in Serbia associated with “*Candidatus* Phytoplasma solani”, *Plant Dis. 105*, 255–263, DOI: 10.1094/PDIS-07-20-1602-RE

Dangl J.L., Jones J.D.G. (2001): Plant pathogens and integrated defence responses to infection, *Nat. 411*, 826–833, DOI: 10.1038/35081161

Detring J., Bömer J., Gupta A., Eini O., Mahlein A.-K. (2025): Phenotyping of syndrome “Basses Richesses” in sugar beet by morphological and spectral traits, *Phytopathology*, DOI: 10.1094/PHYTO-07-25-0239-R

Fisher R.A. (1919): XV.–The Correlation between Relatives on the Supposition of Mendelian Inheritance, *Trans. Roy. Soc. Edinburgh 52*, 399–433, DOI: 10.1017/S0080456800012163

Gatineau F., Jacob N., Vautrin S., Larrue J., Lherminier J., Richard-Molard M., Boudon-Padieu E. (2002): Association with the syndrome “Basses Richesses” of sugar beet of a phytoplasma and a bacterium-like organism transmitted by a *Pentastiridius sp.*, *Phytopathology 92*, 384–392, DOI: 10.1094/PHYTO.2002.92.4.384

Hoffmann C.M., Leijdekkers M., Ekelöf J., Vancutsem F. (2018): Patterns for improved storability of sugar beet – importance of marc content and damage susceptibility of varieties in different environments, *Eur. J. of Agron. 101*, 30–37, DOI: 10.1016/j.eja.2018.08.004

Jarvis M.C. (1998): Intercellular separation forces generated by intracellular pressure, *Plant, Cell and Environ. 21*, 1307–1310, DOI: 10.1046/j.1365-3040.1998.00363.x

Kleuker G., Hoffmann C.M. (2019): Method development for the determination of textural properties of sugar beet roots, *Sugar Industry 144*, 392–400, DOI: 10.36961/si23306

Kleuker G., Hoffmann C.M. (2021): Tissue strength of sugar beet root genotypic variation and environmental impact, *Crop Sci. 61*, 2478–2488, DOI: 10.1002/csc2.20523

Kleuker G., Hoffmann C.M. (2022): Causes of different tissue strength, changes during storage and effect on the storability of sugar beet genotypes, *Postharvest Biol. Technol. 183*, 111744, DOI: 10.1016/j.postharvbio.2021.111744

Lang C., Dettweiler A., Benaouda S., Kreimer D., Löffler D., Glaser E., Adam H., Bojanowicz S.L., Schall E., Stohl J., Göbbels H., Lenz M., Witczak N., Ritz J., Pfitzner H. (2025): *Pentastiridius leporinus* as a plant disease vector: The practical state of knowlege and derived research objectives, *Sugar Industry 150*, 105–120, DOI: 10.36961/si33023

Lee M.-H., Jeon H.S., Kim S.H., Chung J.H., Roppolo D., Lee H.-J., Cho H.J., Tobimatsu Y., Ralph J., Park O.K. (2019): Lignin-based barrier restricts pathogens to the infection site and confers resistance in plants, *EMBO J. 38*, e101948, DOI: 10.15252/embj.2019101948

Levene H. (1960): Robust tests for equality of variances, *Cont. Prob. Stat.*, 278–292

Ma Q.H. (2024): Lignin biosynthesis and its diversified roles in disease resistance, *Genes 15*, 295, DOI: 10.3390/genes15030295

Malavasi U.C., Davis A.S., Malavasi M. (2016): Lignin in woody plants under water stress: A review, *Floresta Ambiente 23*, 589–597, DOI: 10.1590/2179-8087.143715

Mayer A.M. (2006): Polyphenol oxidases in plants and fungi: Going places? A review, *Phytochemistry 67*, 2318–2331, DOI 10.1016/j.phytochem.2006.08.006

Mazur E., Benková E., Friml J. (2016): Vascular cambium regeneration and vessel formation in wounded inflorescence stems of *Arabidopsis*, *Sci. Rep. 6*, 33754, DOI: 10.1038/srep33754

McFeeters R., Armstrong S. (1984): Measurement of pectin methylation in plant cell walls, *Anal. Biochem. 139*, 212–217, DOI: 10.1016/0003-2697(84)90407-X

Morel J.-B., Dangl J.L. (1997): The hypersensitive response and the induction of cell death in plants, *Cell Death Differ. 4*, 671–683, DOI: 10.1038/sj.cdd.4400309

Morkunas I., Ratajczak L. (2014): The role of sugar signaling in plant defense responses against fungal pathogens, Acta Physiol. *Plant. 36*, 1607–1619, DOI: 10.1007/s11738-014-1559-z

Nause N., Meier T., Hoffmann C.M. (2020): Tissue composition and arrangement in sugar beet genotypes of different tissue strength with regard to damage and pathogen infestation, *Sugar Industry 145*, 114–123, DOI: 10.36961/si24063

Pfitzer R., Rostás M., Häußermann P., Häuser T., Rinklef A., Detring J., Schrameyer K., Voegele R.T., Maier J., Varrelmann M. (2024): Effects of succession crops and soil tillage on suppressing the syndrome ‘Basses Richesses’ vector *Pentastiridius leporinus* in sugar beet, *Pest Manag. Sci 80*, 3379–3388, DOI: 10.1002/ps.8041

Pfitzer R., Varrelmann M., Schrameyer K., Rostás M. (2022): Life history traits and a method for continuous mass rearing of the planthopper *Pentastiridius leporinus*, a vector of the causal agent of syndrome ‘Basses Richesses’ in sugar beet, *Pest Manag. Sci. 78*, 4700–4708, DOI: 10.1002/ps.7090

Reinefeld E., Schneider F. (1983): *Analytische Betriebskontrolle der Zuckerindustrie – Teil B: Vorschriften für die Betriebskontrolle, 2.2.1.5*, Verlag Dr. Albert Bartens, Berlin

Schnepel K., Hoffmann C.M. (2016): Genotypic differences in storage losses of sugar beet – causes and indirect criteria for selection, *Plant Breed. 135*, 130–137, DOI: 10.1111/pbr.12338

Shapiro S.S., Francia R.S. (1972): An approximate analysis of variance test for normality, *J. Am. Stat. Assoc. 67*, 215–216, DOI: 10.1080/01621459.1972.10481232

Smith A.H., Gill W.M., Pinkard E.A., Mohammed C.L. (2007): Anatomical and histochemical defence responses induced in juvenile leaves of *Eucalyptus globulus* and *Eucalyptus nitens* by *Mycosphaerella* infection, *For. Pathol. 37*, 361–373, DOI: 10.1111/j.1439-0329.2007.00502.x

Storck V., Karpouzas D.G., Martin-Laurent F. (2012): Towards a better pesticide policy for the European Union, *Sci. Total. Environ. 575*, 1027–1033, DOI: 10.1016/j.scitotenv.2016.09.167

Sullivan M.L. (2015): Beyond brown: Polyphenol oxidases as enzymes of plant specialized metabolism, *Front. in Plant Sci. 5*, DOI: 10.3389/fpls.2014.00783

Torres M.A., Jones J.D.G., Dangl J.L. (2006): Reactive oxygen species signaling in response to pathogens, *Plant Physiol. 141*, 373–378, DOI: 10.1104/pp.106.079467

Tukey J.W. (1949): Comparing individual means in the analysis of variance, *Biometrics 5*, PMID:18151955

Vance C.P., Kirk T.K., Sherwood R.T. (1980): Lignification as a mechanism of disease resistance, *Annu. Rev. Phytopathol. 18*, 259–288, DOI: 10.1146/annurev.py.18.090180.001355

Werner E. (1966): *Zuckertechniker Taschenbuch*, Verlag Dr. Albert Bartens, Berlin

Ziemiński K., Romanowska I., Kowalska M. (2012): Enzymatic pretreatment of lignocellulosic wastes to improve biogas production, *Waste Manag. 32*, 1131–1137, DOI: 10.1016/j.wasman.2012.01.016

Zübert C., Kube M. (2021): Application of TaqMan real-time PCR for detecting ‘*Candidatus* Arsenophonus phytopathogenicus’ infection in sugar beet, *Pathogens 10*, DOI: 10.3390/pathogens10111466

CHAPTER 6: General discussion

This thesis characterized the syndrome “Basses Richesses” of sugar beet with different phenotyping approaches and demonstrated the relevance of the collected parameters for comparing different sugar beet varieties in terms of their tolerance levels to SBR (Figure 1).

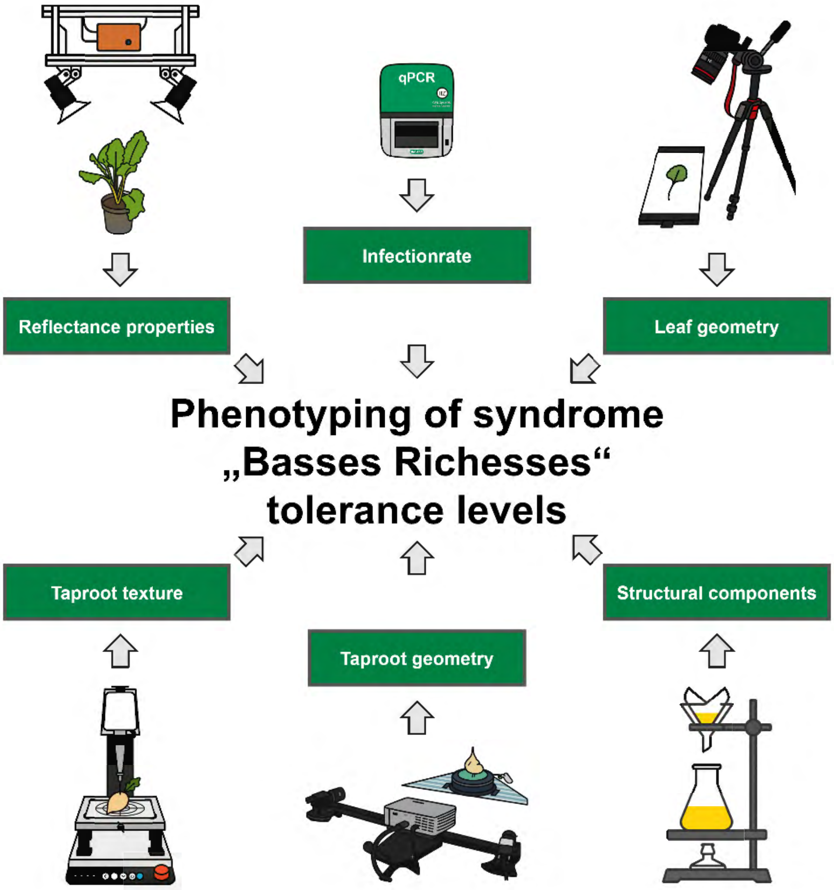

Figure 1: Phenotyping routines for comparing variety-specific tolerance levels to syndrome “Basses Richesses”. Top row (from left to right): Hyperspectral imaging, quantitative polymerase chain reaction and two-dimensional measuring of leaves. Bottom row (from left to right): Texture profile analysis, three-dimensional scanning and structural components analysis.

Especially spectral characterization of the SBR pathogenesis in time series is one of the main objectives of this thesis described in Chapter 4. The fundament for such a characterization is a spectral data set of high quality. Therefore, a sophisticated measuring set up had to be practically established. The establishment of this set up was based on the findings described in Chapter 3 which connects the method development in Chapter 3 and application on a phytopathological use case in Chapter 4. Additionally, robust infection protocols with the complex SBR-pathosystem were accomplished to secure comparability of experimental repetitions and by this variety performance. In this infection protocol, only ARSEPH could be considered. The symptoms caused by a single infection with PHYPSO and mixed infection (ARSEPH, PHYPSO) need to be investigated with the proposed methods. Furthermore, advanced data processing and analyzation pipelines were established to handle complex data sets which have been demonstrated in Chapter 3 and applied in Chapter 4. To contextualize the phenotypic findings of Chapter 4 in the host-pathogen interaction, physiological analyses of different parameters were conducted in Chapter 5. Hypotheses on the connection between physiological alterations and the phenotypic outcomes can be drawn from these results, as the basis for further research. The proposed methods can be integrated into a greenhouse high-throughput variety screening for SBR-tolerance, either partially or in their entirety. In order to ensure the efficacy of the proposed parameters for screening under field conditions, it is essential to investigate their stability in open environments. However, in the context of field high-throughput HSI, there is an absence of robust measurement HSI-methods for validating the spectral characterization. This suggests the preliminary validation of the parameters in the field by targeted non-imaging hyperspectral measurements.

6.1 Hyperspectral imaging in plant phenotyping

Hyperspectral imaging in plant phenotyping for phytopathological use cases faces several obstacles which have been addressed in Chapter 3 of this thesis. Consequently, the establishment of high-quality data sets, which are essential for accurate spectral characterization of plant diseases, poses significant challenges. First and foremost, the results need to be solely associated with the targeted disease. Controlled environments provide the circumstances to prevent stress any other than the desired. Nevertheless, even in controlled measurement conditions, there are several technical factors that must be taken into consideration to ensure the attainment of high-quality measurements. As stated in Chapter 3 of this thesis, the selection of the hyperspectral imaging system is of paramount importance when it comes to ensuring the integrity of the resulting data. Furthermore, the findings in Chapter 3 demonstrate that the type and angle of artificial illumination can exert a substantial influence on hyperspectral measurements which correspond to the findings of Behmann et al. (2015) and Bousquet et al. (2005). Bousquet et al. (2005) showed that the leaf Bidirectional Reflectance Distribution Function (BRDF) is influenced by the illumination angle for non-imaging hyperspectral measurements. Chapter 3 lends further support and an extension to these findings by demonstrating that a 90° illumination angle engenders mirroring effects in hyperspectral images of leaves. This issue can be addressed in HSI by adjusting the angle and avoiding direct illumination with diffusive screens in front of the illumination source as demonstrated in Chapter 3.

In the pursuit of optimal spectral signal-to-noise (SNR) ratio in HSI, meticulous adjustment of all technical factors is important. SNR is a measure that compares the level of desired signal to the level of noise (Welvaert et al. 2013). The measurement method and object of interest define the type of desired signal. In HSI for plant phenotyping, the reflectance of the plant surface is regarded as the desired signal. The potential for noise occurrence in this scenario is multifaceted, arising from various factors. In addition to the HSI-system's inherent technical noise, which can be mitigated by incorporating the system's dark current into the radiometric normalization process, illumination in correspondence with the plant geometry and atmospheric effects influence the quality of HSI (Behmann et al. 2015; Griffin et al. 2003).

The importance of illumination in HSI-setups has been broadly investigated and discussed in this thesis. Radiometric correction of 3D-objects in 2D-HSI is a research topic on its own (Behmann et al. 2015), as well as the influence of the atmosphere on HSI (Griffin et al. 2003). Radiative transfer modeling (RTM) offers the opportunity for atmospheric correction in HSI (Verhoef et al. 2003; Vermote et al. 1996). In RTM sensor altitude, solar angle, visibility, aerosol type, water vapor ozone etc., are taken into consideration for correcting the signal to receive the real surface reflectance (Gao et al. 2009). After the Beer-Lambert law, which describes the loss of light intensity after travelling through a medium, the influence of the atmosphere on hyperspectral measurements decreases with the measurement distance but are never zero (Ihalainen et al. 2024; Mayerhöfer et al. 2020). Nevertheless, the discrepancy in the measurements of the reference material obtained, using the spectroradiometer and the hyperspectral camera in Chapter 3, is most likely attributable to technical variations in the measurement systems rather than the atmospheric effects. The plant probe attachment of the spectroradiometer is applied directly onto the leaf, thereby decreasing the atmospheric space. The hyperspectral camera operated in a 50-centimeter distance, thereby allowing for greater atmospheric space. However, the influence of the atmosphere on close range HSI in the VIS and NIR for plant phenotyping is mostly neglected in literature (Mahlein et al. 2018; Mishra et al. 2017).

As discussed before, for long range hyperspectral measurements RTM is used for correcting the atmospheric influence in the hyperspectral signal, but radiative transfer models do not account for 3D-effects which occur on plant measurements in controlled and uncontrolled conditions. Two-dimensional radiometric normalization of hyperspectral images picturing 3D-objects is still the state of the art in plant phenotyping (Paulus et al. 2020). This method cannot picture the correct spectral signature of every part of the leaf or plant canopy which produces noise in the hyperspectral imaging data (Behmann et al. 2015). Smoothing is an essential pre-processing step for HSI-data to decrease noise and increase the signal-to-noise ratio (SNR). The Savitzky-Golay filter is a standard technique for smoothing in HSI (Mahlein et al. 2012; Mishra et al. 2017). The noise is reduced by considering a small set of points around the wavelength and fits a smooth curve through those points. As a result, the noisy center point is replaced with the value from that fitted curve (Savitzky et al. 1964). Additionally, some HSI-systems offer the option of spectral and spatial binning. Spectral binning combines the adjacent spectral bands. Depending on the degree of spectral binning 2, 4 or even more bands are binned reducing the amount of spectral information which may increase the SNR (Jablonski et al. 2016). Thus, spectral binning might help to reduce the noise in HSI-data when 3D-objects are considered. Spatial binning combines the signal of neighboring image pixels into one single signal. Similar to spectral binning, the higher the degree of binning, the more pixels are combined. Thus, spatial binning can increase the SNR as well but results in a loss of spatial resolution (Paulus et al. 2020). It highly depends on the phenotyping task whether high spectral or high spatial resolution is aimed at in HSI. Technically both can be achieved in close range HSI but practically when fast acquisition speed and reduced data volume is targeted, high spatial resolution should be prioritized in plant phenotyping. This is primarily because, at some point, the increase in spectral resolution surpasses the improvement of HSI with relevant spectral data due to the high correlation of neighboring wavelengths (Li et al. 2014). Furthermore, high spatial resolution is needed for precise segmentation tasks in HSI demonstrated in Chapter 3 and 4.

However, Chapter 3 underlines the importance of high-quality HSI-data for phytopathological plant phenotyping. In this chapter, the foundation for the subsequent exploration of sophisticated hyperspectral imaging techniques within the scope of this thesis is established. The importance of high-quality HSI-data is particularly pronounced in the context of systemic diseases such as SBR where the absence of discernible symptoms in the spatial dimension necessitates a comprehensive measurement and analysis of the plant.

6.2 Combining multifactorial phenotyping results for syndrome “Basses Richesses” tolerance variety screening

SBR has been spectrally and morphologically characterized in Chapter 4 of this thesis. Therefore, a robust infection procedure has been established under controlled conditions to assess high quality hyperspectral data of the sugar beet canopy, which is based on the findings of Chapter 3. To analyze the canopy organs individually, a ResNet18-encoded U-Net (He et al. 2016; Ronneberger et al. 2015) was fine-tuned to segment hyperspectral images into background, taproot, crown, leaves and petioles. ResNet-18 provides deep hierarchical features that capture textures and semantics and has compact architecture for fast training (Peng et al. 2025). Additionally, ResNet-18 is broadly available with pretrained weights resulting in a better generalization of the individual finetuned models. However, ResNet alone provides downscaled, low resolution feature maps which are restored in spatial resolution by U-Net which provides detailed segmentations (Gkologkinas et al. 2025; Ronneberger et al. 2015). The highly accurate segmentations between canopy organs enabled an organ-specific analysis of the reflectance properties affected by SBR. Generally, plant organ-specific analysis of the reflectance properties is necessary for certain use cases but insufficiently implemented in HSI for plant phenotyping (Nethala et al. 2024) especially in the field of phytopathology (Mahlein et al. 2019).

This thesis introduces a novel application of canopy-organ-specific analysis of reflection properties for a phytopathological use case in sugar beets, based on hyperspectral images. In this approach, the hyperspectral information underwent a preliminary categorization based on the pronounced physiological differences between leaves and petioles. The necessity of this approach is underlined by the results which show a significant higher accuracy in disease classification based on the hyperspectral information from the petioles. Moreover, this approach facilitated the interpretability of the ML outcomes, which is pertinent for both biological and physiological interpretation. In addition, the results obtained can be linked to localized molecular diagnostics of ARSEPH. These diagnostics have demonstrated a higher pathogen prevalence in petioles compared to the leaves (Mahillon et al. 2022) which indicates a plant response to the pathogen, because otherwise the immobile bacteria would be transported via the phloem stream to the taproot. This underscores the necessity of attaining a more profound comprehension of the plant and pathosystem to facilitate the execution of machine-driven data analysis, thereby ensuring the attainment of both rational and practical outcomes.

Supervised ML pattern recognition is predicated on the references provided during the training process (Liakos et al. 2018). Model performance is therefore dependent on the detailedness and precision of the reference data. Considering the entire canopy during the training process in Chapter 4 would have blurred the results. For spatially localizable symptoms of e.g. foliar diseases, standard area diagrams are used by raters to estimate the current disease damage in percent (Bock et al. 2020). Systemic diseases need qualitative ordinal scales based on certain descriptions of symptoms to categorize the disease severity by raters (Bock et al. 2020). In Chapter 4, all petioles or leaves were considered diseased if one leave or petiole presented distinct symptoms. Agyei and Detring et al. (2025) demonstrated that SBR can exert a limited effect on the taproot vascular system during disease development. In the event of this occurrence, it is possible that only the leaves and petioles will exhibit symptoms which are connected to infected taproot tissue. Accordingly, the meticulous examination of individual leaves and petioles within a time series has the potential to enhance the precision of disease classification. Additionally, this approach facilitates the estimation of SBR disease severity by quantifying the symptomatic leaves and petioles over the sugar beet canopy. Therefore, a hyperspectral image segmentation would need to go beyond semantics and provide single instances. Prominent instance segmentation models, such as SAM or Mask R-CNN, have been demonstrated to possess the capacity of finetuning for such specific use cases (Archit et al. 2025; Triki et al. 2021).

SBR does not only affect the sugar beet canopy in its phenotypic outcome as described in Chapter 4. Additionally, morphological changes have been described and parametrized based on taproot 3D-scanning. Invasive 3D-scanning of the taproot is a valuable method for describing the effects of SBR on the taproot morphology. Moreover, when geometric parameters such as volume, length and width are derived, the effects of variety-specific factors of SBR on the taproot geometry can be quantified (Chapter 5). Determining the variety-specific effects of SBR on taproot geometry presents the possibility of screening varieties for SBR-tolerance. As 3D-scanning of the taproot is an invasive method, it was always implemented at the end of the experiments in this thesis. The aim was to keep the number of technical repetitions high to enable robust conclusions from data analysis. In theory, 3D-scanning could be applied in a time series to find the earliest timepoint for meaningful variety comparison. Agyei and Detring et al. (2025) showed significant differences in volume between ARESEPH-infected and non-infected sugar beets by non-invasive magnetic resonance imaging 49 days after inoculation and for cambium ring width already 42 days after inoculation. Magnetic resonance imaging facilitates precise measurements for the fundamental understanding of the plant disease effects but lack of practicability for high-throughput screening due to high costs and low measurement throughput. However, the practicability of invasive 3D-scanning for below ground plant phenotyping has been demonstrated (Esser et al. 2023, 2024; Paulus 2019; Paulus et al. 2014a, 2014b). Geometric parameters, including taproot volume, width, and length, exhibit a strong correlation with yield. This suggests the potential for SBR to exert an effect on yield during the later stages of the vegetation period. Nevertheless, morphological parameters are more sensitive shown in Chapter 4. Already small variances in morphological parameters present an impact on the performance of the Boruta model. The analysis of the parameters with Boruta and SHAP revealed the most sensitive to SBR. Based on this finding, parameters can be selected and thresholds set for SBR-tolerance variety screening which needs to be tested on varieties with different tolerance levels to SBR.

Furthermore, Chapter 4 delineates the assessment of additional geometric parameters of the sugar beet leaves. In addition to the impact of SBR on the reflectance properties of leaves, the disease also exerts a substantial influence on various aspects of leaf morphology, including leaf area, length, blade length and blade width. A correlation has been demonstrated between the shape of sugar beet leaves and their leaf area (Tsialtas et al. 2007). Furthermore, an association has been observed between leaf area and sugar beet yield (Tsialtas et al. 2014). Consequently, varieties exhibiting a substantial decrease in leaf parameters may also undergo a notable alteration in yield. Phytopathogens infesting the vascular system of plants are known to affect both source and sink organs (Haider et al. 2024). It is assumed that the ARSEPH-induced changes of the sugar beet canopy are followed by the alteration of the taproot vascular system, but detailed host-pathogen interactions are still to be determined.

6.3 Syndrome “Basses Richesses” host-pathogen interaction

In Chapter 5 of this thesis, the effects of an ARSEPH-infection on the taproot structural and textural characteristics of three sugar beet varieties are investigated. Significant effects on the puncture resistance of the susceptible and flexural strength of the tolerant varieties could be described. The increased flexural strength of the tolerant varieties can be connected to the increased contents of structural components marc and AIR. Gatineau et al. (2002) described SBR-induced lignification of the phloem cell walls by autofluorescence and by phloroglucinol or Mirande's green staining but never quantified its amount. Since then, the visible brownish discoloration of the vascular tissue was considered as lignification. This opposes the findings of Chapter 5, because following this theory taproots with increased discoloration should have an increased content of structural components and increased tissue strength. Based on the findings of Chapter 5 it is questionable if the brownish discoloration is visible lignification. Lignin in its natural form is colorless (Zheng et al. 2023) and depending on its concentration and amount of free phenolic hydroxyl groups it appears dark brown (Mota et al. 2023). Furthermore, increased lignin content causes higher tissue strength (Barros et al. 2015). If the visible brownish discoloration would be really lignin as described by Gatineau et al. (2002), susceptible varieties which show a greater brownish discoloration should consequently have a greater flexural strength (Yang et al. 2018). In fact, susceptible varieties have decreased flexural strength (Chapter 5).

Agyei and Detring et al. (2025) showed a complete disruption of the photoassimilate transportation in ARSEPH-infected sugar beet tissue. Lignification of the cell walls as a plant defense mechanism to pathogen attacks is not associated with complete rupture of the vascular system but reinforcing physical barriers to hinder a systemic spread (Morkunas et al. 2014; Smith et al. 2007; Tiwari et al. 2025). The possibility that toxins produced by bacteria caused this damage is unlikely because bacterial titers are very low in infected plant tissue (personal communication). Thus, other plant defense mechanisms with more self-destructive traits must be responsible for the rupture of the vascular system. Hypersensitive response (HR) is a pathogen-induced areal cell death of plant tissue to stop systemic infections (Balint-Kurti 2019). In HR, reactive oxygen species (ROS) are produced, which are toxic to the pathogen and the plant. This phenomenon consequently results in plant tissue necrosis. SBR-induced taproot tissue necrosis was also described by Gatineau et al. (2002) as a result to an ARSEPH-infection and aligns with the reduced flexural strength and rupture of the vascular system. It is therefore hypothesized that the visible brownish discoloration is tissue necrosis rather than visible lignification. The initial cause of this necrosis demands further investigation. Nonetheless, the hypothesis that lignification, in conjunction with the augmentation of other structural elements, serves as a trait responsible for tolerance to an ARSEPH-infection is substantiated by the findings presented in Chapter 5 of this thesis and corroborated by extant literature (Vance et al. 1980). Besides hindering a systemic infection, lignification of the phloem can also interfere with nutrient supply between sink and source in sugar beet (Ma 2024; Malavasi et al. 2016). SBR-induced insufficient and imbalanced nutrition of the canopy might be an additional reason for the SBR leaf symptom development. This underscores the necessity of a thorough investigation of a pathosystem to elucidate the phenotype of a particular disease.

However, the reinforcement of cell walls with structural components has been identified as a defense response that hinders systemic infection in other phloem-colonizing phytobacteria (Dittmer et al. 2021; Koh et al. 2012). *Candidatus* Liberibacter asiaticus, the causal agent of Huanglongbing in citrus trees and *Candidatus* Phlomobacter fragariae, the causal agent of Strawberry marginal chlorosis, are two examples of other phloem-limited proteobacteria (Bressan 2014). These organisms induce the blocking of the phloem sieve tubes by callose deposition (Dittmer et al. 2021; Koh et al. 2012). Callose is a linear plant polysaccharide that is synthesized in plants in response to various environmental stresses (Piršelová et al. 2013). Furthermore, the synthesis of callose has been demonstrated to provide mechanical support (Piršelová et al. 2013). Therefore, it can be hypothesized that callose may also play a role in the defense of sugar beet plants against SBR, a subject that has yet to be investigated.

This thesis delineates a comprehensive characterization of SBR symptoms through the utilization of high-precision digital phenotyping methods. These results are then contextualized with physiological analyses and molecular diagnostics. This characterization provides a foundation for the assessment of SBR-tolerance levels across different sugar beet varieties. Nonetheless, it has become evident that further research is required to achieve a holistic understanding of the subject matter.

6.4 Further challenges and future perspectives

A comprehensive approach to understand the pathogenesis of SBR is presented in this thesis which involves the integration of high-precision digital phenotyping methods, such as HSI or 3D-scanning, with physiological analysis and molecular diagnostics. This approach is further enhanced by sophisticated ML-driven data analysis, resulting in a multifaceted characterization of the disease's pathophysiology. Nevertheless, further research is necessary to improve the processing of HSI-data and verify the textural and physiological alterations induced by SBR for the purpose of practical screening of sugar beet varieties.

As discussed in Chapters 3, 4 and 6 of this thesis, the significance of HSI-data quality in ensuring the accuracy of data analysis conclusions has been thoroughly examined. Nevertheless, further research is needed to improve HSI quality for plant phenotyping. The implementation of 2D radiometric normalization on 3D plant models introduces noise into the resulting data (Behmann et al. 2015). The introduction of the third dimension to radiometric normalization has been demonstrated to effectively address several data noise issues, including surface orientation to illumination, distance-based illumination falloff, shadow and occlusion detection (Behmann et al. 2015). Furthermore, BRDFs could be employed to derive more precise surface reflectance (Bousquet et al. 2005). In practice, the implementation of depth-sensing methods entails the integration of stereo vision cameras within the HSI-system, thereby facilitating the acquisition of a depth image concomitant with each hyperspectral image (Kazmi et al. 2014). This approach enables the derivation of a plant 3D-model for correct 3D radiometric normalization of hyperspectral images.

Especially systemic diseases such as SBR, which cannot be categorized in linear standard area diagrams for diseases damage estimation (Bock et al. 2020), need precise measurements to enable robust data analysis for estimating disease incidence and severity. The determination of SBR disease incidence in controlled environments based on the reflectance properties of sugar beet petioles has been described in Chapter 4. If the estimation of the disease incidence by the provided method is generalized and robust under field conditions, it could support the monitoring of SBR caused by single infection of ARSEPH. However, due to the late appearance of symptoms in the field, it is not suitable for decision support in plant protection during the vegetation. A determination of the disease severity would further support HSI based SBR-tolerance variety screening which can be established based on the findings of this thesis. The hyperspectral characterization of SBR-induced alterations can be used to establish a disease classification on single instances of leaves and petioles, respectively. If single leaves and petioles are considered high quality and accurate HSI-data is even more important. Moreover, fine alterations of the reflectance properties, especially from petioles caused by SBR, need high precision measurements. High precision HSI of SBR under controlled conditions has been established in this thesis. If in-field HSI is desired, several other factors need to be considered such as intensity and incidence of solar radiation, wind, or the soil in the background (Benelli et al. 2020).

To establish a robust SBR disease detection, the separability of the described hyperspectral SBR-characteristics in Chapter 4 needs to be tested in a multi-stress environment. Additionally, high-throughput and high resolution HSI under field conditions is a research field on its own and has not been established for broader use yet (Benelli et al. 2020). But the description of the most important organs for disease classification outlined in Chapter 4 might have made spatial information redundant. Hyperspectral non-imaging point measurements of the sugar beet petiole for SBR disease classification might be sufficient for disease classification under controlled and uncontrolled conditions.

Nonetheless, the data quality of invasive phenotyping methods, such as 2D- and 3D-scanning and texture analysis of the belowground taproot, is less vulnerable to trials conducted under uncontrolled conditions than HSI. Thus, the established workflow in this thesis for such methods can be easily applied to sugar beet grown under field conditions and for other phytopathological use cases. However, the description of the geometric and morphological parameters in Chapters 4 and 5 need to be tested for its robustness in variety screening. Additionally, the findings of Chapter 5 on the SBR-induced alterations of taproot structural components need to be verified. The hypothesized SBR-induced HR and the possible production of ROS could be tested by diaminobenzidine staining of ARSEPH-infected taproot tissue (Abrahamson 2023) which has not been investigated yet in literature. If SBR-induced increases in structural components are confirmed to be variety-specific tolerance traits, physiological analyses, such as AIR and marc content, can be seamlessly employed for greenhouse and field SBR-tolerance variety screening. Marc content is particularly advantageous as it is an environmentally stable variety trait (Hoffmann et al. 2018).

The main focus of this thesis is the characterization of ARSEPH-induced phenotypical changes in sugar beet. *Candidatus* Arsenophonus phytopathogenicus has been the dominant causal agent of SBR in the last 30 years (Agyei et al. 2025; Kais et al. 2023; Mahillon et al. 2022; Pfitzer et al. 2024; Salar et al. 2010; Sémétey et al. 2007a; Zübert et al. 2021). Recently, the second pathogen associated with SBR, PHYPSO, which had previously played a minor role in the SBR-pathosystem, became highly relevant due to its extreme increase in abundance, particularly in Germany and Austria (Kreitzer et al. 2025; Lang et al. 2025). This resulted in a shift of SBR symptoms if mixed infections with similar titer of ARSEPH and PHYPSO or single infections with PHYPSO occur. Therefore, to attain a holistic phenotypic characterization of the pathosystem SBR, it is imperative to examine the impact of mixed and single infections on the manifestation of symptoms in sugar beet.

The presented phenotyping routines in this thesis combined with sophisticated ML-data analysis provide the potential to achieve a holistic phenotypic characterization of the pathosystem SBR. Subsequently, this phenotypic characterization could be utilized for SBR-tolerance screening for either PHYPSO or ARSEPH. For now, the achieved results on the single infection with ARSEPH are applicable for tolerance screening under controlled conditions. By presenting increased deposition of structural plant tissue components as a possible tolerance trait against ARSEPH-infections, this thesis revealed new insights in the host-pathogen interaction of ARSEPH and sugar beet which are the fundament for further research on this topic. This thesis achieved a comprehensive characterization of ARSEPH-induced SBR symptoms by establishing digital phenotyping routines which can be incorporated in a screening for assessing SBR-tolerance levels of different sugar beet varieties under controlled conditions.

CHAPTER 7: References

Abrahamson, D. R. 2023. The Graham and Karnovsky horseradish peroxidase ultrastructural method: A premier JHC citation classic. J Histochem Cytochem 71:43–45. https://doi.org/10.1369/00221554221146838.

Agyei, K., Detring, J., Metzner, R., Huber, G., Pflugfelder, D., Eini, O., Varrelmann, M., Mahlein, A.-K. and Koller, R. 2025. Syndrome “Basses Richesses” disease induced structural deformations and sectorial distribution of photoassimilates in sugar beet taproot revealed by combined MRI-PET imaging. Plant Phenomics 7:100053. https://doi.org/https://doi.org/10.1016/j.plaphe.2025.100053.

Altermatt, F. 2010. Climatic warming increases voltinism in European butterflies and moths. Proc Biol Sci 277:1281–1287. https://doi.org/10.1098/rspb.2009.1910.

Archit, A., Freckmann, L., Nair, S., Khalid, N., Hilt, P., Rajashekar, V., Freitag, M., Teuber, C., Buckley, G., von Haaren, S., Gupta, S., Dengel, A., Ahmed, S. and Pape, C. 2025. Segment Anything for microscopy. Nat Methods 22:579–591. https://doi.org/10.1038/s41592-024-02580-4.

Balint-Kurti, P. 2019. The plant hypersensitive response: concepts, control and consequences. Mol Plant Pathol 20:1163–1178. https://doi.org/10.1111/mpp.12821.

Barreto, A., Paulus, S., Varrelmann, M. and Mahlein, A.-K. 2020. Hyperspectral imaging of symptoms induced by *Rhizoctonia solani* in sugar beet: comparison of input data and different machine learning algorithms. J Plant Dis Prot 127:441–451. https://doi.org/10.1007/s41348-020-00344-8.

Barreto, A., Reifenrath, L., Vogg, R., Sinz, F. and Mahlein, A.-K. 2023. Data augmentation for mask-based leaf segmentation of UAV-Images as a basis to extract leaf-based phenotyping parameters. KI – Künstl Intell 37:143–156. https://doi.org/10.1007/s13218-023-00815-8.

Barros, J., Serk, H., Granlund, I. and Pesquet, E. 2015. The cell biology of lignification in higher plants. Ann Bot 115:1053–1074. https://doi.org/10.1093/aob/mcv046.

Baumann, P., Moran, N. and Baumann, L. 2006. Bacteriocyte-associated endosymbionts of insects. In: Dworkin, M., Falkow, S., Rosenberg, E., Schleifer, KH., Stackebrandt, E. (eds) The Prokaryotes, Springer, New York. https://doi.org/10.1007/0-387-30741-9_16.

Bažok, R., Lemić, D., Chiarini, F. and Furlan, L. 2021. Western corn rootworm (*Diabrotica virgifera virgifera* LeConte) in Europe: Current status and sustainable pest management. Insects 12:195. https://doi.org/10.3390/insects12030195.

Behmann, J., Acebron, K., Emin, D., Bennertz, S., Matsubara, S., Thomas, S., Bohnenkamp, D., Kuska, M. T., Jussila, J., Salo, H., Mahlein, A.-K. and Rascher, U. 2018. Specim IQ: Evaluation of a new, miniaturized handheld hyperspectral camera and its application for plant phenotyping and disease detection. Sensors 18:441. https://doi.org/10.3390/s18020441.

Behmann, J., Mahlein, A.-K., Paulus, S., Kuhlmann, H., Oerke, E. C. and Plümer, L. 2015. Calibration of hyperspectral close-range pushbroom cameras for plant phenotyping. ISPRS J Photogramm Remote Sen 106:172–182. https://doi.org/10.1016/j.isprsjprs.2015.05.010.

Behrmann, S. C., Rinklef, A., Lang, C., Vilcinskas, A. and Lee, K. Z. 2023. Potato (*Solanum tuberosum*) as a new host for *Pentastiridius leporinus* (Hemiptera: Cixiidae) and *Candidatus* Arsenophonus phytopathogenicus. Insects 14:281. https://doi.org/10.3390/insects14030281.

Belgiu, M. and Drăgu, L. 2016. Random forest in remote sensing: A review of applications and future directions. ISPRS J Photogramm Remote Sen 114:24–31. https://doi.org/10.1016/j.isprsjprs.2016.01.011.

Benelli, A., Cevoli, C. and Fabbri, A. 2020. In-field hyperspectral imaging: An overview on the ground-based applications in agriculture. J Agric Eng 51:129–139. https://doi.org/10.4081/jae.2020.1030.

Bock, C. H., Barbedo, J. G. A., Del Ponte, E. M., Bohnenkamp, D. and Mahlein, A.-K. 2020. From visual estimates to fully automated sensor-based measurements of plant disease severity: status and challenges for improving accuracy. Phytopathol Res 2:9. https://doi.org/10.1186/s42483-020-00049-8.

Bohnenkamp, D., Behmann, J., Paulus, S., Steiner, U. and Mahlein, A.-K. 2021. A hyperspectral library of foliar diseases of wheat. Phytopathology 111:1583–1593. https://doi.org/10.1094/PHYTO-09-19-0335-R.

Bousquet, L., Lachérade, S., Jacquemoud, S. and Moya, I. 2005. Leaf BRDF measurements and model for specular and diffuse components differentiation. Remote. Sens. Environ. 98:201–211. https://doi.org/10.1016/j.rse.2005.07.005.

Breiman, L. 2001. Random Forests. Mach Learn 45:5–32. https://doi.org/10.1023/A:1010933404324.

Bressan, A. 2014. Emergence and evolution of Arsenophonus bacteria as insect-vectored plant pathogens. Infect Genet Evol 22:81–90. https://doi.org/10.1016/j.meegid.2014.01.004.

Bressan, A., Sémétey, O., Nusillard, B., Clair, D. and Boudon-Padieu, E. 2008. Insect vectors (Hemiptera: Cixiidae) and pathogens associated with the disease syndrome “basses richesses” of sugar beet in France. Plant Dis 92:113–119. https://doi.org/10.1094/PDIS-92-1-0113.

Bundesamt für Verbraucherschutz und Lebensmittelsicherheit 2025. BVL ermöglicht Bekämpfung von Glasflügelzikaden als Überträger bakterieller Krankheitserreger an Zuckerrüben. https://www.bvl.bund.de/SharedDocs/Fachmeldungen/04_pflanzenschutzmittel/2025/2025_04_23_Fa_Notfallzulassungen_Glasfluegelzikade_Kartoffel.html (accessed: 22. Dec. 2025).

Bundessortenamt 2025. Beschreibende Sortenliste Getreide Mais Öl- und Faserpflanzen Leguminosen Rüben Zwischenfrüchte. https://www.bundessortenamt.de/bsa/media/Files/BSL/bsl_getreide_2025.pdf (accessed: 22. Dec. 2025).

Calcagno, V., Mitoyen, C., Audiot, P., Ponsard, S., Gao, G. Z., Lu, Z. Z., Wang, Z. Y., He, K. L. and Bourguet, D. 2017. Parallel evolution of behaviour during independent host-shifts following maize introduction into Asia and Europe. Evol Appl 10:881–889. https://doi.org/10.1111/eva.12481.

Coblentz, W. W. 1932. The Copenhagen meeting of the second international congress on Light. Science (1979) 76:412–415. https://doi.org/10.1126/science.76.1975.412.

Cortes, C. and Vapnik, V. 1995. Support-vector networks. Mach Learn 20:273–297. https://doi.org/10.1007/BF00994018.

Ćurčić, Ž., Stepanović, J., Zübert, C., Taški-Ajduković, K., Kosovac, A., Rekanović, E., Kube, M. and Duduk, B. 2021. Rubbery Taproot Disease of sugar beet in Serbia associated with "*Candidatus* phytoplasma solani." Plant Dis 105:255–263. https://doi.org/10.1094/PDIS-07-20-1602-RE.

Detring, J. 2022. Host suitability of cash and catch crops for *Pentastiridius leporinus* (Hem., Cixiidae). Master Thesis, Georg-August-Universität-Göttingen. https://doi.org/http://dx.doi.org/10.53846/goediss-11449.

Dittmer, J., Lusseau, T., Foissac, X. and Faoro, F. 2021. Skipping the insect vector: Plant stolon transmission of the phytopathogen '*Ca.* Phlomobacter fragariae' from the *Arsenophonus* clade of insect endosymbionts. Insects 12:93. https://doi.org/10.3390/insects12020093.

Duduk, B., Stepanović, J., Fránová, J., Zwolińska, A., Rekanović, E., Stepanović, M., Vučković, N., Duduk, N. and Vico, I. 2024. Geographical variations, prevalence, and molecular dynamics of fastidious phloem-limited pathogens infecting sugar beet across Central Europe. PLoS One 19:e0306136. https://doi.org/10.1371/journal.pone.0306136.

EPPO. 2025. EPPO Global Database - '*Candidatus* Arsenophonus phytopathogenicus' (ARSEPH). EPPO.

Esser, F., Rosu, R. A., Cornelißen, A., Klingbeil, L., Kuhlmann, H. and Behnke, S. 2023. Field robot for high-throughput and high-resolution 3D plant phenotyping: Towards efficient and sustainable crop production. IEEE Robot Autom Mag 30:20–29. https://doi.org/10.1109/MRA.2023.3321402.

Esser, F., Tombrink, G., Cornelißen, A., Klingbeil, L. and Kuhlmann, H. 2024. System calibration of a field phenotyping robot with multiple high-precision profile laser scanners. In: 2024 IEEE International Conference on Robotics and Automation pp. 8471–8477. https://doi.org/10.1109/ICRA57147.2024.10610208.

Fisher, R. A. 1919. XV.-The correlation between relatives on the supposition of Mendelian inheritance. Trans R Soc Edinburgh 52:399–433. https://doi.org/10.1017/S0080456800012163.

Fox, E. W., Hill, R. A., Leibowitz, S. G., Olsen, A. R., Thornbrugh, D. J. and Weber, M. H. 2017. Assessing the accuracy and stability of variable selection methods for random forest modeling in ecology. Environ Monit Assess 189:316. https://doi.org/10.1007/s10661-017-6025-0.

Furbank, R. T. and Tester, M. 2011. Phenomics - technologies to relieve the phenotyping bottleneck. Trends Plant Sci 16:635–644. https://doi.org/10.1016/j.tplants.2011.09.005.

Gao, B. C., Montes, M. J., Davis, C. O. and Goetz, A. F. H. 2009. Atmospheric correction algorithms for hyperspectral remote sensing data of land and ocean. Remote Sens Environ 113:17-24. https://doi.org/10.1016/j.rse.2007.12.015.

Gatineau, F., Jacob, N., Vautrin, S., Larrue, J., Lherminier, J., Richard-Molard, M. and Boudon-Padieu, E. 2002. Association with the syndrome “Basses Richesses” of sugar beet of a phytoplasma and a bacterium-Like organism transmitted by a *Pentastiridius* sp. Phytopathology 92:384–392. https://doi.org/https://doi.org/10.1094/PHYTO.2002.92.4.384.

Gatineau, F., Larrue, J., Clair, D., Lorton, F., Richard-Molard, M. and Boudon-Padieu, E. 2001. A new natural planthopper vector of stolbur phytoplasma in the genus *Pentastiridius* (Hemiptera: Cixiidae). Eur J Plant Pathol 107:263–271. https://doi.org/https://doi.org/10.1023/A:1011209229335.

Geiger, D. R., Saunders, M. A. and Cataldo, D. A. 1969. Translocation and accumulation of translocate in the sugar beet petiole. Plant Physiol 44:1657–1665. https://doi.org/https://doi.org/10.1104/pp.44.12.1657.

Gill, T., Gill, S. K., Saini, D. K., Chopra, Y., de Koff, J. P. and Sandhu, K. S. 2022. A comprehensive review of high throughput phenotyping and machine learning for plant stress phenotyping. Phenomics 2:156–183. https://doi.org/10.1007/s43657-022-00048-z.

Gkologkinas, G. D., Ntouros, K., Protopapadakis, E. and Rallis, I. 2025. A comparative analysis of U-Net architectures with dimensionality reduction for agricultural crop classification using hyperspectral data. Algorithms 18:588. https://doi.org/10.3390/a18090588.

Grabenweger, G. 2004. Poor control of the horse chestnut leafminer, *Cameraria ohridella* (Lepidoptera: Gracillariidae), by native European parasitoids: A synchronisation problem. Eur J Entomol 101:189–192. https://doi.org/10.14411/eje.2004.023.

Griffin, M. K. and Burke, H. K. 2003. Compensation of hyperspectral data for atmospheric effects. Lincoln Lab J 14:29–54.

Habib, A., Xiong, W., He, F., Yang, H. L. and Crawford, M. 2017. Improving orthorectification of UAV-based push-broom scanner imagery using derived orthophotos from frame cameras. IEEE J Sel Top Appl Earth Obs Remote Sens 10:262–276. https://doi.org/10.1109/JSTARS.2016.2520929.

Haider, M. W., Sharma, A., Majumdar, A., Fayaz, F., Bromand, F., Rani, U., Singh, V. K., Saharan, M. S., Tiwari, R. K., Lal, M. K. and Kumar, R. 2024. Unveiling the phloem: a battleground for plant pathogens. Phytopathol Res 6:65. https://doi.org/10.1186/s42483-024-00286-1.

Harandi, N., Vandenberghe, B., Vankerschaver, J., Depuydt, S. and Van Messem, A. 2023. How to make sense of 3D representations for plant phenotyping: a compendium of processing and analysis techniques. Plant Methods 19:60. https://doi.org/10.1186/s13007-023-01031-z.

Haris, A., Józan, Z., Schmidt, P., Glemba, G., Tomozii, B., Csóka, G., Hirka, A., Šima, P. and Tóth, S. 2025. Climate change influences on central European insect fauna over the last 50 years: Mediterranean Influx and Non-Native Species. Ecologies 6:16. https://doi.org/10.3390/ecologies6010016.

He, K., Gkioxari, G., Dollar, P. and Girshick, R. 2017. Mask R-CNN. In 2017 IEEE International Conference on Computer Vision pp. 2980–2988. https://doi.org/10.1109/ICCV.2017.322.

He, K., Zhang, X., Ren, S. and Sun, J. 2016. Deep residual learning for image recognition. In: 2016 IEEE Conference on Computer Vision and Pattern Recognition pp. 770–778. https://doi.org/10.1109/CVPR.2016.90.

Hillnhütter, C., Mahlein, A.-K., Sikora, R. A. and Oerke, E. C. 2012. Use of imaging spectroscopy to discriminate symptoms caused by *Heterodera schachtii* and *Rhizoctonia solani* on sugar beet. Precis Agric 13:17–32. https://doi.org/10.1007/s11119-011-9237-2.

Hoffmann, C. M., Leijdekkers, M., Ekelöf, J. and Vancutsem, F. 2018. Patterns for improved storability of sugar beet – importance of marc content and damage susceptibility of varieties in different environments. Eur J Agron 101:30–37. https://doi.org/10.1016/j.eja.2018.08.004.

Hotelling, H. 1933. Analysis of a complex of statistical variables into principal components. J Educ Psychol 24:417–441. https://doi.org/10.1037/h0071325.

Hu, T., Zhang, X., Khanal, S., Wilson, R., Leng, G., Toman, E. M., Wang, X., Li, Y. and Zhao, K. 2024. Climate change impacts on crop yields: A review of empirical findings, statistical crop models, and machine learning methods. Environ Model and Softw 179: 106119. https://doi.org/10.1016/j.envsoft.2024.106119.

Ihalainen, O., Sandmann, T., Rascher, U. and Mõttus, M. 2024. Illumination correction for close-range hyperspectral images using spectral invariants and random forest regression. Remote Sens Environ 315:114467. https://doi.org/10.1016/j.rse.2024.114467.

Jablonski, J., Durell, C., Slonecker, T., Wong, K., Simon, B., Eichelberger, A. and Osterberg, J. 2016. Best practices in passive remote sensing VNIR hyperspectral system hardware calibrations. In Hyperspectral Imaging Sensors: Innovative Applications and Sensor Standards 2016 p. 986004. https://doi.org/10.1117/12.2224022.

Johannsen, W. 1911. The genotype conception of heredity. Int J Epidemiol 43:989-1000. https://doi.org/10.1093/ije/dyu063.

Johannsen, W. L. 1903. Erblichkeit in Populationen und in reinen Linien. Gustav Fischer Verlag, Jena.

Kais, B., Köhler, J., Werner, P. and Mannheim, H. 2023. Does the causative agent of Syndrome Basses Richesses (SBR), *Candidatus* Arsenophonus phytopathogenicus, alter sugar beet phloem composition or plant-emitted volatiles? In: International Organisation for Biological and Integrated Control West Palaearctic Regional Section Bulletins pp. 128–133.

Kazmi, W., Foix, S., Alenyà, G. and Andersen, H. J. 2014. Indoor and outdoor depth imaging of leaves with time-of-flight and stereo vision sensors: Analysis and comparison. ISPRS J Photogramm Remote Sens 88:128–146. https://doi.org/10.1016/j.isprsjprs.2013.11.012.

Kirchhoff, G. and Bunsen, R. 1860. Chemische Analyse durch Spectralbeobachtungen. In: Annalen der Physik und Chemie, Dörflinger, Heidelberg.

Kirillov, A., Mintun, E., Ravi, N., Mao, H., Rolland, C., Gustafson, L., Xiao, T., Whitehead, S., Berg, A. C., Lo, W.-Y., Dollár, P. and Girshick, R. 2023. Segment Anything.

In: 2023 IEEE/CVF International Conference on Computer Vision pp. 3992–4003. https://doi.org/10.1109/ICCV51070.2023.00371.

Kleuker, G. and Hoffmann, C. M. 2022. Causes of different tissue strength, changes during storage and effect on the storability of sugar beet genotypes. Postharvest Biol Technol 183:111744. https://doi.org/10.1016/j.postharvbio.2021.111744.

Kleuker, G. and Hoffmann, C. M. 2019. Method development for the determination of textural properties of sugar beet roots. Sugar Industry 144:392–400. https://doi.org/10.36961/si23306.

Kleuker, G. and Hoffmann, C. M. 2021. Tissue strength of sugar beet root genotypic variation and environmental impact. Crop Sci 61:2478–2488. https://doi.org/10.1002/csc2.20523.

Koh, E. J., Zhou, L., Williams, D. S., Park, J., Ding, N., Duan, Y. P. and Kang, B. H. 2012. Callose deposition in the phloem plasmodesmata and inhibition of phloem transport in citrus leaves infected with “*Candidatus* Liberibacter asiaticus.” Protoplasma 249:687–697. https://doi.org/10.1007/s00709-011-0312-3.

Kong, L., Ji, M., Holtom, G. R., Fu, D., Freudiger, C. W. and Xie, X. S. 2013. Multicolor stimulated Raman scattering microscopy with a rapidly tunable optical parametric oscillator. Opt Lett 38:145-147. https://doi.org/10.1364/OL.38.000145.

Kosovac, A., Ćurčić, Ž., Stepanović, J., Rekanović, E. and Duduk, B. 2023. Epidemiological role of novel and already known ‘*Ca.* P. solani’ cixiid vectors in Rubbery Taproot Disease of sugar beet in Serbia. Sci Rep 13. https://doi.org/10.1038/s41598-023-28562-8.

Kreitzer, C., Stepanović, J., Stanojević, N., Rohringer, A., Seiter, M., Rekanović, E. and Duduk, B. 2025. Dominant cixiid vector and transmission of ‘*Candidatus* Arsenophonus phytopathogenicus’ and ‘*Candidatus* Phytoplasma solani’-related strain 16SrXII-P in sugar beet in Austria. Sci Rep 15:22526. https://doi.org/10.1038/s41598-025-07035-0.

Kursa, M. B. and Rudnicki, W. R. 2010. Feature selection with the Boruta package. J Stat Softw 36:1-13. https://doi.org/10.18637/jss.v036.i11.

Lang, C., Dettweiler, A., Benaouda, S., Kreimer, D., Löffler, D., Glaser, E., Adam, H., Bojanowicz, S. L., Schall, E., Stohl, J., Göbbels, H., Lenz, M., Witczak, N., Ritz, J. and Pfitzner, H. 2025. *Pentastiridius leporinus* as a plant disease vector: The practical state of knowledge and derived research objectives. Sugar Industry 150:105–120. https://doi.org/10.36961/si33023.

Li, S., Qiu, J., Yang, X., Liu, H., Wan, D. and Zhu, Y. 2014. A novel approach to hyperspectral band selection based on spectral shape similarity analysis and fast branch and bound search. Eng Appl Artif Intell 27:241–250. https://doi.org/10.1016/j.engappai.2013.07.010.

Liakos, K., Busato, P., Moshou, D., Pearson, S. and Bochtis, D. 2018. Machine learning in agriculture: A review. Sensors 18:2674. https://doi.org/10.3390/s18082674.

Ma, Q.-H. 2024. Lignin biosynthesis and its diversified roles in disease resistance. Genes 15:295. https://doi.org/10.3390/genes15030295.

Mahillon, M., Groux, R., Bussereau, F., Brodard, J., Debonneville, C., Demal, S., Kellenberger, I., Peter, M., Steinger, T. and Schumpp, O. 2022. Virus yellows and syndrome “Basses Richesses” in western Switzerland: A dramatic 2020 season calls for urgent control measures. Pathogens 11:885. https://doi.org/10.3390/pathogens11080885.

Mahlein, A.-K., Hammersley, S., Oerke, E. C., Dehne, H. W., Goldbach, H. and Grieve, B. 2015. Supplemental blue LED lighting array to improve the signal quality in hyperspectral imaging of plants. Sensors 15:12834–12840. https://doi.org/10.3390/s150612834.

Mahlein, A.-K., Kuska, M. T., Behmann, J., Polder, G. and Walter, A. 2018. Hyperspectral sensors and imaging technologies in phytopathology: State of the art. Annu Rev Phytopathol 56:535–558. https://doi.org/10.1146/annurev-phyto-080417-050100.

Mahlein, A.-K., Kuska, M. T., Thomas, S., Wahabzada, M., Behmann, J., Rascher, U. and Kersting, K. 2019. Quantitative and qualitative phenotyping of disease resistance of crops by hyperspectral sensors: seamless interlocking of phytopathology, sensors, and machine learning is needed! Curr Opin Plant Biol 50:156–162. https://doi.org/10.1016/j.pbi.2019.06.007.

Mahlein, A.-K., Steiner, U., Hillnhütter, C., Dehne, H.-W. and Oerke, E.-C. 2012. Hyperspectral imaging for small-scale analysis of symptoms caused by different sugar beet diseases. Plant Methods 8:3. https://doi.org/10.1186/1746-4811-8-3.

Malavasi, U. C., Davis, A. S. and de Matos Malavasi, M. 2016. Lignin in woody plants under water stress: A review. Floresta e Ambiente 23:589–597. https://doi.org/10.1590/2179-8087.143715.

Marshall, K. E., Gotthard, K. and Williams, C. M. 2020. Evolutionary impacts of winter climate change on insects. Curr Opin Insect Sci 41:54–62. https://doi.org/10.1016/j.cois.2020.06.003.

Mayerhöfer, T. G., Pahlow, S. and Popp, J. 2020. The Bouguer-Beer-Lambert law: Shining light on the obscure. ChemPhysChem 21:2029–2046. https://doi.org/10.1002/cphc.202000464.

Mazzetto, F., Calcante, A. and Mena, A. 2009. Comparing commercial optical sensors for crop monitoring tasks in precision viticulture. J Agric Eng 40:11. https://doi.org/10.4081/jae.2009.1.11.

McGrann, G. R. D., Grimmer, M. K., Mutasa-Göttgens, E. S. and Stevens, M. 2009. Progress towards the understanding and control of sugar beet rhizomania disease. Mol Plant Pathol 10:129–141. https://doi.org/10.1111/j.1364-3703.2008.00514.x.

Mishra, P., Asaari, M. S. M., Herrero-Langreo, A., Lohumi, S., Diezma, B. and Scheunders, P. 2017. Close range hyperspectral imaging of plants: A review. Biosyst Eng 164:49–67. https://doi.org/10.1016/j.biosystemseng.2017.09.009.

Morkunas, I. and Ratajczak, L. 2014. The role of sugar signaling in plant defense responses against fungal pathogens. Acta Physiol Plant 36:1607–1619. https://doi.org/10.1007/s11738-014-1559-z.

Mota, I. F., Antunes, F., Fangueiro, J. F., Costa, C. A. E., Rodrigues, A. E., Pintado, M. E. and Costa, P. S. 2023. Sugarcane light-colored lignin: A renewable resource for sustainable beauty. Int J Mol Sci 24:15941. https://doi.org/10.3390/ijms242115941.

Mouroulis, P. and Green, R. O. 2018. Review of high fidelity imaging spectrometer design for remote sensing. Opt Eng 57:040901. https://doi.org/10.1117/1.oe.57.4.040901.

Nause, N., Meier, T. and Hoffmann, C. M. 2020. Tissue composition and arrangement in sugar beet genotypes of different tissue strength with regard to damage and pathogen infestation. Sugar Industry 2:114–123. https://doi.org/https://doi.org/10.36961/si24063.

Nethala, P., Um, D., Vemula, N., Montero, O. F., Lee, K. and Bhandari, M. 2024. Techniques for canopy to organ level plant feature extraction via remote and proximal sensing: A survey and experiments. Remote Sens 16:4370. https://doi.org/10.3390/rs16234370.

Nickel, H., Achtziger, R., Biedermann, R., Bückel, C., Deutschmann, U., Niedringhaus, R., Remane, R., Walter, S. and Witsack, W. 2016. Rote Liste und Gesamtartenliste der Zikaden (Hemiptera: Auchenorrhyncha) deutschlands. Naturschutz und Biologische Vielfalt 70:247-298.

Nohara, Y., Matsumoto, K., Soejima, H. and Nakashima, N. 2022. Explanation of machine learning models using shapley additive explanation and application for real data in hospital. Comput Methods Programs Biomed 214:106584. https://doi.org/10.1016/j.cmpb.2021.106584.

Nováková, E., Hypša, V. and Moran, N. A. 2009. *Arsenophonus*, an emerging clade of intracellular symbionts with a broad host distribution. BMC Microbiol 9:143. https://doi.org/10.1186/1471-2180-9-143.

Okole, N., Yamati, F. R., Hossain, R., Varrelmann, M., Mahlein, A.-K. and Heim, R. H. 2023. Hyperspectral signatures and betalain indicator for beet mosaic virus infection in sugar beet. In 2023 IEEE International Workshop on Metrology for Agriculture and Forestry pp. 506–511. https://doi.org/10.1109/MetroAgriFor58484.2023.10424290.

Orlova-Bienkowskaja, M. J., Drogvalenko, A. N., Zabaluev, I. A., Sazhnev, A. S., Peregudova, E. Y., Mazurov, S. G., Komarov, E. V., Struchaev, V. V., Martynov, V. V., Nikulina, T. V. and Bieńkowski, A. O. 2019. Current range of *Agrilus planipennis* Fairmaire, an alien pest of ash trees, in European Russia and Ukraine. Ann For Sci 77:29. https://doi.org/10.1007/s13595-020-0930-z.

Paulus, S. 2019. Measuring crops in 3D: Using geometry for plant phenotyping. Plant Methods 15:103. https://doi.org/10.1186/s13007-019-0490-0.

Paulus, S., Behmann, J., Mahlein, A.-K., Plümer, L. and Kuhlmann, H. 2014a. Low-cost 3D systems: Suitable tools for plant phenotyping. Sensors 14:3001–3018. https://doi.org/10.3390/s140203001.

Paulus, S. and Mahlein, A.-K. 2020. Technical workflows for hyperspectral plant image assessment and processing on the greenhouse and laboratory scale. Gigascience 9:giaa090. https://doi.org/10.1093/gigascience/giaa090.

Paulus, S., Schumann, H., Kuhlmann, H. and Léon, J. 2014b. High-precision laser scanning system for capturing 3D plant architecture and analysing growth of cereal plants. Biosyst Eng 121:1–11. https://doi.org/10.1016/j.biosystemseng.2014.01.010.

Peng, D., Zhu, G. and Xie, Z. 2025. A high-precision segmentation method based on UNet for disc cutter holder of shield machine. Sci Rep 15:24085. https://doi.org/10.1038/s41598-025-10559-0.

Percival, G., Keary, I. and Noviss, K. 2008. The potential of a chlorophyll content SPAD meter to quantify nutrient stress in foliar tissue of Sycamore (*Acer pseudoplatanus*), English Oak (*Quercus robur*), and European Beech (*Fagus sylvatica*). Arboric Urban For 34:89–100. https://doi.org/10.48044/jauf.2008.012.

Pfitzer, R., Rostás, M., Häußermann, P., Häuser, T., Rinklef, A., Detring, J., Schrameyer, K., Voegele, R. T., Maier, J. and Varrelmann, M. 2024. Effects of succession crops and soil tillage on suppressing the syndrome ‘Basses Richesses’ vector *Pentastiridius leporinus* in sugar beet. Pest Manag Sci 80:3379–3388. https://doi.org/10.1002/ps.8041.

Pfitzer, R., Varrelmann, M., Schrameyer, K. and Rostás, M. 2022. Life history traits and a method for continuous mass rearing of the planthopper *Pentastiridius leporinus*, a vector of the causal agent of syndrome ‘Basses Richesses’ in sugar beet. Pest Manag Sci 78:4700–4708. https://doi.org/10.1002/ps.7090.

Piršelová, B. and Matušíková, I. 2013. Callose: The plant cell wall polysaccharide with multiple biological functions. Acta Physiol Plant 35:635–644. https://doi.org/10.1007/s11738-012-1103-y.

Rehman, T. U., Ma, D., Wang, L., Zhang, L. and Jin, J. 2020. Predictive spectral analysis using an end-to-end deep model from hyperspectral images for high-throughput plant phenotyping. Comput Electron Agric 177:105713. https://doi.org/10.1016/j.compag.2020.105713.

Ronneberger, O., Fischer, P. and Brox, T. 2015. U-Net: Convolutional networks for biomedical image segmentation. In: 2015 Medical Image Computing and Computer-

Assisted Intervention pp. 234-241. https://doi.org/https://doi.org/10.1007/978-3-319-24574-4_28.

Salar, P., Sémétey, O., Danet, J. L., Boudon-Padieu, E. and Foissac, X. 2010. "*Candidatus* Phlomobacter fragariae" and the proteobacterium associated with the low sugar content syndrome of sugar beet are related to bacteria of the *Arsenophonus* clade detected in Hemipteran insects. Eur J Plant Pathol 126:123–127. https://doi.org/10.1007/s10658-009-9520-5.

Savitzky, A. and Golay, M. J. E. 1964. Smoothing and differentiation of data by simplified least squares procedures. Anal Chem 36:1627–1639. https://doi.org/https://doi.org/10.1021/ac60214a047.

Schnepel, K. and Hoffmann, C. M. 2016. Genotypic differences in storage losses of sugar beet - causes and indirect criteria for selection. Plant Breed 135:130–137. https://doi.org/10.1111/pbr.12338.

Sémétey, O., Bressan, A., Richard-Molard, M. and Boudon-Padieu, E. 2007a. Monitoring of proteobacteria and phytoplasma in sugar beets naturally or experimentally affected by the disease syndrome "Basses Richesses." Eur J Plant Pathol 117:187–196. https://doi.org/10.1007/s10658-006-9087-3.

Sémétey, O., Gatineau, F., Bressan, A. and Boudon-Padieu, E. 2007b. Characterization of a γ-3 proteobacteria responsible for the syndrome "Basses Richesses" of sugar beet transmitted by *Pentastiridius* sp. (Hemiptera, Cixiidae). Phytopathology 97:72–78. https://doi.org/10.1094/PHYTO-97-0072.

Sippel, S., Barnes, C., Cadiou, C., Fischer, E., Kew, S., Kretschmer, M., Philip, S., Shepherd, T. G., Singh, J., Vautard, R. and Yiou, P. 2024. Could an extremely cold central European winter such as 1963 happen again despite climate change? WCD 5:943–957. https://doi.org/10.5194/wcd-5-943-2024.

Skendžić, S., Zovko, M., Pajač Živković, I., Lešić, V. and Lemić, D. 2021. Effect of climate change on introduced and native agricultural invasive insect pests in Europe. Insects 12:985. https://doi.org/10.3390/insects12110985.

Sliney, D. H. 2016. What is light? The visible spectrum and beyond. Eye 30:222–229. https://doi.org/10.1038/eye.2015.252.

Smith, A. H., Gill, W. M., Pinkard, E. A. and Mohammed, C. L. 2007. Anatomical and histochemical defence responses induced in juvenile leaves of *Eucalyptus globulus* and *Eucalyptus nitens* by *Mycosphaerella* infection. For Pathol 37:361–373. https://doi.org/10.1111/j.1439-0329.2007.00502.x.

Sousa, J. J., Toscano, P., Matese, A., Di Gennaro, S. F., Berton, A., Gatti, M., Poni, S., Pádua, L., Hruška, J., Morais, R. and Peres, E. 2022. UAV-based hyperspectral monitoring using push-broom and snapshot sensors: A multisite assessment for precision viticulture applications. Sensors 22:6574. https://doi.org/10.3390/s22176574.

Srisakrapikoop, U., Pirie, T. J. and Fellowes, M. D. E. 2020. Meta-analysis suggests differing indirect effects of viral, bacterial and fungal plant pathogens on the natural enemies of insect herbivores. Insects 11:765. https://doi.org/10.3390/insects11110765.

Stoeckli, S., Hirschi, M., Spirig, C., Calanca, P., Rotach, M. W. and Samietz, J. 2012. Impact of climate change on voltinism and prospective diapause induction of a global pest insect - *Cydia pomonella* (L.). PLoS One 7:e35723. https://doi.org/10.1371/journal.pone.0035723.

Thomas, S., Behmann, J., Steier, A., Kraska, T., Muller, O., Rascher, U. and Mahlein, A.-K. 2018. Quantitative assessment of disease severity and rating of barley cultivars based on hyperspectral imaging in a non-invasive, automated phenotyping platform. Plant Methods 14:45. https://doi.org/10.1186/s13007-018-0313-8.

Tiwari, R. K., Goswami, S. K., Gujjar, R. S., Kumar, R., Kumar, R., Lal, M. K. and Kumari, M. 2025. Mechanistic insights on lignin-mediated plant defense against pathogen infection. Plant Physiol Biochem 228:110224. https://doi.org/10.1016/j.plaphy.2025.110224.

Triki, A., Bouaziz, B., Gaikwad, J. and Mahdi, W. 2021. Deep leaf: Mask R-CNN based leaf detection and segmentation from digitized herbarium specimen images. Pattern Recognit Lett 150:76–83. https://doi.org/10.1016/j.patrec.2021.07.003.

Tsialtas, J. T., Baxevanos, D. and Maslaris, N. 2014. Chlorophyll meter readings, leaf area index and their stability as assessments of yield and quality in sugar beet cultivars grown in two contrasting environments. Crop Sci 54:265–273. https://doi.org/10.2135/cropsci2013.03.0186.

Tsialtas, J. T. and Maslaris, N. 2007. Leaf shape and its relationship with Leaf Area Index in a sugar beet (*Beta vulgaris* L.) cultivar. Photosynthetica 45:527–532. https://doi.org/10.1007/s11099-007-0090-5.

Twardosz, R., Walanus, A. and Guzik, I. 2021. Warming in Europe: Recent trends in annual and seasonal temperatures. Pure Appl Geophys 178:4021–4032. https://doi.org/10.1007/s00024-021-02860-6.

Ulku, I. and Akagündüz, E. 2022. A survey on deep learning-based architectures for semantic segmentation on 2D images. Appl Artif Intell 36:2032924. https://doi.org/10.1080/08839514.2022.2032924.

Vance, C. P., Kirk, T. K. and Sherwood, R. T. 1980. Lignification as a mechanism of disease resistance. Annu Rev Phytopathol 18:259–288. https://doi.org/10.1146/annurev.py.18.090180.001355.

Verhoef, W. and Bach, H. 2003. Simulation of hyperspectral and directional radiance images using coupled biophysical and atmospheric radiative transfer models. Remote Sens Environ 87:23–41. https://doi.org/10.1016/S0034-4257(03)00143-3.

Vermote, E. and Roger, J. C. 1996. Radiative transfer modelling for calibration and atmospheric correction. In: D'Souza, G., Belward, A.S., Malingreau, JP. (eds) Advances in the Use of NOAA AVHRR Data for Land Applications. Euro Courses, vol 5. Springer, Dordrecht. https://doi.org/10.1007/978-94-009-0203-9_3.

Vogel, E., Donat, M. G., Alexander, L. V., Meinshausen, M., Ray, D. K., Karoly, D., Meinshausen, N. and Frieler, K. 2019. The effects of climate extremes on global agricultural yields. Environ Res Lett 14:054010. https://doi.org/10.1088/1748-9326/ab154b.

Vollset, S. E., Goren, E., Yuan, C. W., Cao, J., Smith, A. E., Hsiao, T., Bisignano, C., Azhar, G. S., Castro, E., Chalek, J., Dolgert, A. J., Frank, T., Fukutaki, K., Hay, S. I., Lozano, R., Mokdad, A. H., Nandakumar, V., Pierce, M., Pletcher, M., Robalik, T., Steuben, K. M., Wunrow, H. Y., Zlavog, B. S. and Murray, C. J. L. 2020. Fertility, mortality, migration and population scenarios for 195 countries and territories from 2017 to 2100: A forecasting analysis for the Global Burden of Disease Study. Lancet 396:1285–1306. https://doi.org/10.1016/S0140-6736(20)30677-2.

Welvaert, M. and Rosseel, Y. 2013. On the definition of signal-to-noise ratio and contrast-to-noise ratio for fMRI data. PLoS One 8:e77089. https://doi.org/10.1371/journal.pone.0077089.

Wielkopolan, B., Jakubowska, M. and Obrępalska-Stęplowska, A. 2021. Beetles as plant pathogen vectors. Front Plant Sci 12:748093. https://doi.org/10.3389/fpls.2021.748093.

Winkelbach, S., Molkenstruck, S., Wahl, F.M. (2006). Low-cost laser range scanner and fast surface registration approach. In: Franke, K., Müller, KR., Nickolay, B., Schäfer, R. (eds) Pattern Recognition. DAGM 2006. Lecture Notes in Computer Science, vol 4174. Springer, Berlin, Heidelberg. https://doi.org/10.1007/11861898_72.

Wirtschaftliche Vereinigung Zucker. 2025. Gefahr für die heimische Lebensmittelversorgung: Zikade gefährdet Zuckerrübenanbau. https://www.zuckerverbaende.de/wp-content/uploads/2025/03/20250401_WVZ_PM_SBR_Stolbur.pdf (accessed: 30. Nov. 2025).

Witczak, N., Benaouda, S., Wahl, F., Göbbels, H., Lang, C., Jarausch, B. and Maixner, M. 2025. Carrot (*Daucus carota* L.) as host for *Pentastiridius leporinus* and phloem-restricted pathogens in Germany. Biology 14:1152. https://doi.org/10.3390/biology14091152.

Yamati, F. R. I., Günder, M., Barreto, A., Bömer, J., Laufer, D., Bauckhage, C. and Mahlein, A.-K. 2024. Automatic scoring of Rhizoctonia Crown and Root Rot affected sugar beet fields from orthorectified UAV images using machine learning. Plant Dis 108:711–724. https://doi.org/10.1094/PDIS-04-23-0779-RE.

Yang, C., Liang, Y., Qiu, D., Zeng, H., Yuan, J. and Yang, X. 2018. Lignin metabolism involves *Botrytis cinerea* BcGs1- induced defense response in tomato. BMC Plant Biol 18:103. https://doi.org/10.1186/s12870-018-1319-0.

Yang, F., Wang, H., Mi, H., Lin, C. and Cai, W. 2009. Using random forest for reliable classification and cost-sensitive learning for medical diagnosis. BMC Bioinform 10:S22. https://doi.org/10.1186/1471-2105-10-S1-S22.

Zheng, J., Chen, L., Qiu, X., Liu, Y. and Qin, Y. 2023. Structure investigation of light-colored lignin extracted by Lewis acid-based deep eutectic solvent from softwood. Bioresour Technol 385:129458. https://doi.org/10.1016/j.biortech.2023.129458.

Zübert, C. and Kube, M. 2021. Application of TaqMan real-time PCR for detecting '*Candidatus* Arsenophonus phytopathogenicus' infection in sugar beet. Pathogens 10:1466. https://doi.org/10.3390/pathogens10111466.

Acknowledgments

I would like to express my gratitude to Prof. Dr. Anne-Katrin Mahlein, my doctoral supervisor, for her continuous guidance, invaluable insights and unwavering support throughout this research. Her expertise and encouragement have been instrumental in shaping both the direction and quality of this work.

I would like to thank Prof. Dr. Gabriel Schaaf for agreeing to serve as the second examiner of this dissertation. I appreciate his willingness to review and evaluate my work as part of the examination process.

I am thankful for my PhD colleagues Abel, Jonas and Facundo who became much more than co-workers throughout this journey. Your friendship, kindness and unwavering support helped me navigate both the challenges and the joys of this research. Thank you for the conversations that clarified ideas, the encouragement that lifted my spirits and the shared laughter that made even the most difficult days lighter. Working alongside you has been one of the most meaningful parts of this process and I am thankful not only for your help, but for the friendship that grew from it.

I would like to thank Stefan, Jonathan and Dirk from the Remote Sensing group at the Institute of Sugar Beet Research for supporting me in any way they could.

I would like to extend my sincere thanks to Rebekka and Christa who assisted with proofreading this dissertation. Your careful reading, thoughtful comments and attention to detail greatly improved the clarity, precision and overall quality of the final text.

My deepest gratitude goes to my beloved wife Eva, whose love, patience and unwavering belief in me carried me through every stage of this dissertation. Thank you for standing beside me through long nights, stressful deadlines and moments of doubt. Your strength and kindness have been my anchor and your encouragement has given me the courage to keep going when everything felt overwhelming. I am endlessly grateful for your sacrifices, your understanding and the countless ways you made it possible for me to pursue this work.

To my precious daughter Helena, who brought more joy into my life than words can capture. Thank you for reminding me, every day, of what truly matters. Your laughter, your curiosity and your very presence filled even the hardest days with light. You have been my inspiration, my motivation and my greatest happiness.